THE CREATION AND FREQUENCY TRANSLATION OF SINGLE-PHOTON STATES OF LIGHT IN OPTICAL FIBER

by

HAYDEN JAMES MCGUINNESS

A DISSERTATION

Presented to the Department of Physics
and the Graduate School of the University of Oregon
in partial fulfillment of the requirements
for the degree of
Doctor of Philosophy

March 2011

DISSERTATION APPROVAL PAGE

Student: Hayden James McGuinness

Title: The Creation and Frequency Translation of Single-Photon States of Light in Optical Fiber

This dissertation has been accepted and approved in partial fulfillment of the requirements for the Doctor of Philosophy degree in the Department of Physics by:

Dr. Daniel Steck	Chair
Dr. Michael Raymer	Advisor
Dr. Steven van Enk	Inside Member
Dr. Raghuveer Parthasarathy	Inside Member
Dr. Andrew Marcus	Outside Member

and

Richard Linton	Vice President for Research and Graduate Studies/ Dean of the Graduate School

Original approval signatures are on file with the University of Oregon Graduate School.

Degree awarded March 2011

DISSERTATION ABSTRACT

Hayden James McGuinness

Doctor of Philosophy

Department of Physics

March 2011

Title: The Creation and Frequency Translation of Single-Photon States of Light in Optical Fiber

Approved: _____
Dr. Michael Raymer

We explore the frequency translation of single-photon states of light and the creation of photon pairs by four-wave mixing in optical fiber. Frequency translation refers to changing the central frequency of a field, while photon pair creation refers to the creation of two individual photons at the same time. We demonstrate these effects in third-order nonlinear optical fiber. While both phenomena have previously been shown by three-wave mixing in second-order nonlinear media, there are compelling reasons to develop these tasks in third-order media. Most importantly, frequency translation in third-order material allows for the practical implementation of both small and large frequency shifts, while second-order material only practically allows for large shifts. Photon creation in third-order media often permits more flexible phase-matching conditions, allowing for the creation of a wider variety of quantum states than is often possible in second-order media.

In our theoretical study of photon pair creation, we focus on the spectral correlations of the photon pairs. We pay particular attention to the creation of quantum states of high purity, where the photons are not spectrally correlated with

one another. High purity photons are a requisite resource for several different quantum information processing applications, such as linear-optical quantum computing. We find that states with high purity can be realized with a minimal amount of spectral filtering.

Experimentally, we study photon frequency translation in photonic crystal fiber. The central wavelength of the input photons was translated from 683 nm to 659 nm. We perform second-order intensity correlation measurements on both channels to demonstrate their quantum nature. This resulted in values of 0.21 ± 0.02 and 0.19 ± 0.05 for the 683-nm and 659-nm channels, respectively, demonstrating that those fields were dominated by their single-photon component. The efficiency at which the process occurred was 29 percent. Theoretically, we develop a Green function formalism to describe the translation process and develop a computational model to calculate the solution to the governing equations. Also, in a related experiment, we demonstrate classical frequency translation from 851 nm to 641 nm, a record translation in both wavelength and frequency, at an efficiency of 0.2 percent in a birefringent fiber.

CURRICULUM VITAE

NAME OF AUTHOR: Hayden James McGuinness

GRADUATE AND UNDERGRADUATE SCHOOLS ATTENDED:

University of Oregon, Eugene, Oregon
Rensselaer Polytechnic Institute, Troy, New York
Reed College, Portland, Oregon

DEGREES AWARDED:

Doctor of Philosophy in Physics, 2011, University of Oregon
Master of Science in Nuclear Engineering, 2005, Rensselaer Polytechnic Institute
Bachelor of Arts in Physics, 2002, Reed College

AREAS OF SPECIAL INTEREST:

Quantum Optics, Quantum Information Processing

PROFESSIONAL EXPERIENCE:

Graduate Research Assistant, University of Oregon, 2006 – 2011

Graduate Teaching Fellow, University of Oregon, 2005 – 2006

GRANTS, AWARDS AND HONORS:

Emil Wolf Outstanding Student Paper Competition: Winner, Frontiers in Optics, Rochester NY, 2010

Elected to Alpha Nu Sigma, Rensselaer Polytechnic Institute, Troy, New York, 2005

Elected to Phi Beta Kappa, Reed College, Portland, Oregon, 2002

Commended for Excellence in Academics, Reed College, Portland, Oregon, 1999, 2000, 2001, 2002

Marianne Ott Scholarship, Reed College, Portland, Oregon, 2000, 2001

Howard Vollum Scholarship, Reed College, Portland, Oregon, 1999

PUBLICATIONS:

H.J. McGuinness, M.G. Raymer, C.J. McKinstrie, and S. Radic, "Wavelength Translation across 210 nm in the Visible Using Vector Bragg Scattering in a Birefringent Photonic Crystal Fiber" Photon. Tech. Lett., **23**, 109-111 (2011).

H.J. McGuinness, M.G. Raymer, C.J. McKinstrie, and S. Radic, "Quantum frequency translation of single-photon states in photonic crystal fiber" Phys. Rev. Lett., **105**, 093604 (2010).

H.J. McGuinness, M.G. Raymer, C.J. McKinstrie, and S. Radic, "Translation of Single-Photon States by Four-Wave Mixing in Photonic Crystal Fiber," presented at the 2010 Quantum Electronics and Laser Science Conference (QELS), San Jose, CA, 16-21 May 2010. Published as Technical Digest; Quantum Electronics and Laser Science Conference (QELS), QFA5 (2010) (Optical Society of America, Washington, DC, 2010).

M.G. Raymer, S.J. van Enk, C.J. McKinstrie, and H.J. McGuinness, "Interference of two photons of different color" Opt. Comm., **283**, 747-752 (2010).

K. Garay-Palmett, H.J. McGuinness, O. Cohen, J.S. Lundeen, R. Rangel-Rojo, A.B. U'ren, M.G. Raymer, C.J. McKinstrie, S. Radic, and I.A. Walmsley, ""Photon pair-state preparation with tailored spectral properties by spontaneous four-wave mixing in photonic-crystal fiber" Opt. Express, **15**, 14870-14886 (2007).

A. Korotkov, M. Bowman, H. McGuinness, and D. Davidovic, "Influence of H2O molecules on sub-nanometer scale gaps between Au leads" Nanotechnology, **14**, 42-45, (2003).

ACKNOWLEDGEMENTS

I am indebted to my advisor, Professor Michael Raymer, in a number of ways. In my time at the University of Oregon he has guided me through the ins and outs of research, school, and the sometimes complex and confusing field of quantum optics. He was patient with me and my seemingly innumerable questions and pushed me to produce the highest quality work I was capable of producing. Simply put, he has been my principle teacher, mentor and collaborator throughout my graduate career, and I am grateful to have been his student. I owe thanks to Professor Daniel Steck for chairing my dissertation committee and for fielding more than his fair share of my quantum optics questions both in and out of the classroom. I also thank my dissertation committee members, Professor Steven van Enk, Professor Raghuveer Parthasarathy, and Professor Andrew Marcus for their willingness to helpfully critique and edit my dissertation. From outside the University of Oregon I would like to thank Dr. Colin McKinstrie of Bell Labs for our numerous fruitful collaborative efforts and his willingness to explain mathematical concepts to me that I once found difficult.

Graduate school would have been much less fun and interesting without the camaraderie and support of fellow graduate students. There are too many fellow students to thank, but in particular I would like to thank the following. My current labmates, Dash, Roger, Erin, and Kyle and been helpful and supportive, and in particular I have enjoyed multiple conversations, physics related and otherwise, with Dash and Roger. Former Raymer group members Cody Leary, Chunbai Wu, Justin Hannigan, and Brian Smith have helped me grow as a physicist by patiently answering all of my questions and helping me complete my experiments. Outside of the lab, I would like to thank Tim Sweeney for his penchant for discussing all sorts of interesting

physics phenomena and for being an all-around great friend, Vipul Lugade for his wonderful companionship, uplifting attitude, and unstoppable stream of good project ideas, and Mark Leymon for his friendship and service to the graduate student population through the GTFF. Special thanks must be given to Maggie Evans, who has shared my life in full for the last three years, through good and difficult times has always supported me, and has put up with my need to constantly work these last few months.

Finally, I am deeply indebted to my parents for their guidance and their faith in me and my abilities. Without their unwavering support I would not be the person or the scientist I am today.

TABLE OF CONTENTS

Chapter Page

LIST OF FIGURES

Figure Page

Chapter Page

CHAPTER I

INTRODUCTION

The advent of quantum mechanics at the beginning of the previous century revolutionized our understanding of the physical world. Nearly a century later, the full implications of the theory are still being explored experimentally, theoretically, and philosophically. The new theory quickly ushered in novel technologies and applications; quantum theory was used to explain how the microscopic world worked, which was needed in order to fully to understand the transistor, solar cell, the phenomenon of superconductivity, and the laser, to name a few. These technologies rely on what already exists in nature. In the past couple of decades, quantum physics has played an ever-increasing role in applied fields such as metrology, lithography, and, with continually decreasing circuit sizes, information technology. This has ushered in the "second quantum revolution" with several emergent research areas including nanotechnology, quantum metrology, and quantum information [1]. With these new types of quantum technologies, systems are engineered to exhibit quantum properties such as quantum coherence or entanglement, instead of just using what is naturally available. Often these new quantum technologies rely on processing the informational content of the quantum object and are therefore known as quantum information technologies [2].

Electromagnetic radiation, or light, plays a particularly important role in these new technologies.[1] While many quantum objects such as atoms, molecules, ions, and light quanta (commonly called "photons") can be used for quantum information

[1]Light also played an important role in the "first" quantum revolution; it was the inability of classical physics to explain a black-body spectrum that lead Planck to introduce the concept of a quantum of action [3].

processing, only photons are commonly used to transmit quantum information. A good example of this is quantum cryptography, the oldest and most "mature" quantum information technology, where either single photons or entangled pairs of photons are used to transmit information from a sender to a receiver in such a manner that an eavesdropper cannot intercept the information without being detected. Photons are the medium of choice for this and other quantum information transmission applications due to their ability preserve their quantum nature in most situations, fundamentally due to their low decoherence rate in normal environments [4]. This is particularly true when the photons are traveling in optical fiber, allowing them to traverse tens of kilometers and still transmit quantum information at reasonable rates.

Photons have a long and rich history as a resource in quantum information processing, starting with their production and distillation. Although photons can be produced in a variety of systems such as quantum dots [5], NV centers [6], and via single-molecule emission [7], just to name a few, what might be called the modern era of quantum light production began in 1967 with the first reported demonstration of the spontaneous creation of entangled photon pairs [8] (although the effect was predicted much earlier in 1961 [9]). This was accomplished by sending a strong laser pump field into a medium that exhibited second-order $\chi^{(2)}$ properties, where the dielectric polarization P of the material responds to the square of the electric field E, in this case a lithium niobate crystal. Essentially, a small percentage of the pump photons would undergo what is called spontaneous parametric down conversion (SPDC) where those photons were split up into two different, less energetic photons called the "signal" (lower-wavelength) and "idler" (higher-wavelength). The exact wavelength value of the signal and idler photons, along with their degree

of entanglement, depends on the pump wavelength and polarization, and medium dispersion properties. This initial experiment only documented the spontaneous nature (no input signal or idler required) of the effect along with temperature tuning of the signal and idler wavelengths. Later experiments in 1970 showed that the signal and idler fields are created simultaneously to within 4 nanoseconds, the time resolution limit of the detectors [10], revealing the generally entangled nature of the produced pairs. In 1983 the sub-poissonian nature of SPDC was first shown [11]. Also, numerous experiments have shown the generally entangled nature of such, although under particular conditions it is possible to create un-entangled pairs through SPDC [12]. Due to the relative ease and the variety of quantum states that can be produced, SPDC in $\chi^{(2)}$ has been the go-to method for photon production for several decades.

Although SPDC in $\chi^{(2)}$ media is the dominant method for producing quantum states of light, new methods such as production in third-order $\chi^{(3)}$ materials, where the dielectric polarization P is responsive to the third power of the electric field E, show promise for further developing photon production capability. In particular, photon pair generation in optical fiber has been an active topic of research in the past decade. The first verifiable single-photon source created through the third-order nonlinearity in optical fiber was shown in 2002 at telecom wavelengths of around 1550 nm [13]. The physical process used, called spontaneous four-wave mixing (SFWM), was very similar to SPDC; a strong pump laser was coupled into a fiber, initiating a process in which two pump photons were annihilated and two other photons, signal and idler, were created. Since then, SFWM in birefringent fiber [14] and work demonstrating that SFWM in fibers can produce very high purity states [15, 16] has been shown, along with the possibility for the creation of ultra broad-band photon creation [17] via fiber SFWM. Because of the ubiquity, ease of design and ability

to integrate into other devices, optical fiber is quickly becoming one of the leading mediums with which to produce quantum states of light. Part of this dissertation reports on theoretical work carried out by the author and collaborators to discover the optimal conditions for creating pure, non-entangled single-photon states of light in $\chi^{(3)}$ optical fiber. The emphasis is on creating pure states, although it is shown that an arbitrary degree of correlation between the signal and idler can be created, due to the pure states' usefulness in quantum information processing applications such as linear optical quantum computing, which requires the interference of pure states [18]. The work uses an accurate theoretical model of optical fibers [19] to show that under proper conditions, which can be easily engineered through fiber design, very high-purity single-photons with over 99 percent purity can be produced with minimal spectral filtering [15]. Other than the fiber's various properties, the properties of the pump laser field, such as pulse width and central wavelength, determine whether or not the purity conditions can be met.

Equally important to the task of creating highly controlled states of quantum light is the task of manipulating those states to perform useful operations. As other quantum information technologies such as metrology and computation mature, it is likely that remote devices will need to exchange quantum information. Such a network between devices is called a quantum network, and would very likely take the form of multiple devices connected to a system of optical fibers with photons carrying quantum information from device to device [20]. To facilitate device communication in such a system, it would be desirable to have the ability to frequency translate photons, where the photon carrying the quantum information at one central frequency is annihilated and a new photon at a different central frequency carrying the exact same quantum information is created. This would allow, for example, quantum

devices that operate at different optical frequencies to communicate, extending the range of operation of a quantum network by translating the output device photons to telecom wavelength photons where they would suffer lower loss during transmission, and would also allow for better detection of the photons by translating them to a frequency that was optimal for detector operation.

With an eye towards this application, this dissertation is also concerned with the frequency translation of quantum states of light, with an emphasis on translating single-photon states in optical fiber. Frequency translation of quantum states of light has already been accomplished in second-order $\chi^{(2)}$ media, most notably in nonlinear crystals such as beta barium borate and periodically poled lithium niobate. In $\chi^{(2)}$ media, translation is a one-pump process; the pump photons can combine with the input signal photon to create a photon of higher energy than either input field (called sum generation) or the pump and input signal can combine so that the difference of their frequencies creates a new photon (difference generation). In 1992 it was demonstrated that two fields, both originating from a degenerate SPDC process, showed nonclassical intensity correlations after one of the fields underwent the process of frequency doubling (a special case of sum generation) [21]. In 2005 a more general demonstration of frequency translation showed quantum state transfer of a photon at 1312 nm to a photon 712 nm. The photon at 712 nm was then shown to exhibit strong two-photon interference with another photon at 1555 nm that was originally entangled with the photon at 1310 nm [22]. Both of these experiments demonstrated the transfer of entanglement, a very quantum property, from one photon to another; they technically did not demonstrate the single-photon nature of the photons involved. This overlooked feature was only recently demonstrated in 2010, where a photon originally at 1300 nm underwent sum generation converting it to a photon at 710 nm

where a measurement showed that the field was indeed composed of single photons. Translation via difference generation has also been shown recently in 2010 [23]. But as will be discussed more thoroughly in Chapter IV, there are a few significant drawbacks in using $\chi^{(2)}$ media for frequency translation. Most notably, in this case the frequency of the pump laser that drives the translation process must be equal to the difference of the initial (untranslated) and final (translated) photon frequency. For a large frequency/wavlength separation between initial and final central wavelengths, such as hundreds of nanometers in the visible regime, this is not usually difficult. But for close frequency/wavelength separations, such as a few tens of nanometers or less in the visible regime, it can be challenging to find a suitable pump and material that can efficiently accomplish the task. Another difficulty is that nonlinear crystals can be difficult to engineer for use in frequency translation purposes for a particular pair of wavelengths.

The frequency translation process in a third-order $\chi^{(3)}$ material such as fused silica that makes up optical fiber does not suffer from these drawbacks [24]. The process requires two laser fields, and the condition on their frequencies is that the difference of their frequencies must be equal to the difference of the initial and final photon frequencies. Hence there is no particular wavelength the pumps must be; for a small frequency translation the pumps could be at commonly available laser wavelengths such as titanium-sapphire wavelengths, as is the case in the presented experiment. Also, the kind of fiber used in the presented experiment, called photonic crystal fiber, can be engineered to produce a wide range of dispersion profiles, effectively allowing frequency translation to occur anywhere in the visible and infrared regimes [25].

The presented experiment is not the first demonstration of frequency translation in a $\chi^{(3)}$ optical fiber. It was first shown in 1994 for classical telecom-wavelength fields [26]. Since then much interesting work has been done on the subject, mostly in the telecom regime, showing that the process can achieve a low-noise level while effecting a translation efficiency of nearly 100 percent [27–29].

The goal of our experiment was to demonstrate frequency translation of quantum states of light, in particular, single-photon states of light. The goal was achieved as demonstrated by the value of a measurement designed to test if a field consists of quantum states of light called Fock states, which includes single photon states. As will be shown in later chapters, if a second-order correlation measurement carried out on a field has a value of less than 1.0, then the field can be said to be nonclassical. For the translation of a 683 nm photon to a 659 nm photon, we measure a second-order correlation value of 0.21 ± 0.02 and 0.19 ± 0.05, respectively. This corresponds to mean-photon values of $\langle n \rangle_{683} = 1.12$ and $\langle n \rangle_{659} = 1.11$. This shows that both the untranslated field and the translated field are mostly made up of single photons. Also, the efficiency of translation was shown to be around 29 percent. We are happy to claim the endeavor to show quantum translation successful, although there is significant need for improvement in the experiment before we would claim that we have demonstrated a process sufficiently refined enough for quantum information processing tasks.

Although the experimental part of this dissertation is focused on demonstrating quantum frequency translation, experiments concerning a new type of classical frequency translation in optical fiber were also carried out. This was done in part to show the flexibility of the scheme to work at a wide variety of wavelengths, and using diverse phase-matching methods. In all of the above mentioned translation

experiments (including the author's quantum frequency translation), all of the fields involved had the same polarization; when fiber having two polarization axes (birefringent fiber) was used, the fields were incident on the same axes. There is a good reason to do this, as the translation process is about an order of magnitude stronger when all fields are co-polar. But there might be advantages to a scheme in which this is not the case, in particular, where the pump lasers are polarized on one axis and the field to be translated is polarized on the other axis. Although such a configuration suffers from a drop in the translation process strength by nearly an order of magnitude, the Raman gain, generally the most significant noise source in such an experiment, drops by the same magnitude for small shifts (<30 THz) [30, 31] and often drops significantly more for larger shifts. [32]. Therefore this configuration has the potential to minimize noise for large shifts while also allowing for easier filtering of the pump fields via polarization filtering. We demonstrate this "vector" translation process in birefringent fiber; previously vector translation in fiber was only carried out in fiber that was effectively isotropic [27]. We demonstrate 210-nm wavelength translation from 851 nm to 641 nm, or 115 THz in frequency, with an efficiency of around 0.2 percent. This is record translation in both wavelength and frequency, the previous record was 180 nm (26 THz), from 1545 nm to 1365 nm [29].

The rest of this dissertation is organized as follows. In Chapter II we briefly discuss the quantum nature of light theoretically and one method by which to experimentally demonstrate its nonclassical nature. Since Maxwell's equations describe classical light, it is most appropriate to begin from there and derive the canonically quantized theory of light, where the quantum modes of light are associated with states of the quantum harmonic oscillator. This treatment gives particular attention to the state of light called a Fock state, in which the state consists of a

perfectly well defined number of photons. This is a fortunate coincidence, since the experimental work of this dissertation is concerned with demonstrating the translation effect when a single-photon Fock state is transformed into another single-photon state at a differing central frequency. Since we are particularly interested in Fock states, we also present a technique for measuring the degree to which a field is composed of an integer number of photons, called the second-order correlation measurement, or $g^{(2)}$. It is precisely this measurement technique that allows us to distinguish single-photon states from other Fock states and classical light states, such as coherent and thermal states.

Chapter III introduces the medium in which the translation process takes place, optical fiber. While fiber has been used for several decades for telecommunication purposes, it is only in the past couple decades that it has begun to be explored as a nonlinear medium. In fact, part of the reason it is so widely employed in industry is due to its low nonlinearity. But advancements in manufacturing such as precise chemical doping and decreased core diameter have opened up the possibility for fibers to play a central role in the study of nonlinear optics. This chapter focuses on the basic theoretical description of single-mode fibers, both isotropic and polarization maintaining. Special attention is made to the relatively recent invention of a specialty fiber called photonic crystal fiber. This fiber allows for unprecedented engineering of the fiber's dispersion profile, the key property in deciding at what wavelengths nonlinear processes such as frequency translation take place. Both the fibers used in the presented experiment are photonic crystal fibers.

In Chapter IV, some nonlinear effects that occur in optical fibers due to their $\chi^{(3)}$ nature are discussed. This chapter presents the detailed theory of the two important nonlinear process used in this dissertation to demonstrate state translation;

modulation instability and Bragg scattering. Modulation instability is a one-pump process in which two pump photons are annihilated and two new photons are created. This effect is used to create the photons to be translated. The Bragg scattering process is a two-pump process in which one pump photon and one input photon are annihilated and one photon of the other pump and one new photon are created. This is the translation effect; one photon enters the fiber, is annihilated, and one new photon (at a different frequency/wavelength) is created. Also discussed are important phenomena such as Raman scattering and phase modulation. Although very interesting and useful topics in their own right, for the experimental work presented here Raman scattering and phase modulation are essential noise/degrading effects that were avoided to the largest possible extent. Lastly, the two-color Hong-Ou-Mandel effect first predicted by our group [33] is discussed and the probabilities associated with it are calculated in regards to given input and output fields. Interestingly, the classical and quantum terms of the probabilities can be easily identified, with the bosonic nature of the photons accounting for the quantum term.

In Chapter V, the numerical solution to the optical nonlinear Schrödinger equation is discussed. While there are several common methods for accomplishing this, one in particular, the split-step Fourier method, is used most often, and is the method used here and discussed. Numerical integration techniques, such as the Euler, midpoint and Runge-Kutta methods, are also discussed. In terms of consistency and conserving quantities such as field amplitude, it is found that the fourth-order Runge-Kutta methods offer the best performance. These techniques are then applied to the Bragg scattering translation process, and some general properties of the process are discussed in light of the numerical solutions. Also, calculations relating to the two-

color Hong-Ou-Mandel interference effect are presented, and it is shown under what common conditions the effect is discernable.

In Chapter VI, the experimental apparatus, and all associated equipment, is discussed. Along with the hardware, such as lasers, phase-lock loops, single photon detectors, and coincidence counting circuitry, the dispersion and birefringence of the fibers used to produce and translation the photons have been characterized. The technique used to characterize the fibers relies on measuring the modulation instability product as a function of pump frequency. This technique is relatively simple compared to other techniques such as white-light interferometry and produces dispersion profiles and birefringence values that agree reasonably well with other experimentally collected data.

In Chapter VII, the results of the experiment along with a discussion of those results, is presented. It is shown that quantum frequency translation does indeed occur in our experiments and that the quantum states of light that were translated were dominated by the single-photon term. In addition to this central result, we discuss the error and noise in the measurements, the factors determining the translation efficiency, and the task of modeling the results of this experiment. Finally, in Chapter VIII, we summarize our results and give possible future directions for the next generation of quantum translation experiments.

CHAPTER II

QUANTUM LIGHT: THEORY AND MEASUREMENT

As discussed in the introduction, light played an important role in the early development of quantum mechanics. Its important role has by no means come to an end; basic questions such as does the photon have an associated wavefunction, as do "normal" quantum particles like electrons and protons, are still an active topic of research [34–36]. Fortunately, a coherent and well-established formalism describing light as a quantum entity emerged near the end of the foundational years of quantum theory thanks in large part to Dirac [37]. Using his picture-independent notation, he articulated a theory of quantum light through what is now known as canonical quantization. It is so named because this method of quantizing uses the classical Hamiltonian formalism and its features, most notably the canonical Poison brackets, of classical physics to formulate the corresponding quantum theory.

In this chapter we review the a canonically quantized theory of light derived from Maxwell's classical equations for light. It is in no way an exhaustive derivation, and only intended to give the reader the general flavor of the nature of a quantum theory of light. For more substantial treatment the reader is directed to many fine textbooks [3, 38–42] and dissertations [43, 44]. The general idea is to first calculate the discrete traveling mode wave solutions in a defined region, notice the striking similarities of those solutions to those of the quantum harmonic oscillator, and then propose an analogy between the two that gives us a functional theory of traveling light quanta. Also in this chapter, aspects of the measurement of quantum light that are important to understanding the experimental work (as well as to understanding quantum light in general) presented in this dissertation are discussed.

2.1. The Quantization of Light

2.1.1. Classical Light

To achieve a theory of quantum light we begin by stating the equations that define the classical theory of light, Maxwell's equations. Since we will only be exploring the most basic aspects of either theory we will only discuss the free-space versions, and therefore only discuss the electric field $\mathbf{E}$ and magnetic field $\mathbf{H}$, although their non-free-space counterparts, $\mathbf{D}$ and $\mathbf{B}$ respectively, in an uniform medium can also be quantized without excessive difficulty. In SI units Maxwell's equations in free space are

$$\nabla \cdot \mathbf{E} = 0 \tag{2.1}$$

$$\nabla \cdot \mathbf{H} = 0 \tag{2.2}$$

$$\nabla \times \mathbf{E} = -\mu_0 \partial_t \mathbf{H} \tag{2.3}$$

$$\nabla \times \mathbf{H} = \epsilon_0 \partial_t \mathbf{E}, \tag{2.4}$$

where ϵ_0 is the permittivity of free space, μ_0 is the permeability of free space, and the symbol ∂_t is the partial derivative with respect to time operator. The vector potential $\mathbf{A}$ is often defined in connection with the $\mathbf{E}$ and $\mathbf{H}$ fields because in many circumstances it is simpler to work with. It is defined by the equations

$$\begin{aligned} \mathbf{E} &= -\partial_t \mathbf{A} \\ \mathbf{H} &= \nabla \times \mathbf{A}. \end{aligned} \tag{2.5}$$

In quantum optics it is conventional to employ the Coulomb gauge where $\nabla \cdot \mathbf{A} = 0$.

By combining Maxwell's equations and using the vector identity $\nabla \times (\nabla \times \mathbf{E}) = \nabla(\nabla \cdot \mathbf{E}) - \nabla^2 \mathbf{E}$ we arrive at the famous free space traveling wave solution for the electric (or vector potential)

$$\nabla^2 \mathbf{E} - \frac{1}{c^2}\partial_t^2 \mathbf{E} = 0 \qquad \text{or} \qquad \nabla^2 \mathbf{A} - \frac{1}{c^2}\partial_t^2 \mathbf{A} = 0 \tag{2.6}$$

where the speed of light in vacuum is $c = (\mu_0 \epsilon_0)^{-1/2}$.

Now consider a cubic region of space with sides of length L and total volume V. Were we content to study static solutions to Maxwell's equations we would make the sides of the box perfectly conducting, which would allow us to derive the standing modes. But since we would like to study light, which is always on the move, our interest principally lies with traveling-wave solutions. To satisfy our need for boundary conditions and traveling solutions, we chose only periodic boundary conditions at the sides. Under these conditions the general solution to (2.6) for the vector field is given by a sum of modes

$$\mathbf{A}(\mathbf{r}, t) = \sum_{\mathbf{k}} \sum_{p=1,2} \mathbf{e}_p \left(f_{\mathbf{k}p} e^{i\mathbf{k}.\mathbf{r} - i\omega_k t} + f^{\dagger}_{\mathbf{k}p} e^{-i\mathbf{k}.\mathbf{r} + i\omega_k t} \right) \tag{2.7}$$

where $\mathbf{k}$ is the discrete wavevector and $\mathbf{e}_p$ refers to the field polarization, which has two components. Each spatial component $k_{x,y,z}$ of the wavevector can have values of $k_i = 2\pi n_i / L$, where n_i can be zero or any negative or positive integer. The angular frequency is $\omega_k = c|\mathbf{k}| = ck$. Here $f_{\mathbf{k}p}$ is the mode amplitude and is implicitly a function of wavevector and polarization direction. The electric and magnetic fields are found by evoking (2.5) and found to be

$$\mathbf{E}(\mathbf{r},t) = i\sum_{\mathbf{k}}\sum_{p=1,2}\omega_k \mathbf{e}_p\left(f_{\mathbf{k}p}e^{i\mathbf{k}.\mathbf{r}-i\omega_k t} - f^{\dagger}_{\mathbf{k}p}e^{-i\mathbf{k}.\mathbf{r}+i\omega_k t}\right) \tag{2.8}$$

$$\mathbf{H}(\mathbf{r},t) = i\sum_{\mathbf{k}}\sum_{p=1,2}\mathbf{k}\times\mathbf{e}_p\left(f_{\mathbf{k}p}e^{i\mathbf{k}.\mathbf{r}-i\omega_k t} + f^{\dagger}_{\mathbf{k}p}e^{-i\mathbf{k}.\mathbf{r}+i\omega_k t}\right) \tag{2.9}$$

The classical Hamiltonian, and total energy, for a field is given by the general expression

$$\mathcal{H} = \frac{1}{2}\int_V d\tau(\epsilon_0 E^2 + \mu_0 H^2). \tag{2.10}$$

Plugging in expressions (2.8) and (2.9) we find the Hamiltonian reduces to a sum of the time independent amplitude modes

$$\mathcal{H} = \epsilon_0 V\sum_{\mathbf{k}}\sum_{p=1,2}\omega_k^2(f_{\mathbf{k}p}f^{\dagger}_{\mathbf{k}p} + f^{\dagger}_{\mathbf{k}p}f_{\mathbf{k}p}). \tag{2.11}$$

Of course the two terms in the parenthesis could be combined since they are just scalars. They are written as such because in the next section we will see a striking similarity between this classical expression of traveling waves and one relating to the quantum mechanical oscillator written with the inclusion of operators that cannot be combined so easily.

2.1.2. Light as Harmonic Oscillator

Recall the quantum harmonic oscillator [45, 46] in which a particle of mass m is trapped in an one-dimensional potential quadratic in the position operator $\hat{q}$. The solution leads to a Hamiltonian of the form

$$\hat{\mathcal{H}}_{HO} = \frac{\hat{p}^2}{2m} + \frac{1}{2}m\omega^2\hat{q}^2 \tag{2.12}$$

with $\hat{p}$ being the momentum operator and satisfying the commutation relation $[\hat{q}, \hat{p}] = i\hbar$. For reason that will soon become clear we define another set of operators in relation to the momentum and position operators:

$$\hat{a} = (m\omega\hat{q} + i\hat{p})/\sqrt{2m\hbar\omega} \tag{2.13}$$

$$\hat{a}^\dagger = (m\omega\hat{q} - i\hat{p})/\sqrt{2m\hbar\omega}. \tag{2.14}$$

These operators are usually called the annihilation and creation operators respectively, and often written in relation to the so-called quadrature operators $\hat{X}$ and $\hat{Y}$, which will be important in understanding the field uncertainty relations.

$$\hat{X} = \frac{1}{2}(\hat{a}^\dagger + \hat{a}) \tag{2.15}$$

$$\hat{Y} = \frac{1}{2}(\hat{a}^\dagger - \hat{a}) \tag{2.16}$$

Interestingly, the Hamiltonian operator can be expressed with creation/annihilation or quadrature operators compactly as

$$\hat{\mathcal{H}}_{HO} = \hbar\omega(\hat{a}^\dagger\hat{a} + \frac{1}{2}), \tag{2.17}$$

$$\hat{\mathcal{H}}_{HO} = \frac{1}{2}\hbar\omega(\hat{a}\hat{a}^\dagger + \hat{a}^\dagger\hat{a}) \qquad \text{or} \tag{2.18}$$

$$\hat{\mathcal{H}}_{HO} = \hbar\omega(\hat{X}^2 + \hat{Y}^2). \tag{2.19}$$

The expression of (2.18) presents the clearest connection between the quantum harmonic oscillator and the classical light field of the previous section; their

Hamiltonians are very similar. In fact, if we equate (2.17) with (2.11) we find that

$$f_{\mathbf{k}p} \longrightarrow (\hbar/2\epsilon_0 V\omega_k)^{1/2}\hat{a}_{\mathbf{k}p} \tag{2.20}$$

$$f^{\dagger}_{\mathbf{k}p} \longrightarrow (\hbar/2\epsilon_0 V\omega_k)^{1/2}\hat{a}^{\dagger}_{\mathbf{k}p}, \tag{2.21}$$

where the annihilation and creation operators are labeled with wavevector and polarization parameters. As we will see, these quantum operators are well suited to representing light and have many desirable properties: a Hamiltonian structure much like classical light, operators to create and annihilate quanta of light, a natural zero-point energy, etc. From here on we associate quantum light with modes of the quantum-mechanical harmonic oscillator that has been quantized so as to keep as much of the nature of classical light as is possible. Many of their important quantum properties are manifest in their commutation relations, which are responsible for the various uncertainty relations they adhere to in different contexts.

$$[\hat{a}_{\mathbf{k}p}, \hat{a}^{\dagger}_{\mathbf{k}'p'}] = \delta_{\mathbf{k}\mathbf{k}',pp'} \tag{2.22}$$

$$[\hat{a}_{\mathbf{k}p}, \hat{a}_{\mathbf{k}'p'}] = 0 \tag{2.23}$$

2.2. Specific States of Quantum Light and Their Measurement

The simplest, most intuitive and arguably the most "quantum" states of light is the number state, or Fock state, $|n\rangle$. It describes a field consisting of a perfectly well defined non-negative integer number n of light quanta. This field cannot be split in the conventional sense of the term; a number state incident on a 50/50 beamsplitter does not simply divide into two equal and well defined amplitude parts like a classical field would. For a single quantum incident on said beamsplitter with detectors measuring

the output, it doesn't divide at all! The number state doesn't have a well-defined phase, unlike a classical field, due to the amplitude-phase uncertainty principle [38]. Owing to these properties among others, the number state is often the state of choice in experiments that aim to highlight the difference between quantum and classical theory. In this section we briefly demonstrate how the number state arises from the harmonic oscillator model of quantum light and demonstrate how two classical fields, the coherent and thermal fields, can be described as a superposition of number states. This points to the fact that not only does quantum mechanics predict differing phenomenon from classical theory but what it doesn't contradict it can explain equally well on its own terms.

We will also consider aspects of the theory of measuring Fock states, particularly the number state. One of the first and defining experiments in quantum optics was the measurement and determination of the single-photon state $|1\rangle$ [47]. This state, and its measurement, features prominently in this dissertation, as its creation and frequency translation is the reason for this exposition.

2.2.1. Number, Coherent and Thermal States

Consider only a single quantized mode of the field, implying a single frequency, while dropping the $\mathbf{k}$ and p subscripts. Then let a state we will call the number state $|n\rangle$, which is indexed by an integer n, be an eigenstate of the Hamiltonian of the field given by (2.17).

$$\hat{\mathcal{H}}|n\rangle = \hbar\omega\left(\hat{a}^\dagger\hat{a} + \frac{1}{2}\right)|n\rangle = E_n|n\rangle. \tag{2.24}$$

What effect does the creation or annihilation operator have on $|n\rangle$? If we act with the creation operator on $|n\rangle$ and use the commutation relation of (2.22) and (2.23)

we see

$$\hat{\mathcal{H}}\hat{a}^\dagger|n\rangle = (E_n + \hbar\omega)\hat{a}^\dagger|n\rangle. \tag{2.25}$$

This means that the state that we will call $|n+1\rangle$ is also an energy eigenstate of the Hamiltonian with energy $E_{n+1} = E_n + \hbar\omega$, where

$$|n+1\rangle = \frac{\hat{a}^\dagger}{\alpha_{n+1}}|n\rangle \tag{2.26}$$

and α_{n+1} is a yet to be determined normalization constant. In terms of energy it is clear that acting with the creation operator on a number state increases the amount of energy in the field by an amount $\hbar\omega$. One could carry out a similar procedure with the annihilation operator and find it decreases the amount of energy in the field by the same magnitude. Of course there gets to a point where further "lowering" of the field would produce negative energy. Since it is unclear what to make of a negative energy, that by *fiat* we do not allow, we therefore have the condition $\hat{a}|0\rangle = 0$ where $|0\rangle$ is the lowest possible state of the field. This has the curious consequence that the lowest energy of the field is non-zero, since $\hat{\mathcal{H}}|0\rangle = \frac{1}{2}\hbar\omega$. There are many interesting consequences of this so-called "zero-point energy" [48] but discussion of it is unfortunately beyond the scope of this dissertation. As an aside, we now know n must be a non-negative integer.

From the above properties we can now deduce the form of E_n as a function of n, which with comparison with to (2.25) leads us to the conclusion that

$$E_n = \hbar\omega(n + \frac{1}{2}) \qquad \Rightarrow \qquad \hat{a}^\dagger\hat{a}|n\rangle = \hat{n}|n\rangle = n|n\rangle. \tag{2.27}$$

The operator $\hat{n}$ is called the number operator since when acting on the number state it has an eigenvalue of the integer n, the multiple of $\hbar\omega$ units of energy in the field. By identifying a quanta of light, the photon, with an $\hbar\omega$ unit of field energy we can now say the number operator yields the number of photons in the field when acting on the numbers state. With the discovery of the number operator we can now determine the coefficient of the creation (and annihilation) operator in (2.26).

$$\hat{a}^\dagger|n\rangle = \sqrt{n+1}|n+1\rangle \tag{2.28}$$

$$\hat{a}|n\rangle = \sqrt{n}|n-1\rangle \tag{2.29}$$

We now write a numbers state in terms of the $n = 0$ "vacuum" state, which will be a valuable relation when considering the creation of photon states through spontaneous generation.

$$|n\rangle = \frac{(\hat{a}^\dagger)^n}{\sqrt{n!}}|0\rangle. \tag{2.30}$$

The number states make up a complete basis, with the identity being

$$\sum_{n=0}^{\infty} |n\rangle\langle n| = \mathbf{1}. \tag{2.31}$$

A general state of the field may contain multiple numbers states in superposition, although this state is not strictly speaking a number state since it is composed of an ambiguous number of photons. Such a state can be written as $|\psi\rangle = \sum_n c_n|n\rangle$, where $|c_n|^2$ is the probability of detecting n photons if the state is measured. This notation can also describe multiple fields through use of the direct product. In general the

overall state of m fields can be written as

$$|\Psi\rangle = \sum_m \sum_n c_{1,n}|n\rangle_1 \otimes c_{2,n}|n\rangle_2 ... \otimes c_{m,n}|n\rangle_m = \sum_m \sum_n c_{1,n}|n\rangle_1 c_{2,n}|n\rangle_2 ... c_{m,n}|n\rangle_m. \tag{2.32}$$

The above expressions assumed a monochromatic field and we will continue with such a limitation through the rest of the chapter. It is not difficult to include discrete or continuous multi-frequency fields; the appropriate sum or integral (and appropriate weighting function) is simply incorporated in the above expressions.

Having a general expression for the fields such as (2.32) allows us to consider classical fields from a quantum perspective. In particular we would like to understand the quantum state that most closely resembles the classical traveling electromagnetic wave given by the solution of (2.6). This field classically has well defined amplitude and phase for every point in time, hence it is the most "coherent" of fields and describes the output of a monochromatic laser. This exact description has no analog in quantum theory due to the fact that an uncertainty relation between the amplitude and phase of a field exists, given by [38]

$$\Delta n \Delta \phi \geq \frac{1}{2}, \tag{2.33}$$

where Δn and $\Delta \phi$ refer to the variance of the photon number and variance of the phase of the field, respectively. For different fields, or rather different distributions of numbers states, Δn and $\Delta \phi$ take on different values. For a field consisting of a particular number state $|n\rangle$ the variance in the photon number is zero, implying that the variance in the phase is infinite. While this state succeeds at describing the well-defined amplitude nature of a classical wave it fails completely in describing its well-defined phase nature. Clearly there must be compromise allowing some uncertainty

in both amplitude and phase. On a deeper level this uncertainty relation derives from the commutation relation between field quadratures $\hat{X}$ and $\hat{Y}$, as defined in (2.15) and (2.16), given by

$$[\hat{X}, \hat{Y}] = i/2. \tag{2.34}$$

A reasonable suggestion for the "most certain" state would be a state that not only obeys the minimum uncertainty value of 1/2 for (2.33) but also as the property that the variances of $\hat{X}$ times $\hat{Y}$ equal the smallest possible amount. In this case $\hat{X}$ and $\hat{Y}$ are equal in magnitude. This state represents the closest thing to a classically coherent state and therefore in the quantum parlance is called the "coherent state" and written as $|\alpha\rangle$.[1] In terms of a sum of numbers states the normalized coherent state is given by

$$|\alpha\rangle = e^{-|\alpha|^2/2} \sum_{n=0}^{\infty} \frac{\alpha^n}{\sqrt{n!}} |n\rangle = e^{-|\alpha|^2/2} (e^{\alpha \hat{a}^\dagger} |0\rangle). \tag{2.35}$$

As it turns out, $|\alpha\rangle$ is an eigenstate of annihilation operator having eigenvalue α

$$\hat{a}|\alpha\rangle = \alpha|\alpha\rangle. \tag{2.36}$$

Using this fact we see $\langle\alpha|\hat{a}^\dagger\hat{a}|\alpha\rangle = |\alpha|^2$, and recognizing $\hat{a}^\dagger\hat{a}$ as the number operator it is clear that $|\alpha|^2$ is equal to the mean number of photons in the state $\langle n\rangle$, which is also equal to the square of the variance in photon number $(\Delta n)^2$ and need not be an integer number. The defining feature of a coherent state is this $|\alpha|^2$ value, which dictates the form of the probability distribution. This is found by evaluating

[1] Coherent states can also be used as a complete basis state to describe a state of light using the Glauber-Sudarshan P-representation [49].

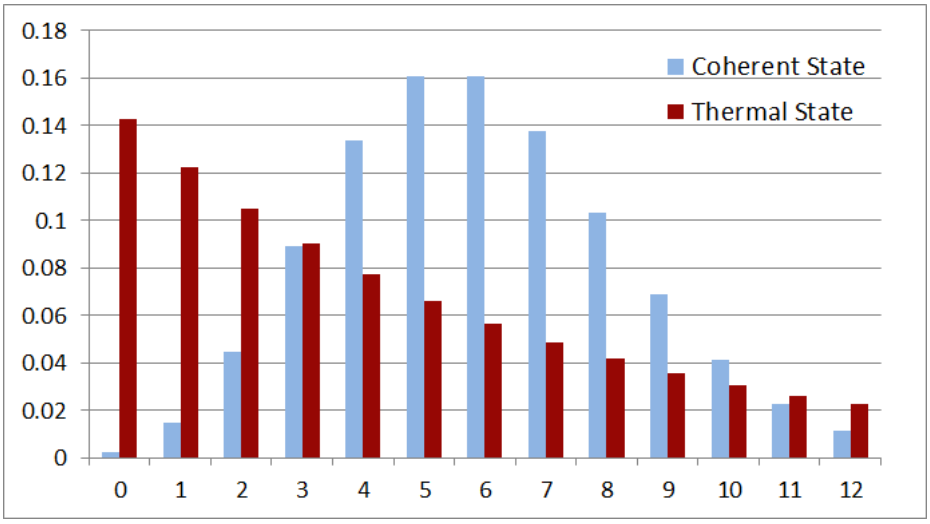

FIGURE 2.1. Coherent (light blue) and Thermal (dark red) probability distributions for $\langle n \rangle = 6$.

the expectation value of the coherent state operator with respect to a number state

$$P(n)_{cs} = \langle n|\alpha\rangle\langle\alpha|n\rangle = \frac{e^{-\langle n\rangle}\langle n\rangle^n}{n!}, \tag{2.37}$$

which is a Poisson distribution in number state. As to be expected, this distribution has a maximum at $\langle n \rangle$ (except for $\langle n \rangle \leq 1$) and quickly dies off for n away from this value. For large values of $\langle n \rangle$ this distribution becomes Gaussian. Figure 2.1. shows $P(n)_{cs}$ for $\langle n \rangle = 6$.

In stark contrast to the coherent state with its minimum uncertainty properties is another classical state called thermal light. As its name suggest this is the chaotic state that arises from a system that has an overall temperature T, but here the system is that of a harmonic oscillator representing the number of photons in a field. Like an ordinary black body, the oscillator can be found in the n^{th} energy state with

probability $p(n)$ given by

$$p(n) = e^{-E_n/k_BT} / \sum_{n=0}^{\infty} e^{-E_n/k_BT}, \tag{2.38}$$

where k_B is the Boltzmann constant. Using the quantized expression for the possible energy of the oscillator given by $E_n = \hbar\omega(n + \frac{1}{2})$ and summing the geometric series, $p(n)$ can be reduced to

$$p(n) = (1 - e^{-\hbar\omega/k_BT})e^{-n\hbar\omega/k_BT}. \tag{2.39}$$

The mean photon number in the field $\langle n \rangle$ can be found by taking the expectation value of n weighted by $p(n)$, which can then can be inverted and integrated into (2.39) to yield $P(n)_{ts}$, the probability number distribution as a function of mean photon number of the thermal state.

$$\langle n \rangle = \sum_n np(n) = \frac{e^{-\hbar\omega/k_BT}}{1 - e^{-\hbar\omega/k_BT}} \qquad \Rightarrow \qquad P(n)_{ts} = \frac{\langle n \rangle^n}{(1 + \langle n \rangle)^{n+1}} \tag{2.40}$$

Figure 2.1. shows $P(n)_{ts}$ for $\langle n \rangle = 6$ contrasted with $P(n)_{cs}$ with the same photon number. As is clear, the photon distribution of $P(n)_{ts}$ is much more spread out than that of $P(n)_{cs}$. Consequently, Δn is larger, given by

$$\Delta n = \left(\langle n \rangle^2 + \langle n \rangle \right)^{1/2} \tag{2.41}$$

Because of this larger Δn, this type of distribution is called super-Poissonian. By contrast, a number state, which has $\Delta n = 0$, is sub-Poissonian.

This state has an important role in the work presented in this dissertation. For values of $\langle n \rangle \ll 1$, the thermal probability distribution is well approximated by

$P(n)_{ts} \approx \langle n \rangle^n$, and hence the thermal state is given by

$$\psi_{ts} \approx |0\rangle\langle 0| + \langle n \rangle |1\rangle\langle 1| + \langle n \rangle^2 |2\rangle\langle 2| + \dots . \tag{2.42}$$

This will be the state of the field that is created by the nonlinear fiber processes, and its form will have implications for type of measurements needed to show that a (mostly) single-photon state of light is present.

2.2.2. Degrees of Coherence and Quantum Light

The phenomenon of interference and correlation of fields of light are at the heart of the experimental understanding of both classical and quantum light. While direct measurement of an optical field is often at very challenging task, owing to the large group velocity, phase velocity, and frequency of light, measuring either the interference or correlation with "slow" photodetectors of two field (often time-displaced copies of one another) can reveal nearly as much information about the fields being measured as direct measurement could. Young's double-slit experiment [50], Michelson's various interferometers [51, 52], the Hanbury-Brown Twist interferometer [53], Grangier's single-photon experiments [47] and other interferometric/correlation works that were responsible for major advancements in the field of physics come readily to mind.

We focus our attention on two types of correlation measurements motivated by three of the above mentioned experiments. The first measures correlations between electric fields. Consider Young's double-slit experiment, pictured in Figure 2.2.(a), where a plane wave is incident on a screen with two slits at positions P_1 and P_2, and measured by a detector at position P_D on a second screen. The electric field at P_D and time t will be a sum of the electric fields exiting the slits at P_1 and P_2, delayed

by times t_1 and t_2 respectively;

$$\mathbf{E}(P_D, t) = C_1\mathbf{E}(P_1, t_1) + C_2\mathbf{E}(P_2, t_2), \tag{2.43}$$

where C_1 and C_2 are amplitude constants. The detector will measure the time-average intensity as

$$\langle I(P_D, t)\rangle = \epsilon_0 c\langle \mathbf{E}^*(P_D, t)\mathbf{E}(P_D, t)\rangle \tag{2.44}$$

$$= \epsilon_0 c\left\langle |C_1\mathbf{E}(P_1, t_1)|^2 + |C_2\mathbf{E}(P_2, t_2)|^2 + 2\mathrm{Re}[C_1\mathbf{E}^*(P_1, t_1)C_1\mathbf{E}(P_2, t_2)]\right\rangle \tag{2.45}$$

The first two terms are just the intensity of the individual fields but the third term includes both of the fields and gives rise to interference fringes. This term is directly proportional to the "first-order correlation function"

$$\langle \mathbf{E}^*(x, t_1)\mathbf{E}(x, t_2)\rangle = \frac{1}{T}\int_T dt_1 \mathbf{E}^*(x, t_1)\mathbf{E}(x, t_2). \tag{2.46}$$

Although there are two time variables in the expression only one needs to be integrated over since only the time difference $\tau = t_2 - t_1$ matters. Rewriting (2.46) in terms of τ and normalizing the function gives the so-called "degree of first-order coherence,"

$$g^{(1)}(x, \tau) = \frac{\langle \mathbf{E}^*(x, t)\mathbf{E}(x, t + \tau)\rangle}{\langle \mathbf{E}^*(x, t)\mathbf{E}(x, t)\rangle}. \tag{2.47}$$

The $g^{(1)}$ function can be understood physically as a measure of the fields' ability to effectively interfere with one another. To this end a quantity often called the

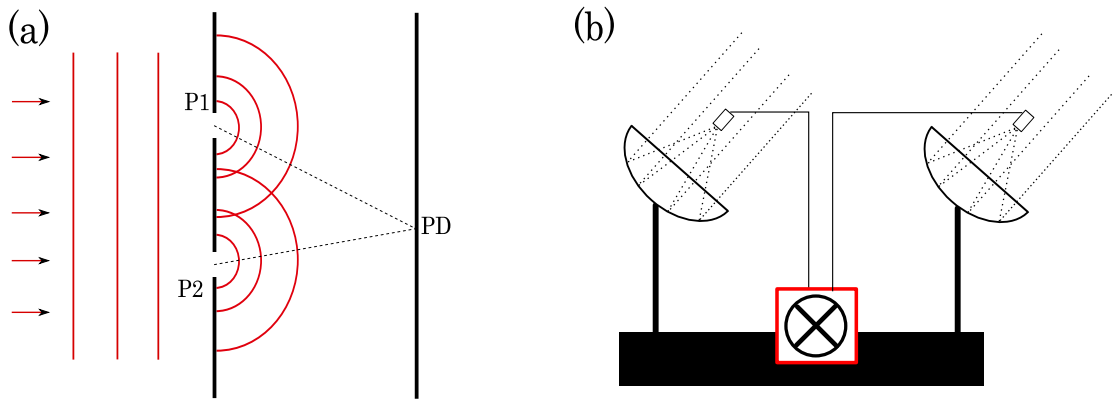

FIGURE 2.2. Measuring the first and second order correlation functions. (a) Young's double-slit experiment, which can be used to measure the first-order correlation function of a field. (b) The HBT interferometer, which measured the second-order correlation between two fields. It was first used to measure properties of stars and the measurement it made did not suffer significantly from atmospheric turbulence.

"visibility" is defined as

$$V = \frac{\langle I(x,t)\rangle_{max} - \langle I(x,t)\rangle_{min}}{\langle I(x,t)\rangle_{max} + \langle I(x,t)\rangle_{min}}, \tag{2.48}$$

where $\langle I(x,t)\rangle_{max}$ and $\langle I(x,t)\rangle_{min}$ are the maximum and minimum intensities on the far screen near the point x, where interference effects might occur. If the intensities reaching x from the two slits are equal then V is simply equal to the magnitude of $g^{(1)}(x,\tau)$. If the wave is highly coherent and able to interfere with itself then $|g^{(1)}(x,\tau)| \cong 1$, if it is completely incoherent then $|g^{(1)}(x,\tau)| \cong 0$, and the intermediate case between zero and one denotes a partially coherent incoming wave.

The quantity $g^{(1)}$ has many interesting and useful properties, but it is not used to measure quantum light. If the fields emanating from P_1 and P_2 have identical spectral properties then $g^{(1)}$ cannot distinguish between number, coherent or thermal states of light [3]. For that we will need a measure that correlates the intensities of two fields, not the correlations of the fields themselves, in a measurement called the

"degree of second-order coherence," or in its normalized version, $g^{(2)}$. Historically, $g^{(2)}$ came to prominence when Hanbury-Brown and Twiss (HBT) devised a new type of stellar interferometer that measured the intensity correlations between two earth-based detectors [53], pictured in Figure 2.2.(b). Before this, an interferometer designed by Fizeau and built and operated by Michelson [3] was used to measure the width of stars by interfering light from different parts of the star together on one detector [54]. This clever scheme had one significant flaw, its measurements were sensitive to the phase disturbances the atmosphere would impart to the incoming electric fields. Since the value of intensity doesn't change if the field's phase is altered, the HBT interferometer got around this by measuring intensity correlations.

Consider two incoming fields produced by a distant star that have slightly different wavevectors $\mathbf{k}$ and $\mathbf{k}'$ that fall onto detectors positioned at $\mathbf{r}_1$ and $\mathbf{r}_2$. The intensity on either detector at time t is

$$I(\mathbf{r}_i, t) = \epsilon_0^2 c^2 \left(|\mathbf{E}(\mathbf{k}, t)|^2 + |\mathbf{E}(\mathbf{k}', t)|^2 + 2\mathrm{Re}[\mathbf{E}(\mathbf{k}, t)\mathbf{E}(\mathbf{k}', t)] \right) \tag{2.49}$$

The time average value of the two intensities measured at the detector is found to be

$$\begin{aligned} \langle I(\mathbf{r}_1, t) I(\mathbf{r}_2, t) \rangle = & \left\langle \epsilon_0^2 c^2 (|\mathbf{E}(\mathbf{k}, t)|^2 + |\mathbf{E}(\mathbf{k}', t)|^2)^2 \right\rangle \\ & + \epsilon_0^2 c^2 \left\langle |\mathbf{E}(\mathbf{k}, t)|^2 |\mathbf{E}(\mathbf{k}', t)|^2 \cos[(\mathbf{k} - \mathbf{k}') \cdot (\mathbf{r}_1 - \mathbf{r}_2)] \right\rangle \end{aligned} \tag{2.50}$$

which is equal to the degree of second-order coherence. Notice that the only phase term present depends on the difference of incoming $\mathbf{k}$ vectors, not the sum. This is the key difference between the Michelson and HBT interferometers; Michelson's had terms proportional to the sum of the $\mathbf{k}$ vectors, which is sensitive to phase

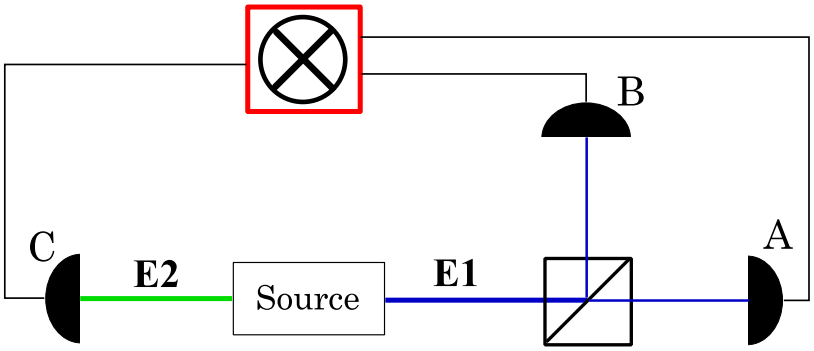

FIGURE 2.3. The Grangier adaptation of the HBT interferometer, used to measure the second-order correlation function of quantum light. In the case of heralded states, the measurements of detectors A and B are conditioned by a positive event measurement by detector C.

disturbance, whereas the HBT device subtracts out any phase disturbances. This leads to improvements in angular resolution by about a factor of 400 [3].

The $g^{(2)}$ function can be defined more generally for intensity correlations between detectors where one signal is time delayed by an amount τ. In this case

$$g^{(2)}(\mathbf{r}_1, \mathbf{r}_2, \tau) = \frac{\langle I(\mathbf{r}_1, t) I(\mathbf{r}_2, t+\tau) \rangle}{I_1 I_2} = \frac{\langle \mathbf{E}^*(\mathbf{r}_1, t) \mathbf{E}^*(\mathbf{r}_2, t+\tau) \mathbf{E}(\mathbf{r}_2, t+\tau) \mathbf{E}(\mathbf{r}_1, t) \rangle}{I_1 I_2} \tag{2.51}$$

where I_1 and I_2 are the time averaged values of the intensity at detectors 1 and 2. The $g^{(2)}$ function is written with the electric fields for the detector at time t ordered so that this classical expression will align more closely with the quantum expression.

Now consider the variation of the HBT interferometer developed by Grangier *et al.* [47] pictured in Figure 2.3.. Here a field E_1 from a source is incident on a beamsplitter, the output of which is monitored by two detectors A and B that measure the intensity as a function of time (detector C need not be considered yet). Since the detectors are measuring a field that comes from the same source, their relative position only matter in so far as there is a time delay between the arrivals of the respective fields. Hence $g^{(2)}$ is only a function of τ, and all other parameter

dependence will be suppressed. There are several important properties of $g^{(2)}$ [38]. The function is time symmetric so that $g^{(2)}(-\tau) = g^{(2)}(\tau)$ and the value of $g^{(2)}$ for $\tau = 0$ has the property that $g^{(2)}(\tau \neq 0) \leq g^{(2)}(0)$. But the most important property that relates to distinguishing classical and quantum light is that $g^{(2)}(0)$ for any incident classical field is greater than or equal to one.

$$1 \leq g^{(2)}(0) \tag{2.52}$$

This is only true for $\tau = 0$, when $\tau \neq 0$ $g^{(2)}$ must simply be greater than or equal to zero, with no upper bound.

With (2.51) in hand we could easily evaluate $g^{(2)}(\tau)$ for the classical coherent and thermal states, but not the number state. Hence we need an appropriate expression for $g^{(2)}$ in terms of quantum operators. Luckily (2.51) is written in a manner that can easily be converted into quantum notation. For a single-mode field the normal-order expression is given by

$$g^{(2)}(\tau) = \frac{\langle \hat{a}^\dagger(t)\hat{a}^\dagger(t+\tau)\hat{a}(t+\tau)\hat{a}(t)\rangle}{\langle \hat{a}^\dagger(t)\hat{a}(t)\rangle^2}. \tag{2.53}$$

What is left to do is to evaluate $g^{(2)}(0)$ for the coherent, thermal states, and number states. For reference, we include the $g^{(2)}$ value for any single-mode field. It can be shown that the results for such states that have a mean photons number $\langle n \rangle$

and mean squared photon number $\langle n^2 \rangle$ are:

$$g^{(2)}_{cs}(0) = 1 \tag{2.54}$$

$$g^{(2)}_{ts}(0) = 2 \tag{2.55}$$

$$g^{(2)}_{ns}(0) = 1 - \frac{1}{\langle n \rangle} \tag{2.56}$$

$$g^{(2)}_{smf}(0) = \frac{\langle n^2 \rangle - \langle n \rangle}{\langle n \rangle^2}. \tag{2.57}$$

Surprisingly, both the values of $g^{(2)}(0)$ for both classical states are independent of the mean photon number, while for the quantum state it is highly dependent. Not surprisingly, both classical states satisfy the condition of equation (2.52) whereas the quantum state does not. For all values of $\langle n \rangle$ the number state is less than 1, a clear break from classical theory. The particular value of $g^{(2)}(0)$ leads to useful information about the number state present. The $g^{(2)}(0)$ measurement is ubiquitous in quantum optics experiments due to its ability to clearly distinguish between not only classical and quantum light, but also between kinds of quantum light.

Before the conclusion of this chapter it is important to note why the third detector in the Grangier interferometer, C in Figure 2.3., is necessary. Many processes used to create photons, like radiative cascades in Grangier's experiments, nonlinear crystals, and optical fibers in work presented in this dissertation, usually create photons in pairs. The pairs can be either frequency degenerate or have different frequencies. More importantly, the process creates a long-tailed number distribution that contains in theory an infinite number of higher order terms (although the probabilities become vanishingly small for high numbers). For example, only considering number states, the quantum state for a parametric generation process

might look something like this for modes 1 and 2:

$$|\psi\rangle \cong |0\rangle_1|0\rangle_2 + \epsilon|1\rangle_1|1\rangle_2 + \epsilon^2|2\rangle_1|2\rangle_2 + \ldots, \tag{2.58}$$

where ϵ is much less than one. For each mode considered separately, when the other mode is traced out[2], the state is thermal, an essentially classical state of light, and a $g^{(2)}$ measurement on either mode will only produce values greater than or equal to one. So how do these sources provide quantum light? The key is that one of these photons is used to *herald* the existence of the other photon, which then projects the non-detected mode into a nearly single photon state. If we set the apparatus up, like in Figure 2.3., where mode 1 is directed towards the beamsplitter and photon 2 is directed towards detector C, then a positive detection event of detector C tells us that the quantum state, initially state (2.58), does not contain a vacuum $n = 0$ term. Upon renormalizing, the $|1\rangle_1|1\rangle_2$ term is the dominant term, and therefore the post-heralded state is most likely in the single-photon state for the remaining mode, mode 1. For the type of detectors commonly used currently, avalanche photodiodes run in Geiger mode, which only register the presence of zero or non-zero intensity ("no click" or "click"), the expression for $g^{(2)}(0)$ is given by

$$g^{(2)}(0) = \frac{N_{ABC}N_C}{N_{AC}N_{BC}}, \tag{2.59}$$

where A and B label the detectors monitoring the output of the beamsplitter, and C labels the heralding detector. The quantities N_i, N_{ij}, N_{ijk} are the number of single, double coincidence and triple coincidence events between detectors i, j and k over the time interval of the data collection, respectively [47, 55].

[2]For example, the density matrix of mode 1 by itself is $\rho_1 = \mathrm{Tr}_2[|\psi\rangle\langle\psi|]$.

CHAPTER III

OPTICAL FIBER

Optical fibers have become the default medium for transmitting large amounts of data long distances for two principle reasons: the physical object they guide, light, travels very fast and does not strongly interact with itself, and the light it transfers is attenuated only by a very small amount. Nearly three decades ago it was shown that light attenuation in a research-grade optical fiber was ≈ 0.154 dB/km, which is an approximate 3.6 percent attenuation per kilometer, at a wavelength of 1550 nm [56]. At that rate light will drop to only half its intensity at about 20 km! But long-haul communications are not the only application of optical fiber. As we will see in detail in the next chapter, fibers can be used as active elements that can create and manipulate light in fascinating ways.

In this chapter a basic introduction to fiber optics is given, paying particular attention to the quantities that are of particular importance to work presented in this dissertation (with the exception of nonlinear effects, which will be dealt with in the next chapter). The "regular" types of fiber optics, step-index and graded-index, will be discussed followed by a discussion of the type of fiber used in the current work, Photonic Crystal Fiber (PCF). We will cover only the most basic aspects of these topics; the interested reader will find much more detail in such texts books as [57–60] and many others.

3.1. Basic Concepts

3.1.1. Step/Graded Index Fibers and Modes

An optical fiber can accurately be described as a cylindrical waveguide composed of two main fused-silica based components; the core, in which the light is guided down, and the cladding, which surrounds the core and enables core-guidance and isolation from the outside environment. Usually there is a "jacket" that surrounds the cladding, used to protect the core and cladding from mechanical damage and often made out of some kind of plastic, but it does not generally affect the waveguiding properties of the fiber. The guided light in the core travels in the form of modes that have differing transverse spatial profiles, polarizations, and group velocities. While all standard fibers guide both modes of polarization not all fibers guide all possible spatial profiles. Fibers are often categorized by whether or not they guide only the fundamental single mode, which has a Bessel intensity profile, or a larger number of modes that in general can be described as a combination of Bessel and modified Bessel functions. These two modes of operation are called single-mode and multimode, respectively. The characterization is highly wavelength dependent; the same fiber might be single mode for one wavelength but multimode for a shorter wavelength.

As far as physical geometry of the core and cladding, standard optical fibers are broken up into two distinct categories; step-index and graded-index. A schematic of a step-index fiber is shown in Figure 3.1.(a). Here the core is uniform in composition on a macroscopic scale but uniformly doped with chemicals (often germanium) so that it has a slightly higher index of refraction n_1 than that of fused silica. The cladding is generally just fused silica and has a cladding index of n_2, which helps to define the index contrast $\delta = n_1 - n_2$. The two index parameters, along with the core radius a,

tell one a great about the mode characteristics of the fiber. The V parameter, defined as

$$V = \frac{2\pi a}{\lambda}(n_1^2 - n_2^2)^{1/2} = \frac{2\pi a}{\lambda}\mathrm{NA}, \tag{3.1}$$

where λ is the wavelength of light, determines the number of spatial modes a fiber will guide at a given wavelength. The numerical aperture NA$= (n_1^2 - n_2^2)^{1/2}$ in fibers is similar to the NA in other optical systems and is related to the maximum angle θ_{max} that light can be incident on the core and still be guided by total internal reflection (TIR). In the ray picture θ_{max} is given by

$$\theta_{max} = \mathrm{ArcSin}[\mathrm{NA}], \tag{3.2}$$

although in the more complicated wave picture this is not strictly true.

From an analysis of the boundary conditions of Maxwell's equations for light propagating down a cylindrical waveguide having a core and cladding (as presented in the textbooks referenced above), a step-index fiber having a V value for a given wavelength such that $V < 2.405$ will only guide the fundamental mode. For fibers such that $V < 5.520$ only the first two modes will propagate and for $V < 8.654$ only the first three modes will propagate, etc. Fibers cannot selectively guide some higher modes without guiding all the modes lower than that of the highest mode they guide, i.e. a fiber cannot guide modes 4-6 and not guide 1-3. Hence a fiber that guides at all will always guide the fundamental mode, and the wavelength/V value at which it will guide the second mode is called the "second-mode cut-off". Of course the cut-off concept can be generalized to higher modes and the values for λ and V are found by solving a characteristic equation involving Bessel functions of the first kind and modified Bessel functions of the second kind. A detailed explanation of fiber modes is

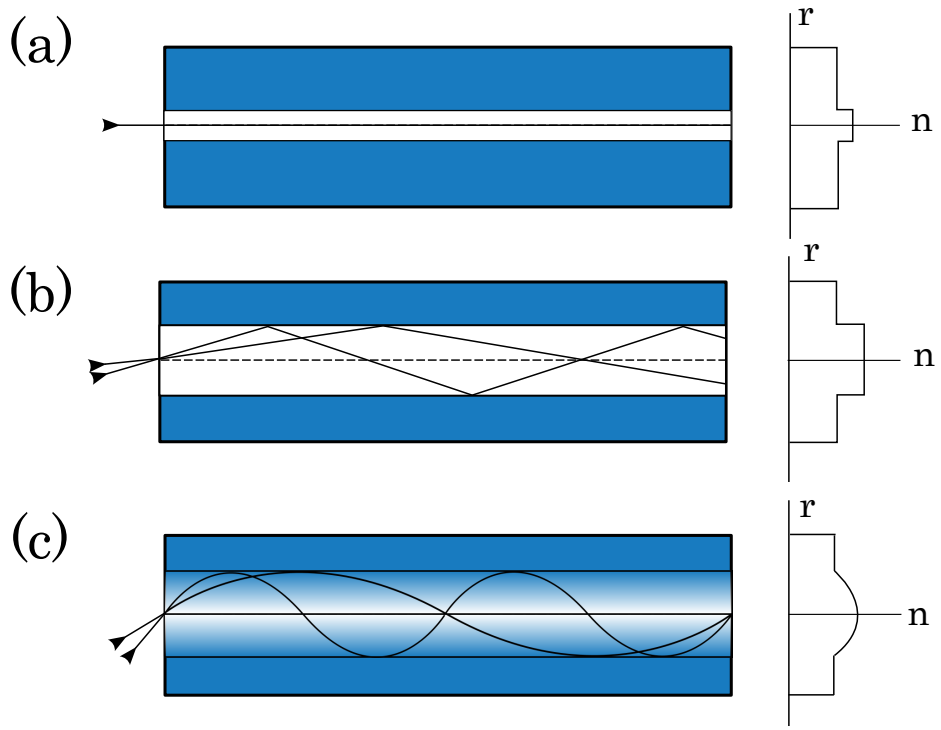

FIGURE 3.1. Schematics of step-index and graded-index optical fibers. (a) A single mode step-index fiber that only propagates the fundamental gaussian down the core. (b) A multi-mode fiber that guides many modes/rays. (c) A graded index fiber, where the time of arrival of the launched pulse is not dependent on its initial angle.

beyond the scope of this dissertation, as the work presented herein deals exclusively with single-mode fibers.

The other type of fiber commonly used is called a graded-index fiber, pictured in Figure 3.1.(c). The index of the core continuously drops off in a radial manner from its peak value on the center of the core, the optical axis, until the cladding is reached. The cladding is uniform having one index n_2. The advantage to this geometry is that a ray that is coupled in at a non-zero angle relative to the optical axis, and initially propagates at some angle to the optical axis, will gradually be directed back towards the optical axis. Once it reaches the axis it will then be propagating at the same initial angle to the axis and be brought slowly back to the axis in the same manner. Although these rays travel a farther distance than rays directed straight down the core they experience a lower average index and therefore travel faster. These fibers are usually designed so that a ray incident at any angle below θ_{max} will take the same amount of time to propagate down the fiber as a ray which is incident at zero angle. Hence spreading that would occur between a pulse coupled in at non-zero angle and one coupled in a zero angle in step-index fiber does not occur in graded-index fibers. These fibers are usually multimode and their analysis is not relevant to fibers used in this dissertation.

3.1.2. Loss, Birefringence, Dispersion and Propagation

One of the most important, if not the most important, parameter in determining which wavelength telecommunications equipment operates at is the attenuation of fused silica as a function of wavelength. This attenuation is usually expressed as the

parameter $\alpha_{dB}(\lambda)$ in units of dB/km defined at a given wavelength by

$$\alpha_{dB} = -\frac{10}{L}\log[P_T/P_0], \tag{3.3}$$

where P_T and P_0 are the output and input powers of the incident beam, respectively. It is related to the more usual definition $P_T = P_0 e^{-\alpha L}$, where α is in units of inverse cm, by $\alpha_{dB} = 4.343\alpha$. The parameter $\alpha_{dB}(\lambda)$ has a minimum in the near-infrared around 1550 nm, which is the most commonly used wavelength in telecommunications. In practice the dominant factor other than pure material attenuation of the overall attenuation is due to Rayleigh scattering, a phenomenon in which light scatters off of, and out of the fiber, due to density fluctuations in the fused silica. The attenuation coefficient for Rayleigh scattering α_R goes as

$$\alpha_R = C_R/\lambda^4 \tag{3.4}$$

where C_R depends on the exact composition of the material and fiber drawing process but is generally in the range of 0.8 dB/(km-μ^4) [60].

Another characteristic of optical fibers is their response to differing polarizations of incident light. Single-mode fibers, while being single mode in their transverse spatial intensity, are not single-mode in terms of polarization. A perfect single-mode fiber will support both orthogonal polarizations of light with no interaction occurring between them. However, real fibers have small defects and deviations that will cause the symmetry of the fiber to be broken, leading to a small amount of birefringence. The indexes of these two birefringent axes n_x and n_y will be slightly different and therefore the light polarized on these axes will encounter differing propagation constants β_x and β_y. This occurrence is called "modal birefringence"

labeled by mode m and is defined as

$$B_m = \frac{|\beta_x - \beta_y|}{k_0} = |n_x - n_y| = \Delta n \tag{3.5}$$

where k_0 is the magnitude of the wavevector of the light in free space [61].[1] Because of this birefringence, a beam completely polarized on one of these axes will undergo an overall change in phase with respect to another field of the same wavelength polarized on the other axis. For long enough fiber length, the phase of this beam will eventually come back into phase with the field on the other axis. The length of fiber that is required for this full-trip oscillation is called the beat length and is given by

$$L_B = \frac{2\pi}{|\beta_x - \beta_y|} = \frac{\lambda}{B_m}. \tag{3.6}$$

The axis in which the propagation constant is higher is called the "slow" axis because light on that axis travels slower than light on the other, "fast" axis.

Due to the random nature of this birefringence, which can change down along the fiber, and the desire to maintain the polarization state of the light as it was when incident on the fiber, so-called polarization maintaining fiber was created in which a large, well-defined birefringence is intentionally introduced that can preserve the linear components of polarization. By aligning the polarization along one of the birefringent axes it is guaranteed that very little light will couple to the other axis and the polarization state will be maintained all along the fiber. There are several method with which to do this, and Figure 3.2.(a) shows two methods; one in which an ecliptically shaped core is created and another in which stress-rods are inserted along

[1] In this dissertation, the propagation constant in free space will be denoted as k, while in material it will be denoted as β.

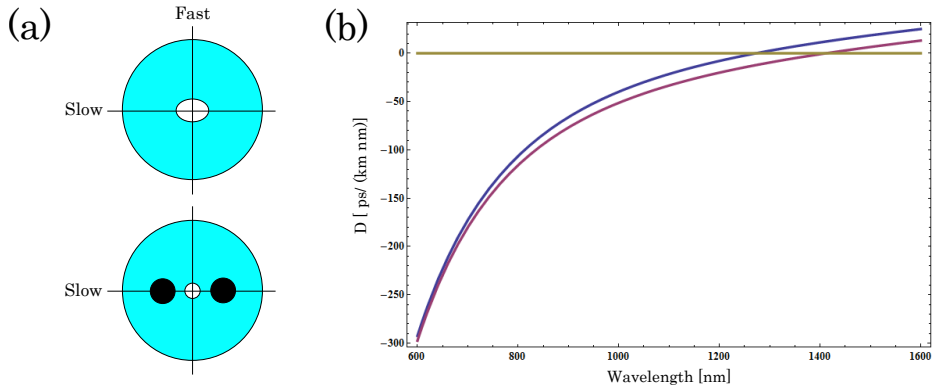

FIGURE 3.2. Polarization maintaining fiber and standard fiber dispersion. (a) Two types of polarization maintaining fibers; elliptical core (top) and panda with stress rods (bottom). The fast and slow axis are label [62]. (b) Fiber D parameter due to only material components (blue) and material plus waveguide components (red). For the waveguiding term a core radius of $a = 2 \cdot 10^{-6}\mu$m and NA $= 0.10$ was used. Although the waveguiding term doesn't change the D parameter much in absolute terms, the ZDW is significantly shifted.

the length of the fiber. Birefringences on the order of $\Delta n \approx 5 \cdot 10^{-4}$ can be created using these methods, while naturally occurring birefringences are several orders of magnitude less.

Above, the propagation constant β was referenced as a property of the mode. A more general description of β would describe it as a property of fiber parameters and input wavelength. In this case it is called the chromatic dispersion, or just dispersion for short, and is one of the most important properties of a fiber overall. It is related to the index of refraction by

$$\beta = \frac{2\pi n}{\lambda} = \frac{n\omega}{c} \tag{3.7}$$

and can be thought of as consisting of three separate terms for single-mode fibers; material, waveguide, and nonlinear:

$$\beta = \beta_M + \beta_W + \beta_{NL}. \tag{3.8}$$

The dispersion is often expressed as a series of terms in a Taylor expansion, written as a function of frequency

$$\beta(\omega) = \beta^{(0)} + \beta^{(1)}(\omega - \omega_0) + \beta^{(2)}(\omega - \omega_0)^2 + \ldots, \tag{3.9}$$

where ω_0 is the frequency expanded around and the $\beta^{(n)}$ derivatives of β are evaluated at ω_0. The first two derivative orders of the dispersion have clear physical meaning. The first order is equal to the inverse of the group velocity, the velocity at which a wavepacket of light moves down the fiber core. The second order, also called the group velocity dispersion (GVD) parameter, indicates the amount of spreading of the individual frequency component in a broad-band pulse that will occur while the pulse travels down the core. It is related to the so-called "D" parameter by the following relation,

$$D = \frac{d\beta^{(1)}}{d\lambda} = -\frac{2\pi c}{\lambda^2}\beta^{(2)}, \tag{3.10}$$

which is often expressed in units of ps/(km $\cdot$ nm). For fused silica D has magnitude of order 10^1 as opposed to $\beta^{(2)}$ that has magnitude on the order of $10^{(-24)}$. The D parameter, or $\beta^{(2)}$, is often the parameter fiber engineers discuss because it is the lowest order term that is relatively straight forward to manipulate through geometric design of the fiber. The ability to manipulate D is particularly important to the present work because, as will be shown in the next chapter, the wavelengths at which D is equal to zero (zero-dispersion wavelengths, ZDWs) are the wavelengths that many of the nonlinear interactions are centered around.

The waveguiding portion of the dispersion is due to the geometric factors, namely core radius a, and fiber index contrast Δ. In term of D the waveguiding term is [58]

$$D_W = -\frac{\Delta}{c\lambda} V \frac{d^2(V \cdot b)}{dV^2} \tag{3.11}$$

where b is a normalized value of β varying from 0 to 1. For general parameter values the second derivative term is difficult to evaluate, but luckily there is an accurate approximation for that term that only depends on the V parameter [59]

$$D_W \cong -\frac{\Delta}{c\lambda} \left(0.08 + 0.549(2.834 - V)^2\right). \tag{3.12}$$

Here the importance of the geometry is quite clear; since V depends linearly on the core radius the D parameter has a strong quadratic dependence on core radius. For small core fiber, such as those used in the presented work, this term becomes significant.

The material component of the dispersion is simply due to the electronic response of molecules in the material to the applied field and therefore is only a function of the molecular structure of the fiber and how exactly they coalesce [63]. Although too complicated to derive presently, the material dispersion of many materials can be accurately approximated by the Sellmeier equations [60]. It is generally the most dominate term in standard fibers; a plot of D_M (the material component to the D parameter) and $D_M + D_W$ for a typical single-mode fiber is shown in Figure 3.2..

The nonlinear contribution to the dispersion is not intrinsic to the fiber, depending on the incident intensity and material composition. It is generally true that $\beta_{NL} = \gamma P$, where

$$\gamma = \frac{n_{NL}\omega}{cA_{eff}}. \tag{3.13}$$

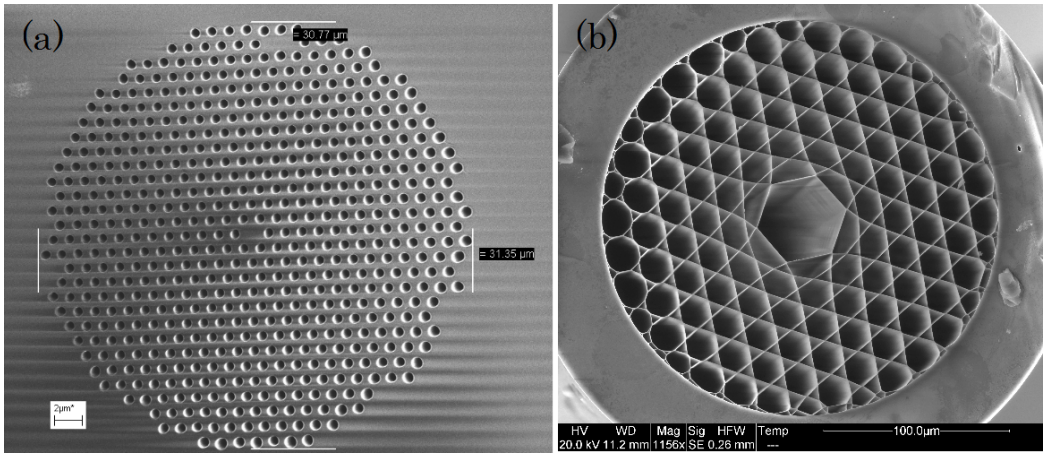

FIGURE 3.3. Photonic crystal fiber: solid and air cores. (a) Scanning Electron Microscope image of a solid-core and (b) hollow-core PCF.

Here n_{NL} is the nonlinear index and A_{eff} is the effective area, usually equal to approximately πa^2. Since we will be dealing with relatively low powers in the experiment we will not need to consider the nonlinear dispersion.

3.2. Photonic Crystal Fibers

In 1996 a novel kind of optical fiber called a photonic crystal fiber (PCF) was fabricated [64]. In contrast to standard fibers, PCFs consist of fiber-sized rod made of a single material where a periodic series of empty holes permeate the length of the rod. This "holey" structure is analogous to the cladding of a standard step-index fiber. The core either consists of an "anti-hole," where there is a material-filled hole or holes near the middle of the cladding, or of a larger air hole. Examples of these two types of PCF are shown in Figure 3.3.. This unique geometry often imbues PCFs with some remarkable properties: "endlessly" single-mode behavior where the fiber only propagates the fundamental mode for a very large range of wavelengths, birefringence an order of magnitude higher than standard PM fibers, and unprecedented control over the fiber dispersion, to name a few.

The fiber gets its name through an analogy to the propagation of electrons through a regular period molecular structure. For certain electron energies, or wavevectors, the electron is allowed to propagate through the material, but for the others energies it is not. Other than molecular composition, the main factor in determining which electron energies allow electron propagation is the periodic nature of the structure, its geometry and de Broglie wavelength. This same effect appears in light transmitting structures that have periodic changes in their indexes of refraction; depending on the index change and geometry only electromagnetic waves (this being a classical phenomenon) with certain energies can propagate through the structure. These structures are called "photonic crystals" and are readily found in nature in butterfly wings, peacock feathers, and opal, among other examples. It is through the creation of these "stop band" ranges in wavelength that is one of the two primary methods of light guidance for PCFs. In the cladding region, where the index periodically varies, only some wavelengths can propagate. Therefore the only direction light having these wavelengths can propagate is down the core where these periodic variations aren't present. This is most often how hollow-core PCFs guide light, and they require precise execution of turning design into reality in order for this effect to occur.

The other way in which PCFs can guide light is through a modified total-internal reflection effect, much like how a standard step-index fiber guides light. In this model the cladding acts as a uniform medium that has an index that is an average of the index of fused silica and air (or of whatever medium is filling the air holes) while the core has the index of fused silica. Then in general the core will a have a significantly larger index than the cladding and will be able to strongly guide light over many wavelengths. A schemata of a typical solid-core PCF is shown in Figure 3.4.(a)

having an air-hole diameter d, distance between air holes (pitch) Λ, and core radius a. Then just like a step-index fiber can be thought of as using the TIR effect to guide, a PCF uses this modified TIR effect to guide. But the analogy isn't perfect; PCFs can exhibit the "endlessly single-mode" effect, where theoretically the V parameter of step-index fibers can become independent of wavelength, and therefore guide only the fundamental mode for all wavelengths [25]. In practice this does not occur, but PCFs are found be single mode over a very broad range of wavelengths, often from the deep visible through the near-infrared. Although the effect is difficult to explain, a qualitative picture put forth in [65] helps in understanding. The array of air holes can be viewed as a "sieve" that light propagating down the core must get through if it is to escape from the core region. For "large" modes, such as the fundamental, it is difficult/impossible for the light to squeeze between the air holes and escape. Higher-order modes are in some sense made up of smaller, more discrete areas of intensity, which can more easily slip through the air holes and escape from the core. Numerical studies have found that for an air-hole diameter to pitch ration $d/\Lambda \leq 0.4$ PCFs become essentially endlessly single mode for all wavelengths [66]. Work in this dissertation has exclusively used solid-core PCFs operating in the modified TIR mode, and all further discussion of PCFs will refer to solid-core PCFS.

For all the advantages PCF offer, one property in particular stands out in its importance to the current work: the ability to significantly alter the dispersion properties of the fiber through design of the hole diameter and pitch. The effect on dispersion is most easily seen in the change in the D parameter, particularly in the ZWDs. Figure 3.4.(b) shows a plot of the D parameter versus wavelength for a typical single-mode fiber and a typical PCF fiber. Whereas the standard fiber only has a ZDW around 1300 nm, the PCF has two ZDW; one around 1300 nm and another

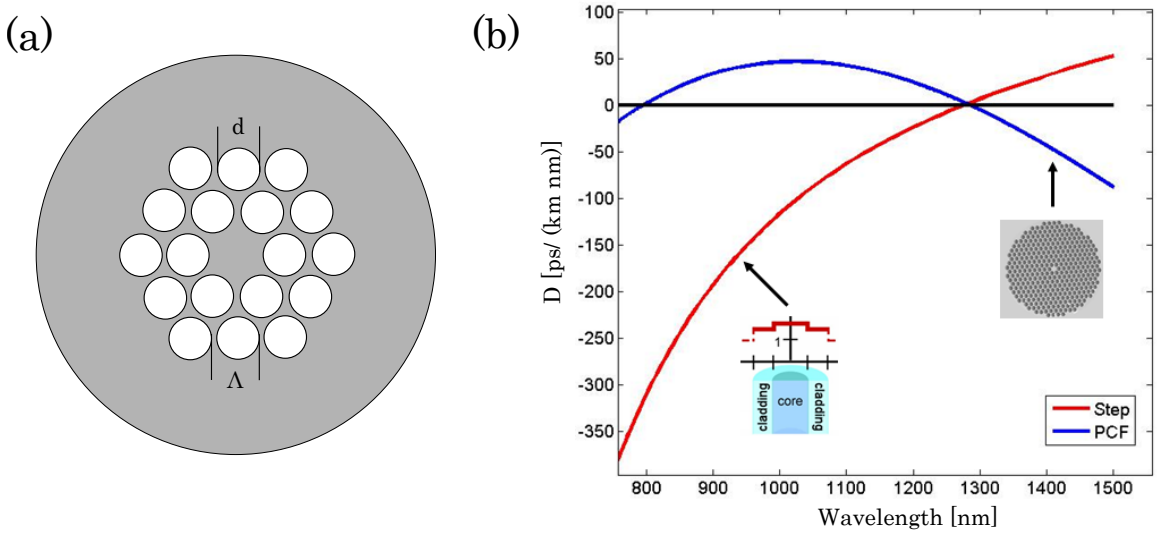

FIGURE 3.4. (a)A schemata of a typical solid-core PCF having air-hole diameter d, pitch Λ, and core radius a.(b) The D parameter for a typical single-mode step-index fiber and for a typical solid-core PCF.

around 800 nm. As mentioned before the ZDW are important in the processes used for creation and translation of light, so this striking difference in ZDW properties is the main reason for the importance of using PCFs over standard fibers in this work.

In order to calculate the dispersion an expression for an effective index of the cladding is required. To good approximation the cladding index as a function of frequency can be approximated as

$$n_{clad}(\omega) = f + (1 - f)n_{core}(\omega), \tag{3.14}$$

where f is the percentage fraction of the cladding that is composed of air, the air-filling fraction, and n_{core} is the index of the core, generally fused silica. This model has been shown to be accurate for a large range of f values, from 0.1 to 0.9 [19]. By modeling the core index through the Sellmeier equations the effective dispersion of the fiber can then be found by by numerically solving the appropriate characteristic

equation involving the solutions of Bessel functions [67]. After the material dispersion, the most important parameters in the computation are the core diameter and air-filling fraction. Since the material is almost always fused silica, taken as given, the core and air-filling fraction become free parameters through which the dispersion characteristics of the fiber can be accurately modeled.

It is interesting to note that there are older models that may or may not be more accurate in particular circumstances, and have the advantage of more easily relating to standard step-index fibers. For example, in [25] a model is put forth where the effective V parameter of the fiber can be found by the expression

$$V_{eff} = \frac{2\pi\Lambda f^{1/2}}{\lambda}(n_{core}^2 - n_{air}^2)^{1/2} \tag{3.15}$$

where it assumed that the medium filling the holes is air. Although an interesting analogy, not all properties of the V parameter carry over exactly. For example, the second-mode cut-off appears to be around 4.1 instead of around 2.405 like in regular step-index fibers [58].

CHAPTER IV

NONLINEAR EFFECTS IN OPTICAL FIBER

Before the invention of the MASER ("Microwave Amplification by Stimulated Emission of Radiation") [68] and LASER ("Light Amplification by Stimulated Emission of Radiation") [69] in 1954 and 1960, respectively, the idea that light could interact with light was not more than exotic (yet intriguing) academic topic without much prospect for experimental investigation.[1] Owing to the large optical powers these coherent source inventions, the field of experimental nonlinear optics began in earnest in 1961 with the first observation of second harmonic generation [71]. Since that time an enormous body of scholarship has been produced concerning the field.

One of the main concerns of the field of fiber optics since its inception has been how to avoid nonlinear effects, which degrade signals and slow down data transfer rates. However, in recent years the potential for nonlinear processes in fibers to be of some benefit has been recognized with the advent of such applications as fiber amplifiers, optical switching, fiber lasers and frequency conversion, to mention just a few. In this chapter a few nonlinear processes important to the work presented in this dissertation will be discussed. First, a theoretical treatment of nonlinear process in fibers will be given, followed by a discussion of phase modulation and Raman scattering. Then the three processes of Four-Wave Mixing (FWM), used for photon creation and photon frequency translation, are discussed. Of course this short

[1]The paper that first documented observation of a laser in action by T.H. Maiman was rejected by *Phys. Rev. Lett.*, only later to be published in *Nature*. As related by Charles Townes, the leader of the research group that invented the MASER, in [70], "Simon Pasternack, who was an editor of Physical Review Letters at the time, has said that he turned down this historic paper because Maiman had just published, in June 1960, an article on the excitation of ruby with light, with an examination of the relaxation times between quantum states, and that the new work seemed to be simply more of the same."

discussion barely scratches the surface of nonlinear fiber optics; the interested reader is pointed to [60] and [72] for far more complete discussions of the topic. Lastly, the two-color Hong-Ou-Mandel interference effect is discussed and probabilities associated with it are calculated.

4.1. The Nonlinear Wave Equation

We begin our study by re-examining the free space traveling wave equation for the electric field derived in chapter two:

$$\nabla^2 \mathbf{E_f} - \frac{1}{c^2}\partial_t^2 \mathbf{E_f} = 0, \tag{4.1}$$

where the speed of light in vacuum is $c = (\mu_0 \epsilon_0)^{-1/2}$ and $\mathbf{E_f}$ denotes that this the field in free space. This was derived with the assumption that there was no medium other than empty space through which we were traveling. Now consider an electromagnetic wave traveling in a non-magnetic, dielectric medium that has bound charge ρ_b (and no free charge by definition) that obeys the relation to the electric polarization $\rho_b = -\nabla \cdot \mathbf{P}$. Two of the four Maxwell's equations must change, and they are now

$$\nabla \cdot \mathbf{D} = 0 \tag{4.2}$$

$$\nabla \cdot \mathbf{B} = 0 \tag{4.3}$$

$$\nabla \times \mathbf{E} = -\partial_t \mathbf{B} \tag{4.4}$$

$$\nabla \times \mathbf{H} = \partial_t \mathbf{D}, \tag{4.5}$$

where $\mathbf{D} = \epsilon_0 \mathbf{E} + \mathbf{P}$ and $\mathbf{B} = \mu_0 \mathbf{H}$. This has the effect of adding an extra term to the wave equation so that

$$\nabla^2\mathbf{E} - \frac{1}{c^2}\partial_t^2\mathbf{E} = \mu_0\partial_t^2\mathbf{P}. \tag{4.6}$$

To clarify this further, we break up the electric polarization into linear and nonlinear parts

$$\mathbf{P} = \mathbf{P}^{(1)} + \mathbf{P}^{\mathrm{NL}}. \tag{4.7}$$

In the time domain, this is the most we can simplify the wave equation and have it be applicable to most situations (remember the slowly varying wave approximation was made). The problem is that while $\mathbf{P}$ and $\mathbf{E}$ are related, their relation is non trivial in the time domain, as can be seen from the expression for $\mathbf{P}^{(1)}$:

$$\mathbf{P}^{(1)}(\mathbf{r},t) = \epsilon_0\int_{-\infty}^{\infty} dt^{'}\chi^{(1)}(t-t^{'})\cdot\mathbf{E}(\mathbf{r},t). \tag{4.8}$$

Luckily, to good approximation, this problem is not present in the frequency domain, so that

$$\mathbf{P}^{(1)}(\mathbf{r},\omega) = \epsilon_0\chi^{(1)}(\omega)\cdot\mathbf{E}(\mathbf{r},\omega). \tag{4.9}$$

With this relation, and the knowledge that $\partial_t \rightarrow -i\omega$ in a transformation from time to frequency, the nonlinear wave equation becomes

$$\nabla^2\mathbf{E}(\mathbf{r},\omega) + \epsilon\frac{\omega^2}{c^2}\mathbf{E}(\mathbf{r},\omega) = -\mu_0\omega^2\mathbf{P}^{\mathrm{NL}}(\mathbf{r},\omega), \tag{4.10}$$

where $\epsilon = \epsilon_0(1+\chi^{(1)})$.

Now the question arises what exactly is the form of the nonlinear polarization? At the most basic level the polarization response is related to the anharmonic nature

of the potential under which electrons in the medium are bound under the influence of an incident field [60]. Therefore the general relation between $\mathbf{P}$ and $\mathbf{E}$ in frequency, with suppressed parameters, is

$$\mathbf{P} = \mathbf{P}^{(1)} + \mathbf{P}^{(2)} + \mathbf{P}^{(3)} + \cdots = \epsilon_0 \left(\chi^{(1)} : \mathbf{E} + \chi^{(2)} : \mathbf{EE} + \chi^{(3)} : \mathbf{EEE} + \dots \right), \quad (4.11)$$

where $\chi^{(j)}$ is the j^{th} order susceptibility, and is in general is a tensor of rank $j+1$. While every material has a non-zero value for $\chi^{(1)}$, the higher order terms often depend on the geometry of the molecular substance to determine whether they are non-zero or not. In the case of fused silica, or SiO_2, which lacks the property of inversion symmetry, $\chi^{(2)}$ and all even terms are essentially zero [60]. Therefore the highest nonlinear term of meaningful magnitude that is present in optical fiber is the third order term. Although just one term, an amazing number of interesting phenomenon occur because of it of which we will only mention a few.

4.2. Phase Modulation and Raman Scattering

Although there is only one meaningful nonlinear term in (4.11) for fibers, for even a monochromatic input fields that term implies several effects such as harmonic generation, four-wave mixing and a nonlinear refractive index. The first two effects create fields at new frequencies, but unless material parameters are just right these effects will be very inefficient and should only be considered under special circumstances where care is taken to allow them to occur on a meaningful scale. The remaining effect, a nonlinear refractive index, occurs whenever there is a field $\mathbf{E}$ applied to a third-order medium. In that case the electric polarization can be written

as

$$\mathbf{P} = \epsilon_0 \left(\chi^{(1)} : \mathbf{E} + \chi^{(3)} : \mathbf{EEE}\right) = \epsilon_0 \left(\chi^{(1)} + 3\chi^{(3)}|E|^2\right) \cdot \mathbf{E}, \tag{4.12}$$

where the $\chi^{(3)}$ tensor can be reduced to a scalar due to the symmetry of fused silica. The factor of 3 comes from three possible ways in which can be attained in (4.11). The refractive index can be written as

$$n = \left(\frac{\epsilon}{\epsilon_0}\right)^{1/2} = (1 + \chi^{(1)} + 3\mathrm{Re}[\chi^{(3)}]|E|^2)^{1/2}. \tag{4.13}$$

Since $\mathrm{Re}[\chi^{(3)}]|E|^2$ is significantly smaller than $\chi^{(1)}$ in any normal circumstance, this can be accurately approximated as

$$n \approx n_0 + \frac{3\mathrm{Re}[\chi^{(3)}]|E|^2}{n_0 2} = n_0 + n_2 I \tag{4.14}$$

where n_0 is the linear index of refraction and n_2 is the nonlinear refractive index. Here $I = 2\eta P/A_{eff}$ is the intensity, P is the peak power, A_{eff} is the effective cross-sectional area of the fiber, and $\eta = (\mu_0/\epsilon_0)^{1/2}$. This leads to two interesting phenomena among others[2], self-phase modulation and cross-phase modulation. For self-phase modulation, note that for a one-dimensional plane wave having traveled distance L the field is proportional to

$$\mathbf{E} \propto e^{ik_0 L} = e^{i\phi[L]} \tag{4.15}$$

with

$$\phi[L] = \frac{2\pi n L}{\lambda} = 2\pi L \frac{n_0 + n_2 I}{\lambda}. \tag{4.16}$$

[2]It is this effect, also called the optical Kerr effect, that is responsible for self-focusing and soliton formation [57].

This implies that the intensity of the field causes its own phase to evolve faster than it usually would, hence the name self-phase modulation. If the incident field contains two or more input frequencies then a cross-phase modulation can occur in which the fields induce a phase modulation on each other. Going through a procedure similar to the above, one finds the cross modulation term to be twice as strong as the self modulation term, hence the total nonlinear phase modulation for a field is

$$\phi_{NL} = 2\pi L \frac{n_2(I_1 + 2\sum_{m\neq 1} I_m)}{\lambda} \tag{4.17}$$

where I_m denotes the intensity from fields other than the field in question.

These modulation effects are useful for the control of light with light. In the present work, which uses relatively weak pulses for a short amount of fiber, these two effects are not significantly present.

The phase-modulation effects are dependent on the real part of the third-order susceptibility. In general $\chi^{(3)}$ is complex. The imaginary part of $\chi^{(3)}$ comes into the expression for the phase just like the real part did, although since it is accompanied with an i the exponent of (4.15) becomes partially real. Splitting this part off we see

$$\mathbf{E} \propto e^{i \cdot i g_R I L} = e^{-g_R I L} \tag{4.18}$$

where by this definition g_R is the Raman gain coefficient given by [57]

$$g_R = \frac{12\pi \mathrm{Im}[\chi^{(3)}]\eta}{n_0 \lambda}. \tag{4.19}$$

This effect was first seen by Raman and Krishnan in 1928 [73]. More properly, the Raman gain should be written as a function of the frequency difference between ω and

the frequency of the pump producing the Raman scattering light. On a fundamental level photons from the pump field are scattering off the molecules of the material into photons of lower frequency/energy. The energy imparted to the molecule excites the vibrational states of the molecule/medium. The new lower-energy photon is called the Stokes wave. Interestingly, there can also be anti-Stokes waves, where the scattered photon has higher energy than original photon with the extra energy coming from the vibrational state of the medium. Anti-Stokes waves are always much weaker than Stokes waves because the vibronic population in higher states is always less than those of lower states by the Boltzmann factor $e^{-\hbar\Delta\omega/k_BT}$ [72].

The spontaneous Raman effect, which requires a quantum mechanical description, is a fairly weak process that only scatters about 1 in 10^6 incident photons in one cm of material such as glass. But once some Raman radiation is present the stimulated Raman effect described above acts in an exponential manner, and under appropriate conditions nearly all of the incident power can be transferred to the Stokes and Anti-Stokes frequencies. Stimulated Raman scattering was discovered in 1962 [74] and is still a subject of current research. In the present work Raman scattering is theorized to be by far the leading cause of noise pollution. Luckily, the effect was not as strong as creation and translation effects that were engineered to occur. Details on the noise pollution in the presented work is given in Chapter VI.

4.3. Four-Wave Mixing

The above effects were created by considering only one incident frequency component. Of course there could be more, and in practice, since real fields are not purely monochromatic, there always are. When considering the nonlinear polarization response for a field with more than one frequency component in a third-order medium

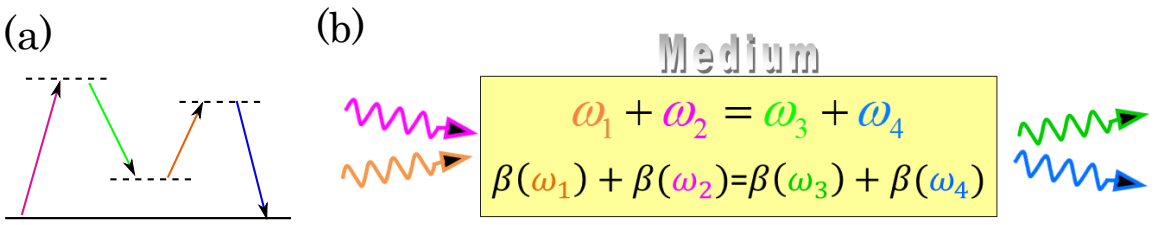

FIGURE 4.1. (a) Schematic of a parametric four-wave mixing process. Dashed lines represent virtual levels. (b) Cartoon of the two-body four-wave mixing process. Energy and momentum must be conserved for efficient product generation. In single-mode fibers the direction of propagation is one-dimensional, down the fiber core.

the phenomena that are produced are said to be products of a four-wave mixing (FWM) process. As noted before, effects of these types are generally not efficient unless special care is taken to ensure that they occur. The FWM processing is a subset of a larger group of processes called parametric processes, where the medium does not absorb or provide any energy to the process, it only "hosts" the process through allowing the interacting particles to excite virtual states.[3] A picture of such a process is shown in Figure 4.1.(a). As a consequence, the final quantum state of the medium is identical to that of the initial state. An easy way to distinguish parametric and non-parametric processes is that only the real part of the susceptibility is involved in parametric process. Hence Raman scattering is not a parametric process, which is also clear since it excites vibrational level of the media's molecules, and hence the final and initial quantum states of the medium are not equal.

To understand the special conditions necessary for FMW consider the situation in which three monochromatic plane-wave fields of differing frequencies are incident

[3]The time interval over which these virtual transitions can take place is roughly given by the pseudo time-energy uncertainty principle, $\Delta t \approx \hbar/\Delta E_n$, where E_n is the energy difference between the occupied virtual level and the nearest real level [72].

on a a third-order medium.

$$\mathbf{E}(\mathbf{r},\omega) = E_1 e^{-i(\beta_1\cdot\mathbf{r}+\omega_1 t)} + E_2 e^{-i(\beta_2\cdot\mathbf{r}+\omega_2 t)} + E_3 e^{-i(\beta_3\cdot\mathbf{r}+\omega_3 t)} + \text{c.c.}, \tag{4.20}$$

with E_i being the amplitude of the *ith* field and c.c. denotes the complex conjugates off the three fields. The nonlinear polarization will then consist of $6^3 = 216$ terms due to its triple-product nature. Of all the possible terms let us examine the one that consists of the positive frequency components of fields one and two, and the conjugate component of three:

$$\mathbf{P}^{(\text{NL})} = E_1 E_2 E_3^* e^{(-i(\beta_1+\beta_2-\beta_3)\cdot\mathbf{r}+i(\omega_1+\omega_2-\omega_3)t)} \tag{4.21}$$

The nonlinear polarization will build up a new field with a frequency ω_4 and wavevector β_4 under the conditions that $\omega_4 = \omega_1+\omega_2-\omega_3$ *and* $\beta_4 = \beta_1+\beta_2-\beta_3$. In the quantum-mechanical picture, positive frequency components of the field correspond to annihilation operators and negative frequency components correspond to creation operators. Hence in a simplified quantum-mechanical picture, depicted in Figure 4.1.(b), this FWM process can be thought of as photon one and two being annihilated by the medium and two new photons 3 and 4 being created by the medium. Since energy and momentum must be conserved, disregarding nonlinear dispersion, we have

$$\boxed{\omega_1 + \omega_2 = \omega_3 + \omega_4} \tag{4.22}$$

and

$$\boxed{\beta_1 + \beta_2 = \beta_3 + \beta_4} \tag{4.23}$$

for optimal conversion. In a field-theoretic approach this interaction would be called two-body scattering. It is clear now why these interactions do not always take place in a third-order medium. Not only must the energies of the products and reactants be equal, but the sums of the momentums must also equal. If they momentums of products and reactants do add up then the process is said to be phase-matched. Unless engineered to do so it is unlikely that these two conditions will occur in any given medium. That being said, it is readily possible in PCF to engineering FWM over a large range of frequencies. This interaction serves as the basis for the photon creation and translation effects presented in this dissertation.

4.3.1. Modulation Instability and Phase Conjugation: Photon Creation

In $\chi^{(3)}$ media the FWM processes responsible for photon creation are called modulation instability and phase conjugation. These two processes are in some sense quite similar to the parametric photon creation process in $\chi^{(2)}$ media, called spontaneous parametric down conversion (SPDC). The SPDC process was first realized in 1967, and was a relatively straight forward technique to produce photons compared to the atomic cascade sources it replaced [8]. It utilizes the second-order nonlinear properties of the medium to split a pump beam photon with frequency ω_p into two photons having frequencies ω_s and ω_i. These created photons can have equal or differing central frequencies and are traditionally called the "signal" (lower-wavelength) and "idler" (higher-wavelength). The exact value of ω_s and ω_i depends on the pump wavelength, polarization, and medium dispersion properties. SPDC in nonlinear crystals as a photon source has been the work horse of quantum optics for several decades. However, the ability to control the quantum state of the photon

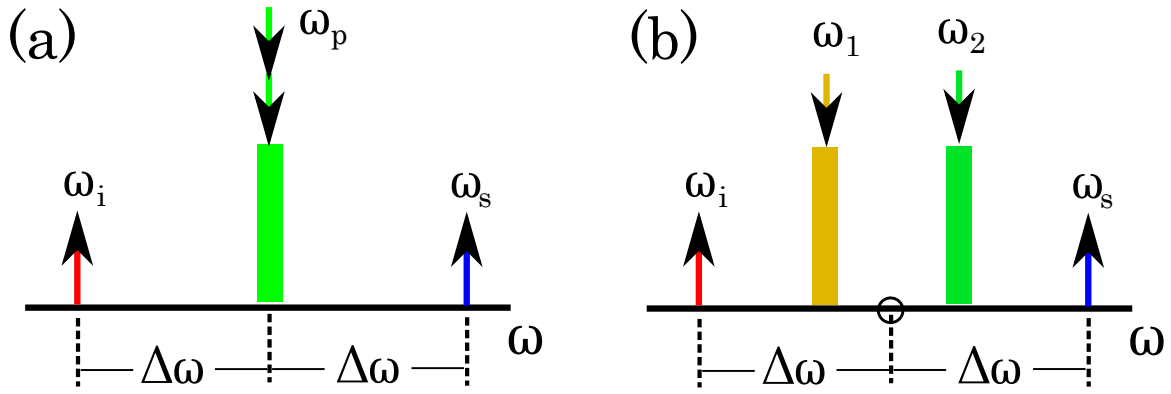

FIGURE 4.2. Modulation instability and phase conjugation. (a) A diagram of the modulation instability process where two pump photons are annihilated (down arrows) and two sideband signal and idler photons are created (up arrows). The magnitude of the frequency difference between pump and either sideband, $|\Delta\omega|$, is the same. (b) A diagram of the phase conjugation process where two photons from pumps one and two are annihilated and two sideband photons are created. The circle represents the average frequency of both the pumps and sidebands. Again, $|\Delta\omega|$, is the same, this time in regards to the average frequency.

pairs produced in SPDC is limited by the natural dispersion of second-order nonlinear materials and the pump geometry.

With the advent of optical fiber a new method for generating photons became available that enables more control over the nature of the photon states created than is generally possible with SPDC in nonlinear crystals. In 2002 the first verifiable single photon source in fiber due to $\chi^{(3)}$ nonlinearity was demonstrated [13]. It used the Spontaneous FWM (SFWM) process of modulation instability (MI) where a strong pump field is coupled into the fiber and two pump photons at frequency ω_p are annihilated and two sideband photons, known as the signal (s) and idler (i), are created at frequencies ω_s and ω_i, where $2\,\omega_p = \omega_s + \omega_i$. Along with this energy conserving relation, momentum must also be preserved, so the process must be phased-matched to achieve good efficiency. The process is shown in Figure 4.2.(a). Historically the name modulation instability came from the general phenomenon of

a system that experiences an instability that leads to a modulation of the steady state as a result of the interaction between nonlinear and dispersive properties of the system. In the case of an optical field in a fiber, MI requires the pump to be in a region of anomalous dispersion (where the D parameter is positive) to balance out the nonlinear dispersive term, eventually leading to the creation of sideband fields [60].

A very similar effect, called phase conjugation (PC), can also create sideband pairs, and is essentially a generalization of MI. In PC, two photons, each coming from one of two strong pumps with frequencies ω_1 and ω_2, are annihilated and two new photons ω_s and ω_i are created such that $\omega_1 + \omega_2 = \omega_s + \omega_i$. The process is shown in Figure 4.2.(b). Its name comes from the fact that the idler and signal terms in the classical theory are coupled to the conjugate of one another. To see this, and arrive at simplified but approximately accurate macroscopic solutions, we turn to the classical theory of two-body FWM processes. To get the full picture we will then turn to the quantum theory.

Let $E(t, z)$ be the linearly polarized electric field of a light wave traveling along the positive z axis in a fiber (the transverse x and y components can be ignored for our purposes) [75]. It is common to measure frequencies relative to a carrier frequency and associated propagation constant, Ω_0 and β_0 respectively. The field can then be written as

$$E(t, z) = A(t, z)\exp[i(\beta_0 z - \Omega_0 t)] + \text{c.c.}. \tag{4.24}$$

The wave amplitude $A(t, z)$ satisfies the Nonlinear Schrödinger equation [60], given by

$$\partial_z A(t, z) = i\beta(i\partial_t; \Omega_0)A(t, z) + i\gamma|A(t, z)|^2 A(t, z). \tag{4.25}$$

The first term on the right side accounts for dispersive effects on the field due to the fiber. This is essentially the Fourier transform of $\beta(\omega)$ so that dispersion effects can be included in the time domain. It can be written as the Taylor expansion about a central frequency of the fiber dispersion, which can be written in less compact (but more intelligible) form as

$$\beta(i\partial_t;\Omega_0) = \sum_{n=1}^{\infty} \frac{\beta^{(n)}(\Omega_0)(i\partial_t)^n}{n!}. \tag{4.26}$$

The second right hand term of (4.25) accounts for all the nonlinear effects discussed earlier in the chapter. The nonlinear coefficient γ is defined as $\gamma = n_2\omega/(cA_{eff})$, where A_{eff} is the effective area of the fiber core (essentially the cross sectional area of the core) and n_2 is the nonlinear index of refraction of the fiber. Often is the case that γ varies weakly with frequency, and is usually approximated as a constant.

Equation (4.25) can be modified so that the time variable of the field refers to the time in the frame of reference of the field, the so-called retarded frame, by making the substitution

$$T = t - z/v_g = t - \beta_1 z. \tag{4.27}$$

Here v_g is the group velocity of the field at frequency Ω_0. This substitution then remakes (4.25) and (4.26) into

$$\partial_z A(T,z) = \beta_T(i\partial_T;\Omega_0)A(T,z) + i\gamma|A(T,z)|^2A(T,z) \tag{4.28}$$

$$\beta_T(i\partial_T;\Omega_0) = \sum_{n=2}^{\infty} \frac{\beta^{(n)}(\Omega_0)(i\partial_T)^n}{n!}. \tag{4.29}$$

The only difference other than notation of the corresponding equations is that (4.29) begins the sum at $n = 2$ instead of $n = 1$. Although it is not necessary to make this

substitution, and we will not use it in the rest of the chapter, it becomes necessary when solving the above equations numerically.

If it is assumed that the field is composed of two CW pump fields (or fields that can accurately be approximated as CW fields, so-called quasi-CW fields) with powers P_1 and P_2, centered around frequencies Ω_1 and Ω_2 respectively, then the solution to (4.25) is given by

$$A(t,z) = P_1^{1/2}\exp[i(\phi_1(z) - \Omega_{p1}t)] + P_2^{1/2}\exp[i(\phi_2(z) - \Omega_{p2}t)] \tag{4.30}$$

where $\phi_{1(2)} = \beta(\Omega_{1(2)})z + \gamma(P_{1(2)} + 2P_{2(1)})$ is the wavenumber shift of each field to do the effects of dispersion and self/cross phase modulation.

Now in addition to the pump fields let us add two fields having much weaker field strengths than the pumps, the signal and idler fields having central frequencies Ω_s and Ω_i respectively. These weak fields will not meaningfully affect the evolution of the pump fields, so we can keep our former solution. As the fields propagate down the fiber they will interact, and one of these interaction will be MI that only is dependent on one pump that has a power that will simply be labeled as P (no subscript).

To see how this manifests quantitatively we make the ansatz that the signal and idler fields take the form

$$A_s(t,z) = B_s(z)\exp[i(\phi_1(z) - \Omega_s t)] \tag{4.31}$$

$$A_i(t,z) = B_i(z)\exp[i(\phi_2(z) - \Omega_i t)]. \tag{4.32}$$

Notice the B amplitudes are only a functions of z, not t and z. Adding these fields to the pump field, plugging the resulting field into (4.25), collecting terms of like frequency, discarding terms with small contributions and solving for the signal and

idler amplitudes yields the coupled equations

$$d_z B_i^* = -i(\beta_i - \beta_p + \gamma P)B_i^* - i\gamma P B_s \tag{4.33}$$

$$d_z B_s = -i(\beta_s - \beta_p + \gamma P)B_s + i\gamma P B_i^*. \tag{4.34}$$

By solving these equations, the manner in which power is transferred from the pump to the idler and signal mode can be seen. For simplicity, let us assume that the normalized power of the idler and signal fields (proportional to $|B_{i(s)}|^2$) is given at the input of the fiber by $P_s(0) = 0$ and $P_i(0) = 1$. This zero and non-zero assignment of powers is arbitrary and could be reversed to get the correspondingly similar effect. The powers as a function of z are

$$P_i(z) = 1 + (\gamma P/\kappa_{MI})^2 \sin^2(\kappa_{MI} z) \tag{4.35}$$

$$P_s(z) = (\gamma P/\kappa_{MI})^2 \sin^2(\kappa_{MI} z) \tag{4.36}$$

where $\kappa_{MI} = (\Delta\beta_{MI})^2 - (\gamma P)^2)^{1/2}$. The quantity $\Delta\beta_{MI}$ is the combination of the material and waveguiding dispersive mismatch from (3.8), and is given by

$$\Delta\beta_{MI} = (\beta(\Omega_i) + \beta(\Omega_s) - 2\beta(\Omega_p) + 2\gamma P)/2. \tag{4.37}$$

Similarly, for PC, the governing equation that includes both pumps is[4]

$$d_z B_i^* = -i(\beta_i - \beta_1 + \gamma P_1)B_i^* - i2\gamma(P_1 P_2)^{1/2} B_s \tag{4.38}$$

$$d_z B_s = -i(\beta_s - \beta_1 + \gamma P_2)B_s + i2\gamma(P_1 P_2)^{1/2} B_i^*. \tag{4.39}$$

[4]These equations appear asymmetric with respect P_1 and P_2. Further simplification shows they are not. See [75] for details.

Solving these equations with the condition $P_s(0) = 0$ and $P_i(0) = 1$ yields

$$P_i(z) = 1 + (4\gamma P_1 P_2/\kappa_{PC}^2)\sin^2(\kappa_{PC} z) \tag{4.40}$$

$$P_s(z) = (4\gamma P_1 P_2/\kappa_{PC}^2)\sin^2(\kappa_{PC} z), \tag{4.41}$$

where $\kappa_{PC} = (\Delta\beta_{PC})^2 - 4\gamma^2 P_1 P_2)^{1/2}$. The quantity $\Delta\beta_{PC}$ is the combination of the material, waveguiding and nonlinear dispersive mismatch from (3.8), and is given by $\Delta\beta_{PC} = (\beta(\Omega_i) + \beta(\Omega_s) - (\beta(\Omega_1) + \beta(\Omega_2)) + \gamma(P_1 + P_2))/2$.

Although this model cannot by definition give insight into the quantum mechanical aspects of light produced by MI and PC, it serves as a useful classical model except for one glaring problem. For there to be any amplification of the signal and idler modes there needed to be some non-zero amplitude in either the signal and/or idler modes at the very beginning of the fiber. Hence this theory cannot account for the situation where only the pump fields are incident upon the fiber. In effect what this theory can model is *Stimulated* FWM, where further growth of the sidebands is stimulated by sideband modes that are already present. What we require is a theory that can account for *Spontaneous* FWM, for which we will have to turn to the quantum theory of FWM. In practice, if one is only interested in the powers of the sidebands, the quantum theory is used to find the initial "seed" sideband light after which the above classical theory is adequate in describing the evolution of the sidebands.

Since we are exploring the regime where only a small amount of light is produced, we will be able to use perturbation theory [46]. Our first step then is to discover a Hamiltonian that accurately describes our system, and we will first study the one-pump MI process. For spontaneous FWM by one pump the relevant interaction

Hamiltonian is given by [76]

$$\mathcal{H}(t) = \epsilon_0 \chi^{(3)} \int_V dV E_s^- E_i^- E_1^+ E_2^+, \tag{4.42}$$

where $E^{+,-}$ are the positive and negative frequency components of the respective pump and sideband fields. We treat the sideband fields as quantum objects, leading to the relation [38, 77]

$$E_{s,i}^- = \sqrt{\frac{\hbar\omega_{s,i}}{2\epsilon_0 V}} \frac{\hat{a}_{s,i}^\dagger}{n(\omega_{s,i})} e^{i(\beta_{s,i}z - \omega_{s,i}t)} \tag{4.43}$$

as stated in (2.8) and (2.21), except for a factor of $n(\omega)$ is included due to the sidebands being in the fiber (the central propagation constant and frequency are factored out). Since the pumps contain a macroscopic number of photons it is appropriate to treat them as classical objects expressed as

$$E_{1,2}^+ = e^{-i\Omega_{1,2}t} \int d\omega A(\omega) e^{i(\beta_{1,}z - \omega t)}, \tag{4.44}$$

which is similar to (4.24) except that the time component has been Fourier transformed into the frequency component. As for most pulsed pumps, the frequency amplitude function $A(\omega)$ can accurately be approximated as a Gaussian, so

$$E_{1,2}^+ \cong e^{-i\Omega_{1,2}t} e^{-i\gamma P z} \sqrt{\frac{2\pi P}{\sigma_p}} \int d\omega e^{-\frac{(\omega-\Omega_{1,2})^2}{2\sigma_p^2}} e^{i(\beta_{1,2}z - \omega t)}, \tag{4.45}$$

where σ_p is the spectral width of the pulse and the term γP comes from the self-phase modulation effect.

Plugging these expressions in we now have an expression for the effective Hamiltonian. Formally, the state is found by acting the evolution propagator on the initial state. Since we are treating the pumps as classical objects the initial state is simply the vacuum for the sidebands, hence $|\psi\rangle = \mathrm{Exp}[\int_t dt\mathcal{H}(t)/i\hbar]|0\rangle$, which is a complicated state in general. If we make the assumption that the input pump is "weak" then we can accurately approximate the state with first-order perturbation theory. After performing this and putting the expression into a simplified form we see

$$|\psi\rangle \cong \left(1 + \int_t dt\mathcal{H}(t)/i\hbar\right)|0\rangle = |0\rangle + C\int\int d\omega_s\omega_i F(\omega_s,\omega_i)|1_s\rangle|1_i\rangle \tag{4.46}$$

where all the constants are condensed into the constant C, including the pump power and fiber nonlinearity. The notation $|1_s, i\rangle$ refers to a single-photon state in the signal/idler mode. To first order it describes the creation of a state that is mostly vacuum but has a small probability to contain a photon-pair, the signal and idler. The variables ω_i and ω_s extend over all frequencies, although the expression will only have significant amplitude for the frequencies the signal and idler are centered around. The meaning of a weak pump is now clear; if the pump power and fiber nonlinearity are such that the constant $C \ll 1$ then the first-order term in the expansion is significantly less than the zeroth order term and the approximately is warranted. For a given pump wavelength the function F is a normalized function and only a function of the variables ω_i and ω_s. It is called the joint-spectrum amplitude (JSA) and its modulus squared is the spectral probability density of the state, that is, $|F(\omega_s,\omega_i)|^2$ is the probability that the signal and idler photons will be in the frequency interval $d\omega$ at frequency ω_s and ω_i respectively.

Most generally the JSA can be expressed as an integral equation [15]

$$F(\omega_s,\omega_i) = \int d\omega^{'}\alpha_1(\omega^{'})\alpha_2(\omega_s+\omega_i-\omega^{'})\cdot\text{sinc}\left[\frac{L}{2}\Delta\beta(\omega_s,\omega_i,\omega^{'})\right]\exp\left[\frac{iL}{2}\Delta\beta(\omega_s,\omega_i,\omega^{'})\right] \tag{4.47}$$

where the functions α are related to the pump photon's fields and pump amplitude spectrum, and $\Delta\beta$ is the dispersion mismatch for all material, waveguide and nonlinear dispersion related to (4.37) and given by

$$\Delta\beta(\omega_s,\omega_i,\omega^{'}) = \beta(\omega^{'}) + \beta(\omega_s+\omega_i-\omega^{'}) - \beta(\omega_s) - \beta(\omega_i) + 2\gamma P. \tag{4.48}$$

In general, for an arbitrary dispersion profile and pump-amplitude spectrum, this expression can be quite complex. But having made the excellent Gaussian spectrum approximation for the pump and further making the assumption that the dispersion mismatch can be well approximated by a linear Taylor expansion in the sideband frequencies we will be able to drastically simplify the above expression [15]. The linear mismatch is given by

$$\Delta\beta_{lin} = \Delta\beta^{(0)} + (\beta_p^{(1)} - \beta_s^{(1)})(\omega_s - \Omega_s) + (\beta_p^{(1)} - \beta_i^{(1)})(\omega_i - \Omega_i), \tag{4.49}$$

where $\Delta\beta^{(0)}$ is the zeroth-order Taylor term in the mismatch expansion. This linear approximation is warranted when the widths of the sideband spectral states are significantly smaller than the frequency interval required to meaningfully change the GVD of the fiber, which is often on the order of tens of Terahertz. In [14–16], the approximation was made where the sideband states had pulse durations as short as several hundred femtoseconds. In the work presented here the pulse widths will

have durations on the order of 100 ps, and therefore much spectrally shorter than is necessary for the approximation to be accurate.

With these approximations it can be shown that the JSA expression reduces to a simple product of two functions

$$F(\omega_s, \omega_i)_{lin} = (\alpha(\omega_s, \omega_i)) \cdot \left(\text{sinc} \left[\frac{L\Delta\beta_{lin}}{2} \right] \exp \left[\frac{iL\Delta\beta_{lin}}{2} \right] \right). \tag{4.50}$$

The first function in parentheses is called the pump envelope function and is simply a Gaussian function given by

$$\alpha(\omega_s, \omega_i) = \exp[-\frac{((\omega_s + \omega_i) - (\Omega_s + \Omega_i))^2}{2\sigma_p^2}]. \tag{4.51}$$

This function is dependent only on one parameter, the pump spectral width, and does not change from fiber to fiber. The second function, in the second set of parentheses, broken up into two functions with identical arguments, describes the diserpsion/phase-matching properties of the fiber. It is dependent on fiber characteristics and will completely change from fiber to fiber. A similar but more complex derivation for the PC process can be found in [15].

Since the most interesting and complex part of the JSA is the function involving the sinc function let us explore it in more depth. Pictured in Figure 4.3.(a) is a contour of the sinc function (in this as for most cases the phase constant is irrelevant) at its maximum, where its argument is zero. The modeled dispersion is of a PCF fiber used in the experiment with an incident field that is linearly polarized on one of the birefringent axes. This is using the full expression for the $\Delta\beta$, (4.48), not the linear approximation. On the horizontal axis is the pump wavelength and on the vertical axis is $\Delta\omega$, which is the frequency difference between the pump and the signal or

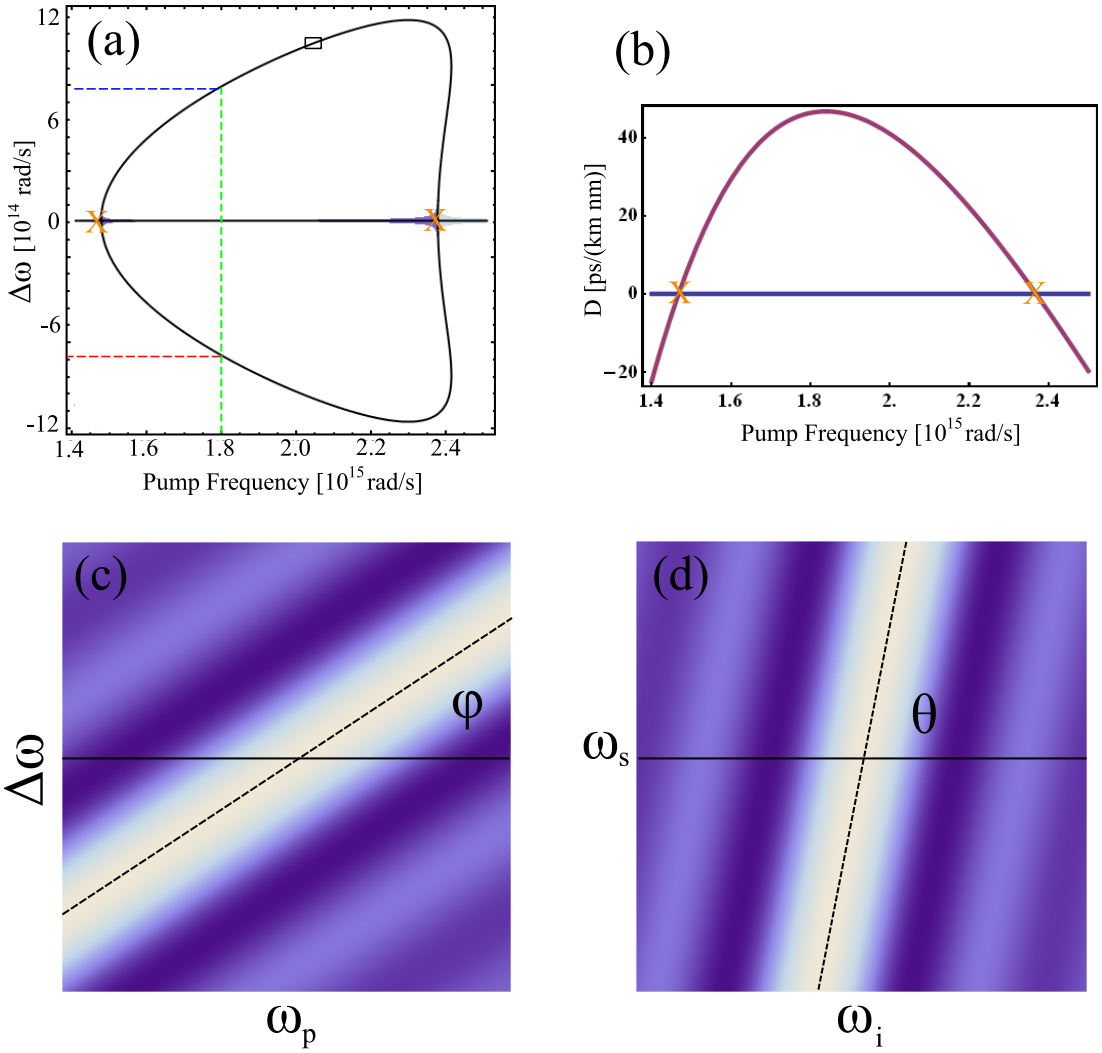

FIGURE 4.3. (a) Contour plot of the maximum of the phase-matching function for PCF fiber used in the experiment. The horizontal axis is the pump frequency in radians and the vertical axis is the frequency value of the sideband minus the pump frequency, also in radians. The green dashed line indicates an example pump value while the blue and red dashed lines illustrate the signal and idler frequencies that would results from that pump choice. The "X" markers mark the ZDWs of the fiber. (b) The D parameter for the fiber. The MI process almost always only occurs when the pump frequency is in an anomalous dispersion region, hence the contour of part (a) only existing between the "X" markers. (c) A zoomed-in region of the contour plot of part (a), labeled by a black box in part (a). For long pump pulses ($\sigma > 1$ps) the full phase-matching function is essentially a line with thickness dictated by σ and the fiber length having some angle φ. (d) A similar plot of the phase-matching function, except the pump frequency is fixed and the signal and idler values are allowed to vary. The angle the line makes is given by $\theta = \varphi + \pi/4$

idler. It consists of two lobes that are separated off the $\Delta\omega = 0$ axis by an amount proportional to the nonlinear dispersion shit γP. Except for very large input powers this separation is negligible. By convention, the signal is the higher wavelength but since the sidebands must be equally space in frequency magnitude from the pump the contour is symmetric around $\Delta\omega = 0$. As an example, the green dotted line indicates that a pump of frequency of 1.8×10^{15} rad Hz (1047 nm) is coupled into the fiber and that a signal of $\omega_p + 7 \times 10^{14}$ rad Hz and an idler of $\omega_p - 7 \times 10^{14}$ rad Hz are created. The extent of this phase-matching contour, the largest frequency at which there is a solution and the smallest frequency at which there is a solution, is related to the fiber's ZDW. As noted earlier, the pump must be in an anomalous dispersion region of the fiber in order for the MI effect to occur. Figure 4.3.(b) is a plot of the D parameter for this fiber. In both Figures 4.3.(a) and (b) the ZDW are marked with "x"s, and the placement of the marks in frequency is nearly identical.

This plot covers a wide range of pump wavelengths, which is the reason the general expression for $\Delta\beta$ must be used. Pictured in Figure 4.3.(c) is a far zoomed-in picture of the boxed region in Figure 4.3.(a) where the frequency ranges are on the order of several spectral pulse widths. Unlike the macroscopic contour plot, this contour plot has a noticeable thickness. This plot is showing most of the $\text{sinc}[L\Delta\beta/2]$ function, not just its maximum where the MI process is most efficient. This width is a consequence of the fiber dispersion characteristics and is inversely proportional to length. Also, it is essentially a straight line where the approximate expression for the phase-matching mismatch in (4.49) can be used. Being a line, it has a characteristic angle θ it makes with respect to the pump frequency ω_p versus $\Delta\omega = \omega_{s,i} - \omega_p$ basis. But this basis is not the basis in which the JSA is expressed, for that we need a plot where the basis is ω_s versus ω_i for a fixed pump frequency. The plot of Figure 4.3.(d)

shows a case where the central pump frequency in Figure 4.3.(c) was chosen and the ω_s and ω_i variables are allowed to vary. It is essentially the same Figure except that the line has been rotate by an amount of $\pi/4$. This is generally true for all ω_p versus $\Delta\omega$ to ω_s versus ω_i change of basis; all that is required is a rotation of $\pi/4$.

As mentioned before, the modulus squared of the JSA is the probability density distribution of the state. It also describes the spectral correlation that exists between the signal and idler modes and hence describes the amount of entanglement (or lack thereof) present in the quantum state. In particular, if the JSA can be written in such a manner that it is a product of two functions, each of which is only dependent either on the signal or idler frequency, then the signal and idler modes will exhibit no spectral correlation. Mathematically this is written as $F(\omega_s, \omega_i) = G(\omega_s) \cdot H(\omega_i)$. In this case the quantum state is factorable, where both signal and idler are pure states. Pure state creation is an active field of research due to applications in various quantum information processing technologies. On the other hand, if the JSA can in no way be written as a product of two independent functions then the signal and idler modes will exhibit complete spectral correlation. The creation of highly-correlated states is very much an active topic of research and has numerous applications, one of which (quantum cryptography) is already a commercially available product. In the case between these two extremes, where the signal and idler are somewhat spectrally correlated, the signal-idler state is said to be in a mixed state. Of course all states that can be physically realized fall into this category to a greater or lesser extent.

Using the linear approximation for the JSA, (4.50), the degree of spectral correlation can be readily calculated. In most cases it is possible to estimate the degree of correlation simply by inspecting the JSA. In Figure 4.4.(a) the "upper half" (signal) portion of the phase-matching contour is shown for the modeled dispersion

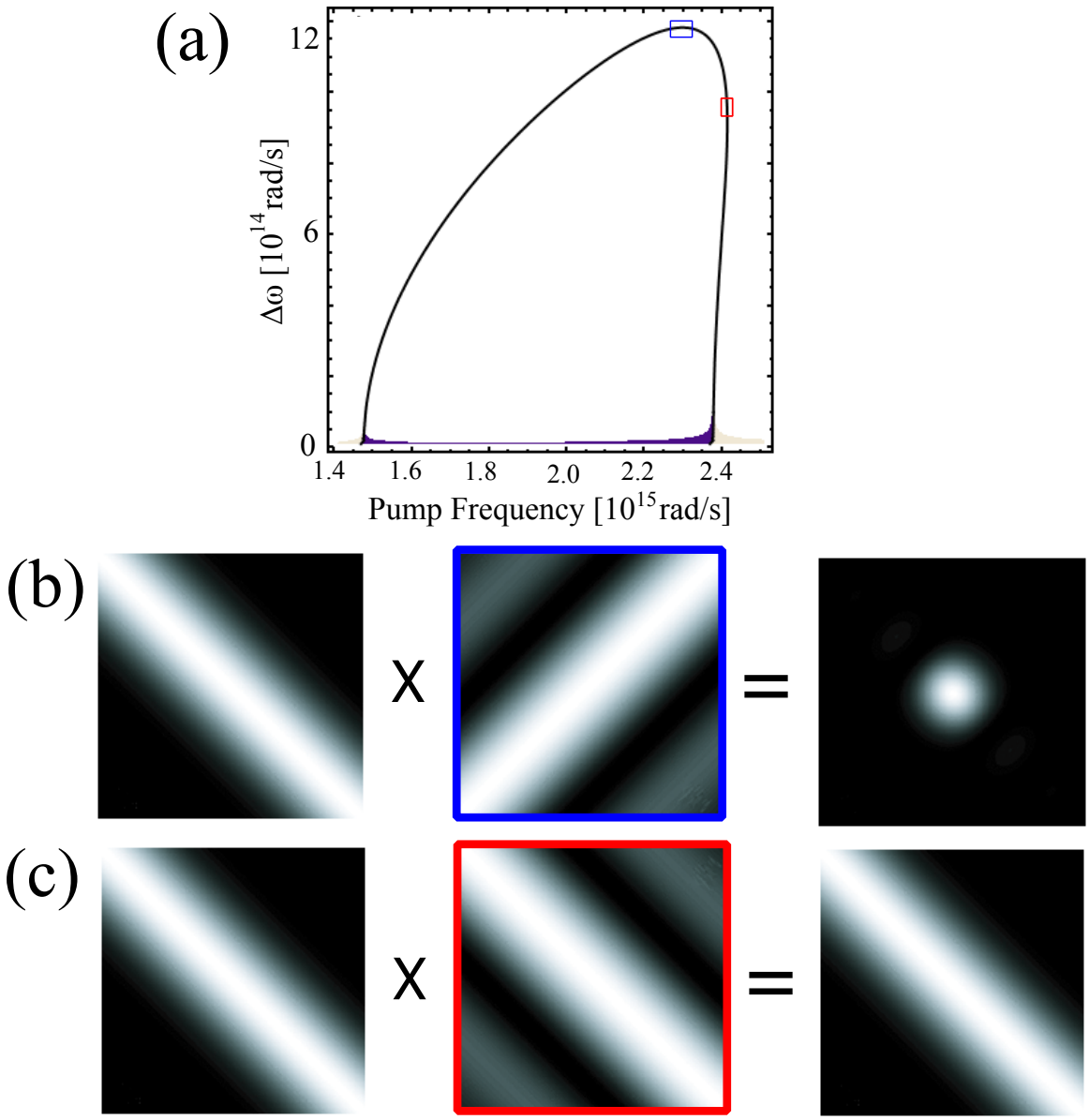

FIGURE 4.4. Pure and entangled states. (a) The "top-half" of the contour plot of figure 4.3.(a), which plots the central signal minus pump frequency versus pump frequency. The blue and red boxes represent regions where the slope of the contour is zero and infinity, respectively. (b) The resulting JSA when the pump frequency is aligned with the blue box in (a). The result is a JSA that to good approximation is a product of two independent functions of ω_s and ω_i, and hence the resulting quantum state is nearly separable. (c) The resulting JSA when the pump frequency is aligned with the red box in (a). This JSA shows nearly perfect correlation between signal and idler, hence the resulting quantum state will be nearly maximally entangled.

of a PCF fiber used in the experiment. The JSA at two regions of the contour, in the general area of the blue and red boxes, are examined in parts (b) and (c) of Figure 4.4.. These regions are where the contour reaches its highest point (zero slope) and its largest possible pump value (infinite slope). The first function in both parts (b) and (c) is the pump envelope function of (4.51) for a given pump width in signal-idler frequency space. It is essentially a line with slope -1, and will always be this way regardless of fiber properties. The second function in (b) and (c) is the sinc phase-matching function in sigma-idler frequency space for a particular fiber length of the blue and red regions in part (a) respectively. The zero slope of the contour in the blue region translates to a line of slope 1 and the infinite slope of the contour in the red region translates to a line of slope -1. Consequently, when the pump envelope function is multiplied by the phase-matching function to find the JSA as written in (4.50) significantly different functions for the two different regions are produced. For a phase-matching function with a slope of 1 the two functions have only minimal overlap, the region in which they cross. For a phase-matching function with a slope of -1 the two functions almost perfectly overlap. Hence in (b) a near circular function is produced that to good approximation is the product of two Gaussian functions each only a function of the signal frequency or the idler frequency.[5] Since the JSA can be accurately approximated as a product of two independent functions the signal and idler modes are not spectrally correlated, and the state is separable. In the case shown in (c) the resulting JSA, only partially shown, to good approximation cannot be written to any degree as the product of two independent functions, and is therefore nearly maximally entangled. As can be easily surmised, a state of any particular

[5]The sinc function of the phase-matching function produces small, but not negligible, tails of amplitude that persist through to the JSA. These side lobes decrease the purity of the state, but can be spectrally filtered so that the state only consists of only the central double Gaussian. This causes a small loss in throughput.

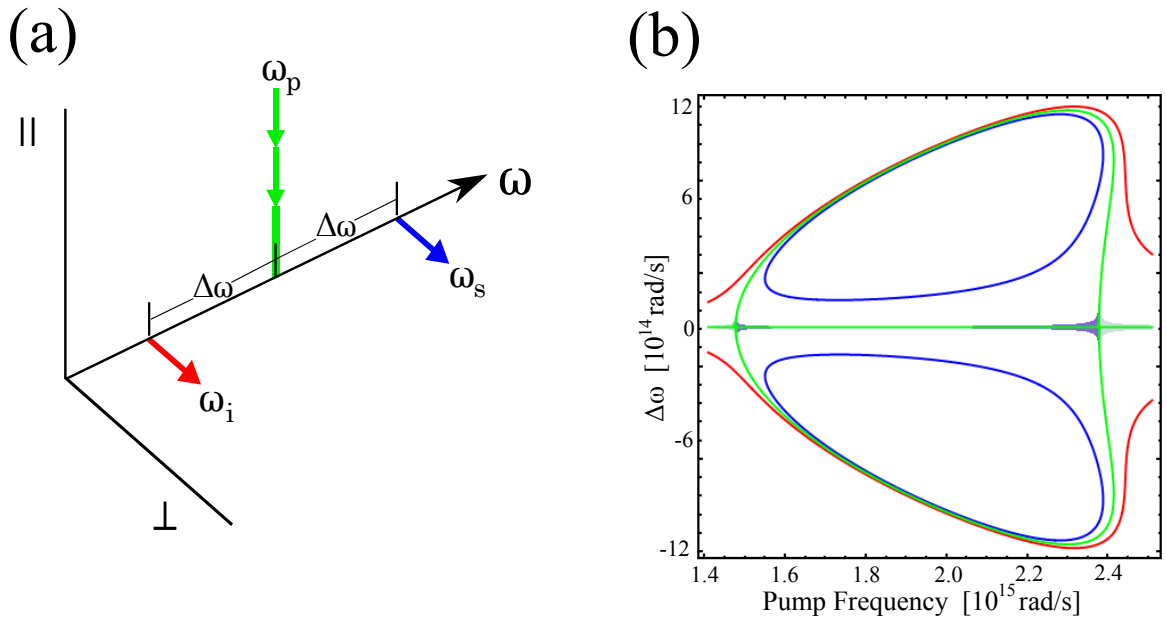

FIGURE 4.5. (a) A diagram of the $xx \rightarrow yy$ birefringent MI process where two pump photons are annihilated (down arrows) and two sideband signal and idler photons are created (up arrows). The magnitude of the frequency difference between pump and either sideband, $|\Delta\omega|$, is the same due to energy conservation. The parallel and perpendicular axis could represent either the slow or fast axis. (b) The phase-matching contour plot for the birefringent MI process. The red, green and blue contours are the resulting contours for negative, zero and positive birefringence. The blue contour exhibits two distinct non-degenerate sideband pair solutions for a given pump frequency.

degree of entanglement can be created by choosing a region of the phase-matching contour with the appropriate slope. The exact value of the spectral correlation can be found by carrying out a Schmidt-mode decomposition of the JSA [15].

The above analysis did not take into consideration the phenomenon of birefringence. In a realistic situation, pumping a non-birefringent with linearly polarized light will eventually lead to polarization scattering of the pump and any signal or idler photons. Therefore if it is desirable to keep all MI products in the same polarization state as that of the pump, a polarization-maintaining fiber with the pump aligned to either the fast or slow axis must be used. Interestingly, if the condition of

having the sideband photons in the same polarization state as the pump is relaxed, several other polarization configurations are possible for the MI process. An extra law now comes into play where the angular momentum of the initial pump photons must be conserved, which has the consequence that the polarizations of the four involved photons must come in pairs [60, 78]. Therefore there are three configurations in which the MI process can occur: if x stands for a photon on either the fast or the slow axis while y stands for a photon on the opposite axis of that of x then the allowed process are $xx \rightarrow xx$, $xy \rightarrow xy$ and $xx \rightarrow yy$. The above analysis was for the first case, where all waves are polarized on the same axis. Figure 4.5.(a) shows the latter case, where the pump photons are polarized on opposite axis to that of the sidebands. In practice this case allows for the most flexible arrangement of pumps and products while also allowing easy filtering of the exit pump field from the sidebands. This is the configuration used in the experimental setup and was first reported in 1981 [79] in regular fiber, and in PCF in 2006 [80].

The equivalent phase-mismatch function, analogous to (4.37), is given by

$$\Delta\beta_{xxyy} = 2\beta_{p,x} - (\beta_{s,y} + \beta_{i,y} + \frac{2}{3}\gamma P) \cong 2\beta_{p,x} - (\beta_{s,x} + \beta_{i,x} + 2\frac{\Delta n\omega_p}{c} + \frac{2}{3}\gamma P) \quad (4.52)$$

where Δn is the birefringence. The nonlinear constant, and hence the nonlinear dispersion term, is a third the value in the co-polar case of (4.37) [81]. The above approximation is accurate when the birefringence is nearly independent of pump wavelength, which is generally the case [60]. The sign of Δn is dependent on which axis the pump is on; if it is on the fast axis then Δn is negative, if it is on the slow axis then Δn is positive. Figure 4.5.(b) shows the three qualitative configurations, where Δn is negative (red), zero (green), and positive (blue). For the $\Delta n = 0$ scenario the $xx \rightarrow xx$ and $xx \rightarrow yy$ frequency solutions are degenerate. Notice that for the blue

contour there are effectively two sets of sideband pairs for any given pump frequency; an outer pair with large frequency separation from the pump and an inner pair with small frequency separation. Since the outer pair is usually separated by quite a large amount, where the signal is in the visible regime and the idler is in the infrared, the existence of the inner pair solutions is useful in situations where one wants to be able to detect both sidebands with similar detectors that have limited detection range. In the work being presented in this dissertation the sidebands are created in this manner due to the need to use single-photon detectors that only function in the visible and near-infrared.

4.3.2. Bragg-Scattering: Photon Frequency Translation

In $\chi^{(3)}$ media the FWM processes responsible for photon translation is called Bragg scattering (BS) and requires the presence of two frequency non-degenerate pump fields. The BS process is in some sense quite similar to translation via sum/difference generation (SG and DG respectively) in $\chi^{(2)}$ media [72]. In SG, or upconversion, an input pump at frequency ω_p combines with one input idler photon at frequency ω_i to create a new signal photon at a frequency $\omega_s = \omega_p + \omega_i$. The dispersion of the fields in the medium must be matched for this process to occur efficiently. Although an experiment done in 1992 [21] showed nonclassical intensity correlations between two fields originating from SPDC, of which one field was upconverted, it wasn't until recently in 2010 that single photon input was shown to also be in a single photon state after the upconversion process [82]. In DG, or downconversion, an input pump at frequency ω_p combines with one input idler photon at frequency ω_i to create a new signal photon at a frequency $\omega_s = \omega_p - \omega_i$. This process was shown recently [23]. The reason that the signal photon frequency is the difference of the pump and

idler and not the sum is that in this case the dispersion of the medium is such that these three frequencies are phase matched.

The SG process is more analogous to the BS process than is DG for at least one key reason. Both SG and BS are stimulated effects, that is, they require the presence of the idler and will not produce photons at the signal frequency even when the pump(s) is (are) present. The DG process, on the other hand, will occur both spontaneously, when no idler photon is present, and from stimulation by the idler photon. In that way DG is more akin to MI and PC, which can be used to translate fields from the idler to the signal and vice versa [83]. Translation under DG, MI, and PC can amplify the power (or increase the number of photons) in the translated mode, whereas in SG and BS no amplification occurs (photon number is conserved). The importance of SG and BS only being stimulated effects is that the signal mode will not be populated by "noise" photons, photons that are created in the signal mode even when an idler photon is not present. This is a particularly good property in the case of translating quantum states of light which, due to their low intensity, are particularly sensitive to noise.

Although SG and BS share similar properties there are key differences in their practical implementation and utility. BS is a two-pump process where the pumps have frequency ω_p and ω_q interact with the signal and idler frequencies so that $\omega_p+\omega_i = \omega_q+\omega_s$, whereas SG is a one pump process. Depending on particular circumstances this could either make translation by BS more cumbersome, due to the extra complexity of needing two pump lasers, or more flexible, in that one doesn't need one particular laser frequency to effectively translate the idler field (or in some circumstances, both cumbersome but flexible). But BS offers a significant advantage over SG in terms of the range of frequency translation that is in practice possible. Since in BS the

frequency difference between the two pumps $\Delta\omega$ is equal to the frequency difference between the signal and idler it is not hard to see that it is equally easy to translate by small $\Delta\omega$ as it is to translate by large $\Delta\omega$. For translation by small $\Delta\omega$, the pumps need to be close to another in wavelength, such as two titanium-sapphire lasers lasing around 800 nm. Translating by small $\Delta\omega$ could be useful for communication between quantum memory devices or for quantum repeaters [84]. For large $\Delta\omega$ the pumps must have significantly different wavelengths, like possibly a frequency doubled Nd:YAG laser at 532 nm and a titanium-sapphire laser. Since in the SG process there is only one pump, the single pump frequency must equal the difference between signal and idler. For large $\Delta\omega$ this is no problem, but for small $\Delta\omega$ the pump must have a very large wavelength for translation to the visible and infrared, in the tens of microns or even millimeters. Coherent sources at those wavelengths not common, and it is quite likely that for most $\chi^{(2)}$ materials efficient phase-matching of such disparate wavelengths is not feasible.

To achieve a quantitative understanding of the BS process we first turn to classical sideband theory, in the same manner in which the MI process was first analyzed. Starting from (4.30) and (4.31), plugging the resulting field into (4.25), collecting terms of like frequency, discarding terms with small contributions and solving for the signal and idler amplitudes yields the coupled equations for CW fields

$$d_z B_i^* = -i((\beta_i - \beta_2) + \gamma P_1)B_i^* - i2\gamma(P_1 P_2)^{1/2} B_s^* \tag{4.53}$$

$$d_z B_s^* = -i((\beta_s - \beta_1) + \gamma P_2)B_s^* - i2\gamma(P_1 P_2)^{1/2} B_i^*. \tag{4.54}$$

By solving these equations the manner in which power is transferred from the idler to the signal mode can be seen. Again, assume that the normalized power of the

idler and signal fields (proportional to $|B_{i(s)}|^2$) is given at the input of the fiber by $P_s(0) = 0$ and $P_i(0) = 1$. Then the powers as a function of z are

$$P_i(z) = 1 - (4\gamma^2 P_1 P_2/\kappa_{BS}^2)\sin^2(\kappa_{BS} z) \tag{4.55}$$

$$P_s(z) = (4\gamma^2 P_1 P_2/\kappa_{BS}^2)\sin^2(\kappa_{BS} z) \tag{4.56}$$

where

$$\kappa_{BS} = (1/4[\Delta\beta_{BS} + \gamma(P_2 - P_1)]^2 + 4\gamma^2 P_1 P_2)^{1/2} \tag{4.57}$$

The quantity $\Delta\beta_{BS}$ is the combination of the material and waveguiding dispersive mismatch from (3.8), and is given by

$$\Delta\beta_{BS} = \beta(\omega_1) + \beta(\omega_s) - (\beta(\omega_2) + \beta(\omega_i)) \tag{4.58}$$

where the term $\gamma(P_2 - P_1)$ is the nonlinear dispersive mismatch.

There are a couple of features of this solution to point out. For a given fiber length, the overall efficiency of the translation process can be sensitive to the dispersion mismatch $\Delta\beta_{BS}$, which can easily become much larger than the other terms of κ_{BS}. Also, the sum of signal and idler power is always constant, and for long enough fiber lengths power will oscillate between the two modes. Since the sum of powers of the signal and idler is constant, the BS process is theoretically noise-free, which is an important property for quantum-level translation.

Before continuing to the quantum BS theory we will comment on where the BS process takes place in regards to the input field frequencies and the fiber properties. As (4.58) notes, the dispersion mismatch (not including the nonlinear term, which is usually very small compared to material and waveguiding terms) is the dispersion

difference between the fields being annihilated and the fields being created/amplified. Let us expand this expression around ω_A, the average value of the frequencies of all four fields, so that it is the "center of energy" of the BS process. Also, denote the frequency difference between the higher-frequency field to be annihilated and ω_A as $\delta_1\omega$. Similarly, denote the frequency difference between the higher-frequency field to be created and ω_A as $\delta_2\omega$. Both of these difference quantities, along with $\Delta\omega$, are pictured in Figure 4.6. (a). Expanding out the dispersion in a Taylor series leaves

$$\Delta\beta_{BS} = \beta^{(2)}|_{\omega_A}(\delta_1\omega^2 - \delta_2\omega^2) + \ldots \frac{2}{2n!}\beta^{(2n)}|_{\omega_A}(\delta_1\omega^{2n} - \delta_2\omega^{2n}) + \ldots \tag{4.59}$$

where n is an integer and the derivatives are evaluated at ω_A. Interestingly, the first two orders of β cancel out; the first because the expression to zeroth order is $2\beta^{(0)}|_{\omega_A} - 2\beta^{(0)}|_{\omega_A}$ and the second due to the sign of the term multiplying $\beta^{(1)}|_{\omega_A}$ each canceling each other out, which incidentally cancels out all odd orders. Now, in real fibers, the first term $\beta^{(2)}|_{\omega_A}(\delta_1\omega^2 - \delta_2\omega^2)$ will be significantly larger than all other terms in the series for arbitrary input field frequency values, with the overall magnitude of higher order terms dropping rapidly. Hence the most likely scenario for when the BS process will be phase matched is when this first term is as small as possible. But the term involving the field frequencies multiplying the second-order derivative in general is not zero or even small; if that were the case there would be no meaningful frequency translation. Therefore the derivative term $\beta^{(2)}|_{\omega_A}$ must be very small or zero. This of course happens when the value of ω_A corresponds closely with the ZDW; in fact, to first order, ω_A must be equal to the frequency equivalent of one of the fiber's ZDW. In practice ω_A does not exactly correspond to a ZDW; higher order terms in the series do play a role, shifting the value of ω_A away from the equivalent ZDW. But in the author's experience ω_A has always been quite close to

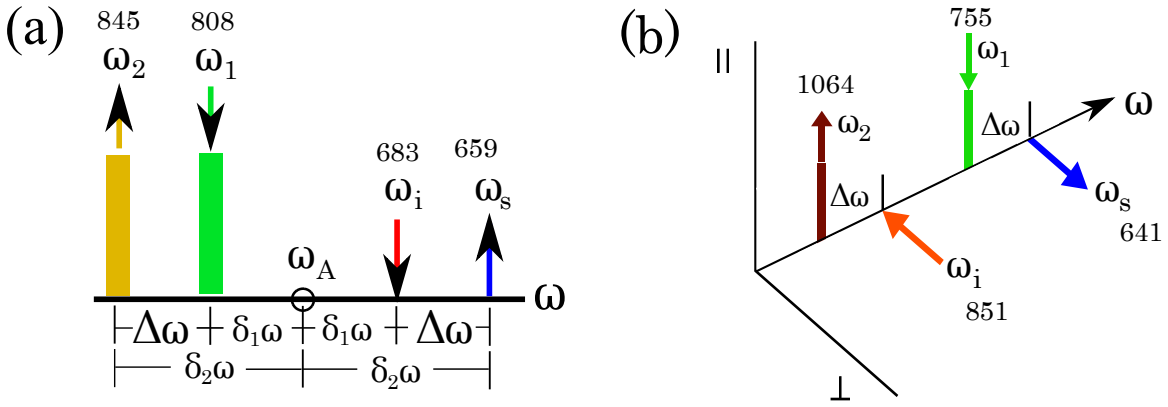

FIGURE 4.6. Bragg-scattering diagrams. (a) Diagram of the co-polarized BS process. The numbers above the fields are the central wavelengths in nanometers of the fields in the experiment. The quantity $\Delta\omega$ is the frequency difference of the pumps, equal to the frequency difference of the sidebands. The quantity $\delta_1\omega$ ($\delta_2\omega$) is the frequency differences between the annihilated (created) photons and the average frequency of all four fields. The frequency ω_A is the average frequency of the fields. (b) An example of birefringent BS, where the pumps are polarized on one axis and the signal and idler are polarized on the other. The numbers above the fields are the central wavelengths in nanometers of the fields from [85] where the process was first demonstrated.

the corresponding ZDW, and so to good approximation the center of energy of a BS process is one of the fiber's ZDWs.

We now turn to a simplified quantum mechanical picture of the BS process, where one idler field mode is annihilated and one signal field mode is created. The pumps are also taken to be CW fields. The process is shown in Figure 4.6.(a) for co-polarized fields (similar to $xx \rightarrow xx$) and in Figure 4.6.(b) for one particular birefringent configuration (similar to $xy \rightarrow xy$). We will focus on the former, since that is the configuration used in the work presented in this dissertation, but it is interesting to note the later configuration was used to demonstrate the largest BS translation effect to date [85]. The process is governed by the Hamiltonian

$$\mathcal{H} = \delta(a_i^\dagger a_i - a_s^\dagger a_s) + \rho a_i^\dagger a_s + \rho^* a_s^\dagger a_i \tag{4.60}$$

where the creation/annihilation operators satisfy the usual commutation relations, and δ and ρ are parameters quantifying the effects of phase-mismatch and nonlinearity [24]. The evolution is given by the spatial equations-of-motion (with a minus sign compared to the usual time-domain Heisenberg equation)

$$d_z a_{s(i)}(z) = i[a_{s(i)}(z), \mathcal{H}]. \tag{4.61}$$

The solution of (4.61) for $a_{i(s)}(z)$ as a function of fiber length z is given by

$$a_i(z) = \mu(z)a_i(0) + \nu(z)a_s(0) \tag{4.62}$$

$$a_s(z) = \mu^*(z)a_s(0) - \nu^*(z)a_i(0) \tag{4.63}$$

where the so-called transfer functions are given by

$$\mu(z) = \cos(\kappa z) + i\delta \sin(\kappa z)/\kappa \tag{4.64}$$

$$\nu(z) = i\rho \sin(\kappa z)/\kappa \tag{4.65}$$

where $\kappa = (|\rho|^2 + \delta^2)^{1/2}$. The transfer functions have the relation $|\mu|^2 + |\nu|^2 = 1$, which ensures the process is unitary and conserves photon numbers. Also, from comparing the parameters in the quantum case to the classical case of (4.55) and (4.56) it is clear that δ is closely related to $\delta\beta$, while the κ are identical. Mathematically, the BS translation process having frequency input and output "ports" is identical to the normal beamsplitter operation on monochromatic fields interacting through a beamsplitter [86].

We now examine how a single photon in the idler mode is transferred to the signal mode. This state is denoted by $|1, 0\rangle_{\text{in}}$. The state can also be written as

$|1,0\rangle_{\text{in}} = a_i^\dagger(0)|0,0\rangle$, and by using the inverted relations of the transfer functions relations $a_i^\dagger(0) = \mu(z)a_i^\dagger(z) - \nu(z)^* a_s^\dagger(z)$, the state becomes

$$|1,0\rangle_{\text{in}} = \mu(z)|1,0\rangle_{\text{out}} - \nu(z)^*|0,1\rangle_{\text{out}}, \tag{4.66}$$

where in and out denote the state at the fiber input and output. If the parameters are chosen such that $|\nu(z)| = 1$, then the idler mode will be perfectly translated to the signal mode. The process is similar for multi-photon states.[6]

Pure states are not the only type of state that can be translated; entangled states can be translated while preserving their entangled properties. For example, suppose the input consisted of two photon inputs at different frequencies ω_i and ω_i'. In this case the Hamiltonian will consist of twice as many terms, those from the originally unprimed signal and idler and those from the new primed signal and idler. The evolution of the entire system can be regarded as the evolution of the primed and unprimed individual systems. The input state could then be denoted by $|1,0;1,0\rangle_{\text{in}}$, and similar to (4.66) the input can be written as a function of the output as

$$\begin{aligned} |1,0;1,0\rangle_{\text{in}} =& \mu(z)\mu'(z)|1,0;1,0\rangle_{\text{out}} - \mu(z)(\nu'(z))^*|1,0;0,1\rangle_{\text{out}} \\ & - \mu'(z)\nu^*(z)|0,1;1,0\rangle_{\text{out}} + \nu^*(z)(\nu'(z))^*|0,1;0,1\rangle_{\text{out}}. \end{aligned} \tag{4.67}$$

Similar to the single mode input, if $|\nu(z)| = |\nu'(z)| = 1$ the two photon input state would be translated to $|0,1;0,1\rangle_{\text{out}}$. If the input was an entangled state, such as $|0,0;0,0\rangle + |1,0;1,0\rangle$, then the output state would be similarly entangled, equalling $|0,0;0,0\rangle + e^{i\phi}|0,1;0,1\rangle$, where ϕ is a phase shift related to ν.

[6]The translated single photon state will pick up a phase factor of $\phi = \pi - \arg(\nu)$. In general the translation of a state with n idler photons will pick up a phase of $n\phi$. Translation does not affect the coherence of the state; if the input was coherent, then the output would be as well.

The above analysis was carried out only for CW input fields where each particular idler field corresponded to one particular signal field. The more complicated, and much more realistic, scenario is where all fields (both pumps, signal, and idler) contain multiple frequencies. In that case each idler mode at a given frequency corresponds to many signal modes, and vice versa [87]. The solution for the fields as a function of fiber length cannot be solved analytically for arbitrary wavepacket input; the output wavepackets must be computed numerically [60]. However, it is possible to assign analytically a transfer function G in either frequency or time that relates the input wavepacket to the output wavepacket for arbitrary input, analogous to (4.62) and (4.63), for given pump spectra, fiber dispersion, and fiber length. This function is an instance of a Green's function [88] and the input/output relation in frequency (similarly in time) for the creation operator at a particular frequency ω is

$$a^\dagger(z=0,\omega) = \int d\omega' G(\omega,\omega') a^\dagger(z=L,\omega'), \tag{4.68}$$

where $z=0$ and $z=L$ denote the beginning and end of the fiber [33]. A wavepacket with multiple frequencies given by $\int d\omega A(0,\omega) a^\dagger(z=0,\omega)$ is translated in the manner given by (4.68). The output state will then be

$$\int d\omega A(0,\omega) a^\dagger(0,\omega) = \int d\omega A(0,\omega) \int d\omega' G(\omega,\omega') a^\dagger(L,\omega'). \tag{4.69}$$

The transfer function is unitary and satisfies the condition

$$\int d\omega' G(\omega,\omega') G^*(\omega'',\omega') = \delta(\omega-\omega''). \tag{4.70}$$

To facilitate an intuitive understanding of the transfer function we will break up frequency space into two pieces; the range that contains the idler and the range that contains the signal [33]. Each operator or variable will be denoted by an "I" or "S" subscript. For example, the creation operator for an idler photon at a particular idler frequency will be written as $a_I^\dagger(\omega_I)$. In this case the transfer function can be written in block form as

$$\begin{bmatrix} G_{II}(\omega_I, \omega_I') & G_{SI}(\omega_S, \omega_I') \\ G_{IS}(\omega_I, \omega_S') & G_{SS}(\omega_S, \omega_S') \end{bmatrix} \tag{4.71}$$

where G_{AB} refers to the evolution of an operator that began in range B but scatters (translates or doesn't translate) to range A. The idler and signal input creation operators can then be written as

$$a_I^\dagger(0, \omega_I) = \int d\omega_I' G_{II}(\omega_I, \omega_I') a^\dagger(L, d\omega_I') + \int d\omega_S' G_{SI}(\omega_S, \omega_I') a^\dagger(L, d\omega_S') \tag{4.72}$$

$$a_S^\dagger(0, \omega_S) = \int d\omega_S' G_{SS}(\omega_S, \omega_S') a^\dagger(L, d\omega_S') + \int d\omega_I' G_{IS}(\omega_I, \omega_S') a^\dagger(L, d\omega_I') \tag{4.73}$$

The unitary conditions for the four sub-transfer functions are

$$\int d\omega_I' G_{II}(\omega_I, \omega_I') G_{II}^*(\omega_I'', \omega_I') + \int d\omega_S' G_{IS}(\omega_I, \omega_S') G_{IS}^*(\omega_I'', \omega_S') = \delta(\omega_I - \omega_I'') \tag{4.74}$$

$$\int d\omega_I' G_{SI}(\omega_S, \omega_I') G_{II}^*(\omega_I'', \omega_I') + \int d\omega_S' G_{SS}(\omega_S, \omega_S') G_{IS}^*(\omega_I'', \omega_S') = 0 \tag{4.75}$$

Unfortunately, the transfer function cannot be solved analytically for arbitrary input. But it is possible to accurately numerically calculate G up to some known, given error, which is usually sufficient for practical concerns. In the next chapter we will discuss numerical solutions for realistic input wavepackets in realistic models of optical fiber.

4.3.2.1. Two-Color Hong-Ou-Mandel Interference

As an interesting example of the phenomenon that can occur due to quantum BS, we derive the so-called two-color Hong-Ou-Mandel interference effect. The "regular" Hong-Ou-Mandel interference (HOMI) effect occurs when two photons, identical in every respect except for their propagation direction, are incident on different ports of a 50/50 beamsplitter [89]. Due to the quantum nature of single photons, which have no defined phase, the incident photons will either both emerge in one output port of the beamsplitter or both emerge in the other output port. This is due to the wavepacket terms corresponding to one photon emerging in one port and one in the other canceling out, leaving only the two-photons-in-the-same-port states with non-zero amplitude. In general the output state of the bi-photon state can be written as

$$\psi\rangle = C_{11}|1,1\rangle + C_{20}|2,0\rangle + C_{02}|0,2\rangle, \tag{4.76}$$

where $|i,j\rangle$ denotes the state in which i photons are in one output port and j photons are in the other. The entire state $\psi\rangle$ must be normalized and the component states are orthonormal.

We predicted that an analogous effect occurs for the BS process, except instead of input spatial ports the photons are input in different frequency "ports," or modes [33]. Hence if parameters are set correctly (good phase matching, pump powers, fiber nonlinearity, and fiber length) such that 50 percent translation occurs two input photons, one in the signal and one in the idler modes, both photons will emerge in either the idler or in the signal mode. While this process was treated generically in our prior paper [33], in the following we extend that treatment in order to put the results into a form that explicitly predicts the photon-counting statistics.

For idler and signal input modes that have input spectrums of $A_I(0,\omega_I)$ and $A_S(0,\omega_I)$ respectively, the output state according to (4.69), (4.72), and (4.73) will be

$$\begin{aligned}|\psi\rangle_{out} =&\Big[\int d\omega A_I(0,\omega)\int d\omega_I G_{II}(\omega,\omega_I)a_I^\dagger(\omega_I)+\\ &\int d\omega A_S(0,\omega)\int d\omega_S G_{IS}(\omega,\omega_S)a_S^\dagger(\omega_S)\Big]\\ &\cdot\Big[\int d\omega^{'} A_I(0,\omega^{'})\int d\omega_I^{'} G_{SI}(\omega^{'},\omega_I^{'})a_I^\dagger(\omega_I^{'})+\\ &\int d\omega^{'} A_S(0,\omega^{'})\int d\omega_S^{'} G_{SS}(\omega^{'},\omega_S^{'})a_S^\dagger(\omega_S^{'})\Big]|vac\rangle\end{aligned} \tag{4.77}$$

Let us closely examine the very first term, which describes how an idler photon wavepacket is scattered into another idler photon wavepacket. The spectra of these two wavepackets overlap, but are not necessarily identical. If the order of integration over variables $d\omega_I$ and $d\omega$ is switched then this term reads as

$$\int d\omega_I a_I^\dagger(\omega_I)\left[\int d\omega A_I(0,\omega)G_{II}(\omega,\omega_I)\right], \tag{4.78}$$

where the term in brackets describes how the amplitude function of a *classical* idler input field is scattered to another classical idler field at the output. In fact, the term in brackets is just the output amplitude at ω_I of the idler field at the output where $z = L$. Hence this first term becomes

$$\int d\omega_I a_I^\dagger(\omega_I)\left[\int d\omega A_I(0,\omega)G_{II}(\omega,\omega_I)\right] \rightarrow \int d\omega_I a_I^\dagger(\omega_I)A_{II}(L,\omega_I). \tag{4.79}$$

where the double subscript of $A_{II}(L,\omega)$ refers to idler amplitude at ω that scatter from initially idler amplitude. Similarly, $A_{IS}(L,\omega)$, $A_{SS}(L,\omega)$, and $A_{SI}(L,\omega)$ refer to idler/signal/signal amplitude at the output that originated from signal/signal/idler amplitude at the input, respectively.

Through the use of (4.79), (4.77) can be written much more compactly, using the amplitude at the output, as

$$\begin{aligned}|\psi\rangle_{out} =&\Big[\int d\omega_I a_I^\dagger(\omega_I)A_{II}(L,\omega_I) + \int d\omega_S a_S^\dagger(\omega_S)A_{SI}(L,\omega_S)\Big] \\ &\cdot\Big[\int d\omega_I^{'} a_I^\dagger(\omega_I^{'})A_{IS}(L,\omega_I^{'}) + \int d\omega_S^{'} a_S^\dagger(\omega_S^{'})A_{SS}(L,\omega_S^{'})\Big]|vac\rangle.\end{aligned} \tag{4.80}$$

When fully expanded (4.80) consists of four terms. Two of the terms, that contain the $a_I^\dagger(\omega_I)a_S^\dagger(\omega_S^{'})$ and $a_S^\dagger(\omega_S)a_I^\dagger(\omega_I^{'})$ operators, relate to the creation of one idler photon and one signal photon. Since these terms correspond to the same Hilbert sub-space, $|1,1\rangle$, we can combine them to into one term. The other two terms, those that contain the $a_I^\dagger(\omega_I)a_I^\dagger(\omega_I^{'})$ and $a_S^\dagger(\omega_S)a_S^\dagger(\omega_S^{'})$ operators, relate to the creation of either two idler photons or two signal photons. Since these terms do not correspond to the same Hilbert sub-space ($|2,0\rangle$ and $|0,2\rangle$) respectively) the terms cannot be combined.

The probability, given a particular output state, for the various sub-space states to occur is simply given by the modulus squared of the coefficients of these states, $|C_{ij}|^2$. For the $|1,1\rangle$ state the coefficient is found by acting the aforementioned operators, with their accompanying functions, on the vacuum, yielding

$$|\psi_{11}\rangle = \int\int d\omega_I d\omega_S \left(A_{II}(L,\omega_I)A_{SS}(L,\omega_S) + A_{IS}(L,\omega_I)A_{SI}(L,\omega_S)\right)|1_{\omega_I},1_{\omega_S}\rangle \tag{4.81}$$

where $\omega_S^{'}$ was taken into ω_S since in this case these variables are only dummy variables. The first term, $A_{II}(L,\omega_I)A_{SS}(L,\omega_S)$, corresponds to the case where a photon initial in the idler mode scatters to the idler mode at the output, and where a photon initial in the signal mode scatters to the signal mode at the output. The second term, $A_{IS}(L,\omega_I)A_{SI}(L,\omega_S)$, corresponds to the case where a photon initial in the idler mode

scatters to the signal mode at the output, and where a photon initial in the signal mode scatters to the idler mode at the output. Since these terms are being added before their modulus squared is taken, there is the chance that they could cancel if the terms are proportional and out of phase with one another. This is exactly what happens in the case in which HOMI occurs, leaving zero probability amplitude for the field to emerge in the $|1,1\rangle$ state.

Hitting the above ket vector against its corresponding conjugate bra vector yields $P11 = |C_{11}|^2$, the probability the photons will emerge in different frequency modes. Since ω_I and ω_S are independent variables, the expression for $P11$ is

$$P11 = \int\int d\omega_I d\omega_S^{'}\big[|A_{II}(L,\omega_I)|^2|A_{SS}(L,\omega_S)|^2 + |A_{IS}(L,\omega_I)|^2|A_{SI}(L,\omega_S)|^2 + 2\mathrm{Re}[A_{II}(L,\omega_I)A_{SS}(L,\omega_S)A_{IS}^*(L,\omega_I)A_{SI}^*(L,\omega_S)|]\big]. \tag{4.82}$$

The expression for the probability of the $|2,0\rangle$ and $|0,2\rangle$ states is somewhat trickier to derive due to the possibility that degenerate photons would be created in the idler and signal frequency regions. In this case the primed variables attached to the operators cannot be taken over to their unprimed counterparts (as $\omega_S^{'}$ to ω_S was for example). This ambiguity can be avoided by calculating $P20$ directly as the product of the appropriate bra and ket vectors (similarly $P02$). From (4.80) the term

corresponding to the creation of two idler photons leads to an expression for $P20$ of

$$\begin{aligned} P20 = \langle \psi_{20} || \psi_{20} \rangle &= \langle vac | \left(\int \int d\bar{\omega}_I d\bar{\omega}_I^{'} a_I(\bar{\omega}_I) a_I(\bar{\omega}_I^{'}) A_{II}^*(L, \bar{\omega}_I) A_{IS}^*(L, \bar{\omega}_I^{'}) \right) \\ &\cdot \left(\int \int d\omega_I d\omega_I^{'} a_I^\dagger(\omega_I) a_I^\dagger(\omega_I^{'}) A_{II}(L, \omega_I) A_{IS}(L, \omega_I^{'}) \right) |vac\rangle \\ &= \langle vac | \int \int \int \int d\bar{\omega}_I d\bar{\omega}_I^{'} d\omega_I d\omega_I^{'} A_{II}^*(L, \bar{\omega}_I) A_{IS}^*(L, \bar{\omega}_I^{'}) A_{II}(L, \omega_I) A_{IS}(L, \omega_I^{'}) \\ & a_I(\bar{\omega}_I) a_I(\bar{\omega}_I^{'}) a_I^\dagger(\omega_I) a_I^\dagger(\omega_I^{'}) |vac\rangle, \end{aligned} \tag{4.83}$$

where the variables of the conjugate wavefunction are denoted with an overhead bar. The key to evaluating this expression is to utilize the field commutation relation. In the frequency variable the commutation relation is $[a(\omega), a^\dagger(\omega^{'})] = \delta(\omega - \omega^{'})$ or, in a form more applicable to the current case, $a(\omega)a^\dagger(\omega^{'}) = \delta(\omega - \omega^{'}) + a(\omega)^\dagger a(\omega^{'})$. The ordering of the operators is crucial, as they do not commute in general. Hence the commutation relation must be used on the inner most operators:

$$a_I(\bar{\omega}_I^{'}) a_I^\dagger(\omega_I) = \delta(\bar{\omega}_I^{'} - \omega_I) + a_I^\dagger(\omega_I) a_I(\bar{\omega}_I^{'}). \tag{4.84}$$

This breaks the expression up into two parts, and leads to the expression, employing dummy variable notation, of

$$P20 = \left| \int \omega A_{II}^*(L, \omega) A_{IS}(L, \omega) \right|^2 + \int d\omega d\omega^{'} |A_{II}(L, \omega)|^2 |A_{IS}(L, \omega^{'})|^2. \tag{4.85}$$

The expression for $P02$ is the same when $A_{II} \rightarrow A_{SS}$ and $A_{IS} \rightarrow A_{SI}$. The two terms of (4.85) have distinct physical interpretations. The first term, derived in part from the delta function of (4.84), is essentially the overlap of the two spectral functions A_{II} and A_{IS}, and accounts for cases in which the two idler photons are created in the

same mode. This purely quantum mechanical term arises from the bosonic nature of photons, the operators of which obey the above mentioned commutation relation. The second term accounts for the cases in which the two idler fields are purely classical, as if these fields did not obey the quantum bosonic commutation relations.

Although this calculation was done in very general terms, it was possible to assign clear physical meaning to the various parts of the final expressions for $P11$, $P20$, and $P02$. For $P11$, there was the possibility that the amplitudes involved in the final expression would cancel to some degree or completely. This is certainly a quantum effect; for independent classical sources averaged out over all phases the corresponding quantity would be a half, but for quantum single-photon sources, where phase cannot be defined, the probability can drop all the way to zero. Similarly for the $P20$ and $P02$ cases, there is a term due to the bosonic nature of photons that gives a quantitatively different results from the corresponding classical case. We will see in the next chapter under what particular conditions the quantum nature of this effect can be distinguished from the corresponding classical behavior.

CHAPTER V

NUMERICAL EVOLUTION AND BRAGG SCATTERING

In most realistic circumstances, taking into account actual field shapes and real fiber dispersion properties, it is not possible to solve the nonlinear Schrödinger equation analytically. So we turn to numerical computation to compute the evolution of a completely specified input state to a completely determined output state. The key difficulty with such an approach is that, in general, nonlinear operator equations cannot be simulated by any simple numerical scheme. When the evolution is both in space and time as in our case, the problem becomes one suited only for full-time theorists employing techniques such as the positive-P representation [90, 91]. Fortunately, in our case, although the evolution is nonlinear in the pump fields, it is linear in the weak signal fields. This allows a great simplification if we treat the pump fields as classically evolving parameters in the quantum Heisenberg equations for the weak signals. Using this approach, we solve numerically for the classical evolution of the weak signals and use those solutions to calculate any quantum probability or correlation function concerning the signal fields. Additionally, we can solve numerically for the classical Green functions for the signal evolution, which gives us a complimentary method for calculating quantum quantities as well as a method for checking the accuracy our solution. There are many ways to do this, most of which can be broken up into two main categories of methods; the finite-difference methods and the pseudospectral methods [60]. It happens to be the case that the pseudospectral methods are generally significantly more computationally efficient than the finite-difference methods to compute solutions that are of the same order of accuracy. Among pseudospectral methods the most often used method is the

split-step Fourier method, owing to the efficiency of calculating Fourier transforms via Fast Fourier Transform (FFT) algorithms. The split-step Fourier method is the method used to calculate field evolution in this dissertation.

In this chapter we will briefly describe the split-step Fourier method as it applies to the BS process. Some details concerning how the method is applied, along with the Runge-Kutta ordinary differential equation solving method, will be discussed. Lastly, some numerical results for BS translation and two-color HOMI effects for models of fibers used in this dissertation will be presented. The full code used, written in MATLAB script, is available on request.

5.1. Overview of the Approach: The Split-Step Fourier Method

We desire to numerically solve (4.28), for an arbitrary input boundary condition, written again here for convenience (along with (4.29) as part of the accompanying definition).

$$\partial_z A(T,z) = i\beta(i\partial_T;\Omega_0)A(T,z) + i\gamma|A(T,z)|^2 A(T,z) \tag{5.1}$$

$$\beta(i\partial_T;\Omega_0) = \sum_{n=2}^{\infty} \frac{\beta^{(n)}(\Omega_0)(i\partial_T)^n}{n!} \tag{5.2}$$

Recall that in the formulation of this equation the time variable T is for the retarded frame, where the frame of reference is "boosted" by the group velocity of the field at its central frequency. This formula includes the effects of dispersion, self and cross phase modulation, and four-wave mixing, while ignoring the effects of self-steepening and Raman generation. The self-steepening term can be ignored in this instance because it only meaningfully affects pulses with time widths less than 1 picosecond [60], and the pulse durations used in the experiment will be on the order of 100 picoseconds.

Raman generation can also be ignored since for the power of the pumps and length of fibers used in the experiment the Raman threshold is just barely reached. Also, in the context of studying the BS process, Raman generation simply acts as a noise term, and does not need to be studied in its own right. Loss due to absorption is not included in the model, although it could easily be by simply including a factor of $\alpha/2A(t,z)$ to the right hand side of (5.1).

To prepare (5.1) for numerical solution we write the terms that act on the field on the right hand side as two different operators, one differential operator that accounts for the dispersion as function of frequency and one nonlinear operator that accounts for the nonlinearity as a function of time:

$$\partial_z A(T,z) = (\hat{D} + \hat{N})A(T,z) \tag{5.3}$$

$$\hat{D(\omega)} = \sum_{n=1}^{\infty} \frac{i\beta^{(n)}(\omega)^n}{n!} \tag{5.4}$$

$$\hat{N(T)} = i\gamma|A(T,z)|^2. \tag{5.5}$$

The $i\partial_t$ term in the dispersive term has been replaced with ω, as that is what it corresponds to in the frequency domain where the dispersive term will act on the field. In a real, physical system, dispersion and nonlinearity act on the field at the same time. Analytically, we can think of this as dispersion and nonlinearity acting independently on one infinitesimal fiber segment of length dz at a time until the end of the fiber is reached. The split-step Fourier (SSF) method seeks to approximate this process by breaking up the fiber into N segments, each with length $\Delta z = L/N$. In its simplest form, the SSF method evolves $A(T,z)$ to $A(T,z+\Delta z)$ by the equation

$$A(T,z+\Delta z) \approx \exp(\Delta z\hat{D})\exp(\Delta z\hat{N})A(T,z). \tag{5.6}$$

Before the exponential containing $\hat{N}$ acts on the initial field, the resulting time evolved field must be Fourier transformed to the frequency domain where the exponential containing $\hat{D}$ acts on the half-evolved field in the frequency domain. After that, the field must be inverse Fourier transformed to arrive at the fully evolved field as a function of T.

While the algorithm of (5.6) is the simplest method applying the SSF method, it is not the best. Using the Baker-Hausdorff formula for two non-commuting operators it can be shown that this method is accurate only up to $\mathcal{O}((\Delta z)^2)$. To improve upon this, the symmetric split-step Fourier (SSSF) method can be employed [92] in which the evolution of one step is given by

$$A(T, z + \Delta z) \approx \exp\left(\frac{\Delta z}{2}\hat{D}\right) \exp\left(\int_z^{z+\Delta z} \hat{N} dz\right) \exp\left(\frac{\Delta z}{2}\hat{D}\right) A(T, z). \tag{5.7}$$

Here the nonlinear term is sandwiched between two dispersive half-steps. By using the Baker-Hausdorff formula, it can be shown that the SSSF method is accurate up to $\mathcal{O}((\Delta z)^3)$.

5.1.1. Algorithmic Implementation

To solve (5.1) in the manner described above for pulses that are close in time and frequency requires only one time mesh and the corresponding frequency mesh in which to situate the pulses in relation to one another. While in theory only one time mesh and one frequency mesh are all that is absolutely required for any situation, carrying out such a method for pulses that are distantly spaced in either domain would be computationally prohibitive. In the case for the work presented in this dissertation, the pump pulses and sideband pulses almost completely overlap in time

but are separated by large frequency amounts, which would make using one frequency mesh for all pulses highly impractical. Instead, each field is given its own frequency mesh, allowing for accurate computation of the frequency amplitudes around the fields while not calculating the frequency amplitudes for intervals between the fields, which will be very close to zero anyhow. Because of this, the terms in which the fields are coupled (the nonlinear terms) in (5.1) must be rewritten such that the four fields are described by a system of four coupled equations. Labeling the amplitudes by A_p, A_q, A_i, and A_s (with central carrier frequencies ω_p, ω_q, ω_i, and ω_s, respectively) for the two pumps, idler, and signal, respectively, the total electric field can be written as

$$E(z,t) = \sum_j A_j(z,t)e^{i(\beta_j z - \omega_j t)} + \text{c.c.}, \tag{5.8}$$

where j denotes p, q, i or s. Given that pump p combines with the idler to produce amplitude at pump q and the signal, the four coupled equations, with suppressed amplitude parameters, are given by

$$\begin{aligned}
\partial_z A_p &= i\beta_p(i\partial_T;\omega_p)A_p + \left(i\gamma|A_p|^2 + 2i\gamma\sum_{k\neq p}|A_k|^2\right)A_p + 2i\gamma A_i^* A_q A_s \exp[i\Delta\beta z] \\
\partial_z A_q &= i\beta_p(i\partial_T;\omega_q)A_q + \left(i\gamma|A_q|^2 + 2i\gamma\sum_{k\neq q}|A_k|^2\right)A_q + 2i\gamma A_s^* A_p A_i \exp[-i\Delta\beta z] \\
\partial_z A_i &= i\beta_p(i\partial_T;\omega_i)A_i + \left(i\gamma|A_i|^2 + 2i\gamma\sum_{k\neq i}|A_k|^2\right)A_i + 2i\gamma A_p^* A_q A_s \exp[i\Delta\beta z] \\
\partial_z A_s &= i\beta_p(i\partial_T;\omega_s)A_s + \left(i\gamma|A_s|^2 + 2i\gamma\sum_{k\neq s}|A_k|^2\right)A_s + 2i\gamma A_q^* A_p A_i \exp[-i\Delta\beta z],
\end{aligned} \tag{5.9}$$

where $\Delta\beta$ is the dispersive mismatch given by (4.58) between the fields. The first term on the right hand side describes the effect of dispersion, the next two terms describe self and cross phase modulation respectively, and the last term describes the BS four-wave mixing process. The quantity $\beta_j(i\partial_T;\Omega_0)$ is given by

$$\beta_j(i\partial_T;\Omega_0) = \sum_{n=1}^{\infty} \frac{\beta^{(n)}(\Omega_0)(i\partial_T)^n}{n!} - \beta^{(1)}(\omega_j)i\partial_T. \tag{5.10}$$

where $\beta^{(n)}(\Omega_0)$ is the nth derivative of β evaluated at Ω_0, and $T = t - z\beta^{(1)}(\omega_j)$. Essentially, the equation for A_i is being solved in the frame of the A_j field. For the equations of (5.9), the frame of reference is the pump field p, although it could be for any of the pulses or even at a frequency not associated with a field, like the average frequency of all fields. The equations were chosen to be in the frame of one of the pumps because the temporal amplitude for Gaussian pulses (as the pumps are assumed to be) under self and cross phase modulation is constant. Hence for the pump that defines the frame of reference, the amplitude will not change in shape or place in time, whereas for the other pump it will not change shape but will move relative to it's initial T offset of zero. This allows for a quick visual check to see that the code is working properly.

Given this new set of equations, the algorithm for calculating the evolution of the fields, in brief, is as follows. After the wavelengths and powers of the two pumps and temporal durations of the pumps and the idler are given, the central frequency of the idler and signal are found given a particular fiber dispersion. For the given central frequencies the dispersion mesh as a function of frequency is calculated for each field. Then the amplitudes for the four fields are created in the time domain. This consists of the absolute value of the amplitudes created in regards to the retarded time

mesh T_a, with time separation between mesh points of Δt initially centered at zero (although that can be changed if an offset value is desired), for all fields. Although the initial amplitude shape is in theory arbitrary, we choose all input shapes to be either transform-limited Gaussian pulses or CW fields. These shapes closely correspond to the output of most mode-locked pulsed or monochromatic lasers, respectively, including the lasers used in the experiments. When using transform-limited Gaussian pulses with time standard deviation σ_t and frequency standard deviation $\sigma_f = 1/\sigma_t$, where the separation in frequency mesh points Δf is equal to $1/T$, the inverse of the time window, there is the question of how many mesh points N to use for given T and σ_t values. It is desirable to treat the time and frequency domains on equal footing, since they are equally important to the solution of the equations. One way in which to define equal treatment is to choose the parameters so that an equal number of mesh points represent the Gaussian time distribution and the Gaussian frequency distribution. For parameters that give the same number of mesh points contained within one σ_t in time and one σ_f in frequency away from the peak Gaussian value in the center of each respective mesh, it is easy to show that $N = T^2/\sigma_t^2$. For all calculations involving Gaussian pulses, this convention is used.

The initial idler power is set to a factor of 10^{-5} times that of the lower pump power to ensure that the sidebands have no meaningful effect on the pumps. These initial amplitudes are then Fourier transformed via MATLAB's built in FFT functions to frequency space.[1] The fields are now ready to be advanced one step. First, a dispersive half-step is applied to the fields, simply by multiplying the fields by an exponential factor of the dispersive mesh. The fields are then transformed into the

[1]For best results in MATLAB it is suggested to perform the Fourier transform on a vector A via the sequence $A(\omega)$ =fftshift(fft(fftshift($A(t)$))), instead of just fft(A(t)). This has to do with how the phase is calculated, often not an important quantity for regular uses of an fft, but an important one in this circumstance. For Fourier transforming back, use $A(t)$ =ifftshift(ifft(ifftshift($A(\omega)$))).

time domain where the phase modulation and four-wave mixing terms act on the fields. Details regarding the implementation of the four-wave mixing calculation are given in the next subsection. Since the sideband fields are so much weaker than the pump fields, the four-wave mixing term affecting the two pump fields is negligible, and is not included in the calculation. Then, using the inverse Fourier transform, the fields are transformed into the frequency domain where the second dispersive half-step is acted on them. This evolutionary procedure is carried out until the fields have been propagated down the entire length of the fiber.

After the calculation has been completed, there is the question of how accurate the numerical solution is to the true solution. There are a few ways in which to gauge the accuracy of the numerical solutions. While not explicitly built into the calculations, for all calculations the frequency integrated amplitude squared of the idler and signal were verified to be conserved, in accordance with the Manley-Rowe relation [72] for the BS process. Also, there are conditions on the unitary of the Green functions that governs the process, given by (4.74) and (4.75). Although checking these conditions is significantly more expensive computationally than verifying the Manley-Rowe conditions, and therefore is not feasible to carry out for every case for a study requiring a large number of case like in the below-mentioned parameter studies, this check can be carried out for several representative cases for such studies. The Green functions were calculated in the mode basis, where the input and output field amplitudes were decomposed into Hermite-Gaussian functions. The Green function for a particular case was found by setting the idler and signal field to the first through N^{th} order of Hermite-Gaussian functions (where N was sufficiently large to describe the resulting output fields) and comparing these input amplitudes to the output amplitudes. The Green functions were then checked against (4.74) and (4.75), and

in these cases were found to agree to good approximation. Finally, the appropriate number of steps were taken for each calculation so that the solutions converged and were not meaningfully dependent on the exact number of steps.

5.1.2. Runge-Kutta Integration Methods

Equation (5.7), which gives the numerical recipe for evolving the field, contains an integration of the nonlinear term. Computing this integral is a nontrivial operation, and there are several methods available to tackle this problem. Probably the most widely used method for general ordinary differential equation and integration problems is the Runge-Kutta (RK) method, which will be the method used in this dissertation. The RK method is really a family of methods, depending on what type of problem one is solving and the order of accuracy required. We present here a short introduction to RK methods, details of which can be found in many numerical techniques books such as [93] and [94].

The most straight forward integration problem to solve, one that thankfully corresponds to the BS process, is the first-order differential equation with initial boundary conditions. If y is the dependent variable and z the independent variable then this problem can be summarized as

$$d_z y = f(z, y) \ , \ y(z_0) = y_0. \tag{5.11}$$

To numerically solve this, the variables must be discretized in a mesh index with mesh points labeled according to n. Hence, $y(z) \to y_n(z_n)$ with step size Δz. The easiest way in which to advance y_n to y_{n+1} (from z_n to z_{n+1}) is through the use of the Euler

method:

$$y_{n+1} = y_n + \Delta z f(z_n, y_n). \tag{5.12}$$

This method is simple but crude, and only accurate to $\mathcal{O}((\Delta z)^2)$. This is due to the fact that the method only uses derivative information (in the form of $\Delta z f(z_n, y_n)$) at step index n. The Euler method is rarely used for practical problems.

To get a more accurate solution we want to access more information about the function $f(z, y)$. So instead of just using derivative information at the beginning we shall make an educated guess of what the value of y should be midway through the step, a "trial" midpoint. With that information we can approximate what the midpoint derivative should be and use that to better guess what the full step solution should be. Mathematically this can be implemented as

$$\begin{aligned} k_1 &= \Delta z f(z_n, y_n) \\ k_2 &= \Delta z f(z_n + \Delta z/2, y_n + k_1/2) \\ y_{n+1} &= y_n + k_2. \end{aligned} \tag{5.13}$$

Because of the extra information, and extra step, this second-order RK method (also, called the midpoint method) is accurate up to $\mathcal{O}((\Delta z)^3)$.

Although a significant improvement over the Euler method, the midpoint method is not the go-to numerical recipe favored by most practitioners. The fourth-order RK method is often simply referred to as *the* Runge-Kutta method, due to its frequent use over all other orders RK methods. In it, four trial derivative points are accessed; the usual Euler point, two midpoints (for different guesses of what the midpoint should

be), and one trial point at the full step. Mathematically this is implemented as

$$\begin{aligned} k_1 &= \Delta z f(z_n, y_n) \\ k_2 &= \Delta z f(z_n + \Delta z/2, y_n + k_1/2) \\ k_3 &= \Delta z f(z_n + \Delta z/2, y_n + k_2/2) \\ k_4 &= \Delta z f(z_n + \Delta z, y_n + k_3) \\ y_{n+1} &= y_n + k_1/6 + k_2/3 + k_3/3 + k_4/6. \end{aligned} \tag{5.14}$$

This can be shown to be accurate up to $\mathcal{O}((\Delta z)^5)$. While there are some situations in which it is appropriate to use the second-order method over the fourth-order method, for functions that are relatively "smooth", i.e. the value of the function from step to step does not change drastically, the fourth-order RK method will be more accurate. Since we are not concerned with ultrafast pulses in this dissertation, which might have amplitude shapes that do not conform to the definition of "smooth", the use of the fourth-order RK method to solve the pulse-propagation equations is most appropriate. It is possible to develop higher-order schemes than fourth, and add bells and whistles to the algorithm such as adaptive step size, but as will shortly be shown, the fourth-order RK method more than suffices for solving the pulse evolution problem.

In the four-wave mixing BS context we can see how the variables of (5.14) match up with those of (5.9). The main difference is that (5.9) describes four coupled equations, whereas (5.14) is considering a single equation, although only the signal and idler fields are coupled via BS, so it is more accurate to describe the system as two coupled equations. The signal and idler fields each correspond to a y variable when it is being evolved while the other fields are part of $f(z_n, y_n)$ terms. Hence signal

and idler fields go through their own RK process, but the solution to one informs the solution of the other in an iterative manner. The trial midpoints are evaluated by using the "actual" pump midpoint values and approximating the other sideband value via the k_2 and k_3 terms used in that sideband's evolution.

5.2. Numerical Results for Translation and Two-Color HOMI

To show an example of the techniques for evolving the field as it travels down the fiber, we present the results of a few calculations aimed at exploring some of the important properties of the BS process. Exploration of this manner is by its nature only able to offer limited understanding; it is notoriously difficult to gain general insight from solutions to very specific initial conditions and problem parameters. However, some very general features of how the BS process functions are accessible through these methods. In particular we will try to explore the effect of input idler/signal pulse length, pump pulse length, and pump power on the overall translation efficiency. Also, we explore the two-color HOMI effect to discover the conditions in which the effect can be shown.

Since we are considering numerical solutions we must not only choose specific initial conditions but also specific fiber parameters, namely the dispersion function. As will be explained in the next chapter, a dispersion function for the fiber used in the experiment for the BS process was experimentally attained. For the experimental input pulse wavelengths of 808 and 845 nm, the derived dispersion function yields idler and signal values of 673 nm and 649 nm respectively. The actual values from the experiment were 683 nm and 659 nm respectively, so the predicted values are both about one and a half percent off. This error can be explained in part by the BS process' sensitivity to a fiber's ZDW. Since the ZDW for co-polarized fields is nearly

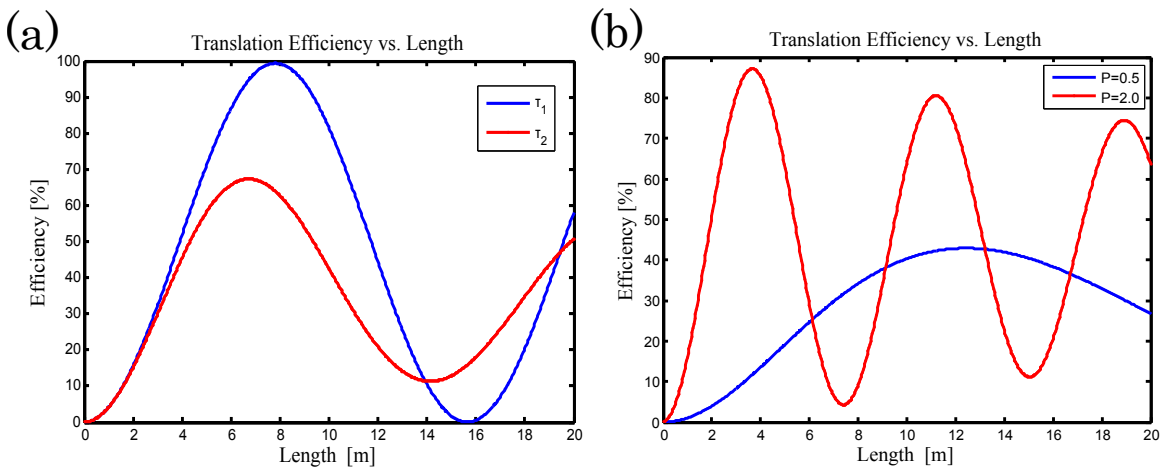

FIGURE 5.1. Translation efficiency results for differing input idler pulse widths with CW pumps versus fiber length. (a) The translation efficiency versus fiber length is shown for input idler pulses with two different temporal FWHM values. The blue line (τ_1) relates to a pulse with a FWHM of 50 ps and the red line (τ_2) relates to a pulse with a FWHM of 5 ps. (b) The translation efficiency versus fiber length for two equal 0.5 ps pulses that are associated with two sets of pump power values. The blue is associated with pump values of 0.5 W while the red is associated with pump values of 2.0 W.

the center of energy for the BS process (the average single photon energy $\hbar\nu$ of all fields), for large wavelength separations of tens of nm or more between the pump and sidebands relative to the ZDW, a 1 nm change in the fiber's ZDW will result in an approximately 2 nm change in the sideband wavelengths. Hence a 1.5 percent error in the predicted sideband wavelength suggests an error in the calculated ZDW of about 0.75 percent. This suggests that the predicted dispersion function only deviates from the actual dispersion function by one percent or less. Therefore, even though there are discrepancies in the predicted and actual values of some parameters, which there are bound to be in any measurement, quantities depending on fiber dispersion, such as field outputs, are likely to be very similar to the actual quantities in the real fiber.

5.2.1. Frequency Translation

To begin exploring the BS process we choose the pumps to be monochromatic CW fields, which is accomplished numerically by initially choosing the pump amplitude function to be a constant in time. As stated before, all non-CW input fields were chosen to be transform-limited Gaussian pulses in time and frequency. To study the efficiency of the translation effect, of the sidebands only the idler field was given non-zero amplitude. This makes it natural to define the translation efficiency as the percentage of the idler amplitude that is translated from the idler field to the signal field. Figure 5.1.(a) shows the translation efficiency as a function of fiber length for two different input full width at half maximum (FWHM) idler temporal widths. The first width, τ_1, had a value of 50 ps, while the second width, τ_2, had a value of 5 ps. Both pumps had powers of one watt. As can be seen in the figure, the τ_1 idler field is essentially completely converted to the signal field and then, at about twice that length, is re-converted to the idler field. This conforms to the sinusoidal nature of the BS process, described by (4.55) and (4.56), for CW fields. Here even, though the input idler field is pulsed, it is temporally long enough (really, spectrally thin enough), and the dispersion is flat enough, that the idler field is quasi-CW. The idler field with longer width τ_2 only partially converts and doesn't fully re-convert farther down the fiber. The difference is likely due to the fiber dispersion mismatch $\Delta\beta_{BS}$ in (5.15), repeated here

$$\kappa_{BS} = (1/4[\Delta\beta_{BS} + \gamma(P_2 - P_1)]^2 + 4\gamma^2 P_1 P_2)^{1/2}, \tag{5.15}$$

becoming too large for different spectral parts of the signal to be effectively translated. Although any frequency mismatch leads to incomplete conversion, the pulse with

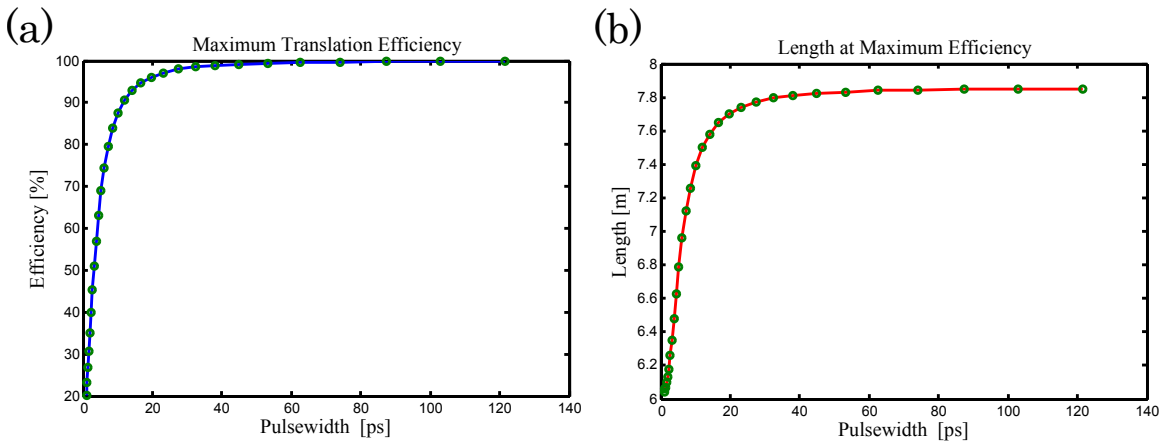

FIGURE 5.2. Translation efficiency results for differing input idler pulse widths with CW pumps. The green dots represent cases that were actually calculated, while the connecting lines between them only serve as a visual reference. (a) The maximal translation efficiency achieved versus FWHM pulse duration with both pump powers equal to 1 W. (b) The length at which maximal efficiency is achieved versus pulse width.

width τ_1 has such a small mismatch that it is nearly fully converted. In some sense, the pulse with width τ_2 field has a larger spectral bandwidth than the BS process at these pump powers and fiber length. Also, the lengths at which maximum conversion and re-conversion happen are shorter for τ_2 than for τ_1. This is also due to the large dispersive mismatch some spectral components of the τ_2 field had. As shown in (4.55) and (4.56), the argument of the sinusoidal term is $\kappa_{BS}z$, where the larger the dispersive mismatch, the larger κ_{BS} will be. Hence the more mismatch a field has the shorter the fiber needs to be for the sinusoidal term to reach its maximum value. The case in which the input idler field is CW has the smallest possible dispersive mismatch, and will therefore take the longest to convert and re-convert.

This is explored to a fuller extent in Figure 5.2.. Here the input idler temporal width was varied from over a 100 ps down to 1 ps. As can be clearly seen in part (a), the maximum translation efficiency achieved is nearly 100 percent for pulses of duration about 50 ps or longer, but under about 20 ps the efficiency drops

precipitously until at 1 ps it reaches around 20 percent and looks like shorter pulses would quickly reach nearly zero efficiency. The length at which maximum translation efficiency occurs, shown in part (b), also drops monotonically but seems to settle at a particular length which is not much more than 20 percent different from that of pulses with high translation efficiency. This suggests that for this fiber and power level the BS process simply cannot translate the outer spectral wings of the short pulses and has converted all it could in this short range of lengths.

The values of the pump powers plays an equally interesting role in the BS process. Figure 5.2.(b) shows the translation efficiency versus length for the propagation of a 5 ps pulse where the two sets of pump powers are equal to 0.5 and 2.0 watts. What is interesting is that not only does the pulse with higher pump powers achieve higher efficiency, but it does so at a significantly shorter length. The first phenomenon of higher translation efficiency can be understood by noting that the value of κ_{BS} for the case of the pulse with high powered pumps depends less on the values of the dispersive mismatch than it does on the powers of the pulse. Because of that, the term multiplying the sinusoidal term of (4.55) and (4.56) can reach a higher value. The second phenomenon of achieving the maximal value for efficiency can be understood by noting that although the pulses have an equal amount of dispersive mismatch, the absolute value of κ_{BS} is around four times larger for the pulse with high powered pumps, so the sinusoidal terms of (4.55) and (4.56) should reach their maximum in about a quarter of the length.

Until now we have explored examples in which the two pump powers are equal. Figure 5.3. shows the case for the propagation of 50 ps pulse where the pump powers are not equal but still multiply together to get 1 W^2. The x axis for both parts is the power of Pump one. As is clear from κ_{BS}, there is a term that depends on

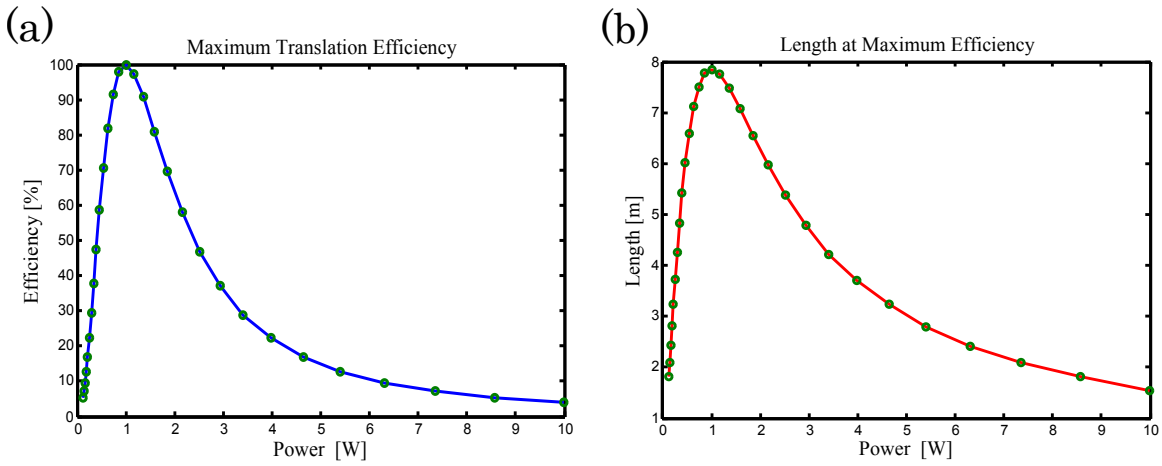

FIGURE 5.3. The role of pump power mismatch in the translation process with CW pumps. The green dots represent cases that were actually calculated, while the connecting lines between them only serve as a visual reference. (a) The maximal translation efficiency achieved versus Pump-one power, where $P_1 \cdot P_2 = 1\text{W}^2$ for all values of Pump one power. (b) The length at which maximal efficiency is achieved versus Pump-one power.

the subtracted value of the powers, which up until now has been zero. This term, if large enough, will cause the multiplicative term in (4.55) and (4.56) to decrease away from one, which is exactly what happens. For small or large values of Pump one the efficiency drops dramatically. Note that the equations are not symmetric in power; κ_{BS} will take on somewhat different values if Pump one and Pump two are switched. This can be seen in both parts (a) and (b) (particularly b) where the values of the efficiency and length for Pump one values of 0.1 W and 10 W are not equal. The differences in the lengths it takes to achieve maximum efficiency can be explained in the usual manner that since the value of κ_{BS} changes the length at which the sinusoids of (4.55) and (4.56) achieve their maximums will change.

For the cases in which the pumps are CW it is relatively straightforward to understand the numerical solutions. The more realistic cases, at least for experimental work presented in this dissertation, when the pumps are pulsed,

interpreting the solutions can be much trickier. With pulsed pumps there are issues with pump/sideband walk-off that make teasing out which effects are due to the dynamic pump pulses and which are due the fiber properties difficult. In addition, there are no longer relatively simple equations such as (4.55) and (4.56) to fully guide the interpretation, although the CW equations can still give some insight.

The parameter space also becomes much larger, as there are both pump pulse widths and sideband pulse widths to account for. Figures 5.4. and 5.5. give the input (blue) and output (red) amplitude squared in both time and frequency space for two particular scenarios evolved over the typical 20 meters, with all input pulses being Gaussian. In both figures the pump pulses had equal widths and powers, and the input and output pump amplitudes are normalized to the peak values of the input pump pulses, while the input and output sideband amplitudes are normalized to the peak value of the input idler amplitude. All time amplitude plots are taken in the frame of Pump one.

In Figure 5.4., the FWHM pump pulse widths were equal to 200 ps and the input idler pulse width was 50 ps. The peak power of the pumps was 1 watt. Since the frame of reference is the Pump one, it is not surprising to see that the shape of the amplitude distribution doesn't change in time, since the only nonlinear effects acting on the pumps are self and cross phase modulation. The Pump two shape is constant but shifted slightly, reflecting the fact that the pumps travel at different group velocities. In the frequency domain, the initial Gaussian shape for the pumps is distorted by phase modulation. The slight asymmetry is due to the differing speeds of the pumps. For the sidebands, in both time and frequency space, the general Gaussian nature of the idler is kept but diminished in overall amplitude, while the signal grows from nothing into a fairly Gaussian pulse. The sideband fields don't

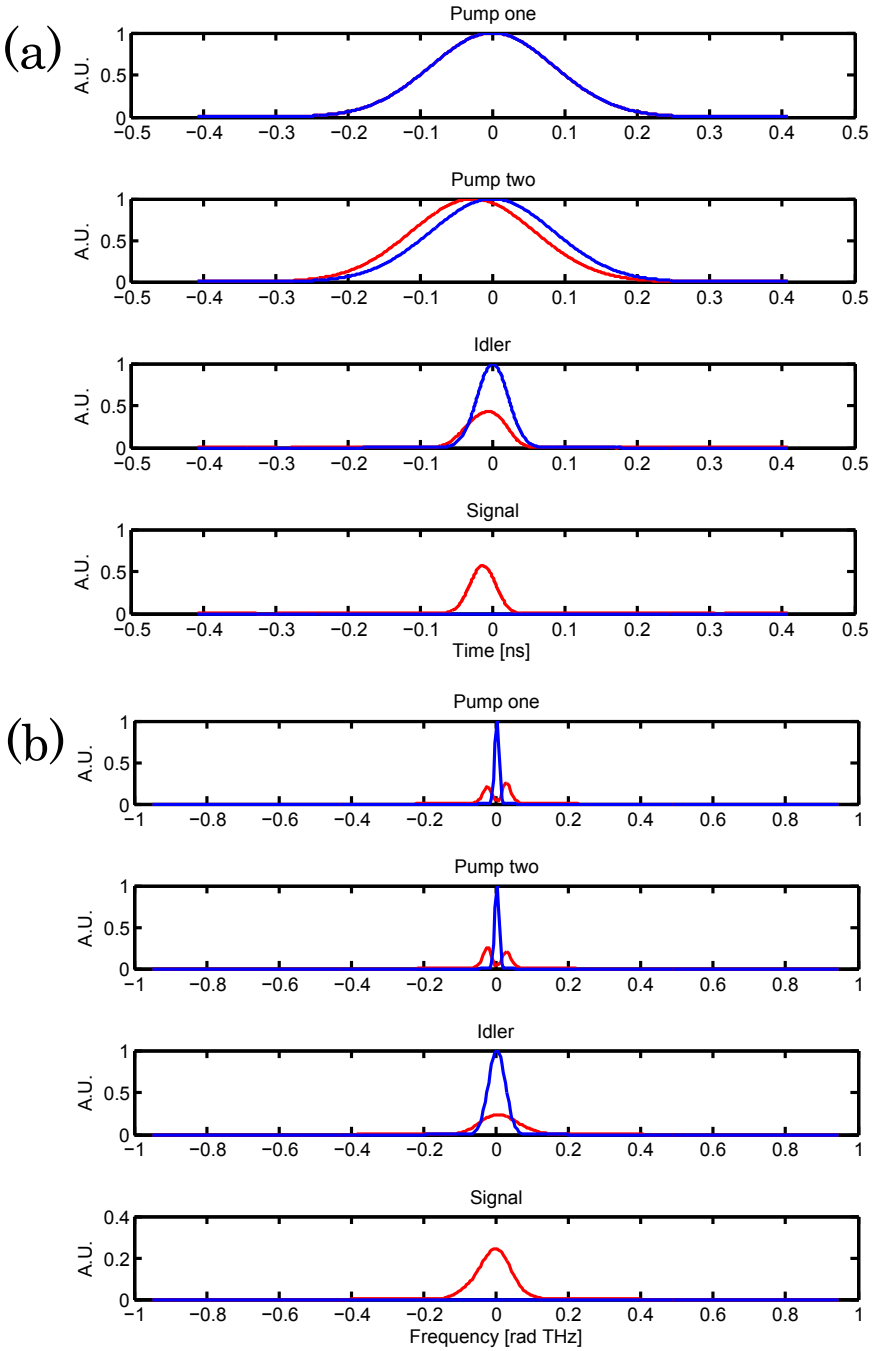

FIGURE 5.4. Input and output amplitudes for pulsed BS; case one. (a) The pump and sideband amplitude squared in the temporal domain. Blue indicates input and red indicates output. In this case, the FWHM of the pumps was 200 ps, while the idler input was 50 ps. The pump peak powers are equal. The pump amplitudes are normalized to the input pump peak powers of 1 watt. The sideband amplitudes are normalized with respect to the peak input power of the idler. (b) The pump and sideband amplitude squared in the frequency domain. The normalization conventions are the same as that in part (a).

experience meaningful phase modulation from the sideband fields, since only the pumps have large enough power to affect any meaningful phase modulation.

In Figure 5.5., the pump pulses' FWHM are changed to be $200/8 \cong 25$ps while the pulse energies remain the same as in Figure 5.4.. The input idler pulse width is still 50 ps. Although the pump group velocities are the same as in Figure 5.4., since their temporal widths are significantly smaller, the shift of pump two is much more dramatic. Also, with higher peak power, the pump spectra are much more affected by self and cross phase modulation. These factors conspire to produce very non-Gaussian shapes for the sideband output. While phase modulation due to the pumps is felt more acutely by the sidebands, it is also the case that the idler is twice as long as the pump pulses, and so different parts of the sidebands are affected by the pumps as the pumps pass through the sidebands.

These are of course only two specific cases, and they are not much help in providing a general understanding of non-CW scenarios. As a more general example, Figure 5.6. shows the results for the maximum translation efficiency and the length at which this maximum occurs versus the ratio of the input sideband pulse width to the pump pulse width for a constant sideband FWHM pulse width of 100 ps. To better explore the effect of the pump pulse width on the process, the total energy of each pump pulse was held fixed with the peak power for a pump pulse width of 100 ps being 2 W. Therefore the longer pulses would have lower peak powers than the shorter pulses. Also, the two pump fields had equal temporal shapes, and therefore equal peak powers. As is shown in part (a), for long pump pulses, where σ_i/σ_p values are small, the translation efficiency is nearly 100 percent, and for short pump pulses the translation efficiency is low. This intuitively makes sense; the long pulses are quasi-CW as far as the sideband pulse is concerned and there is adequate power to

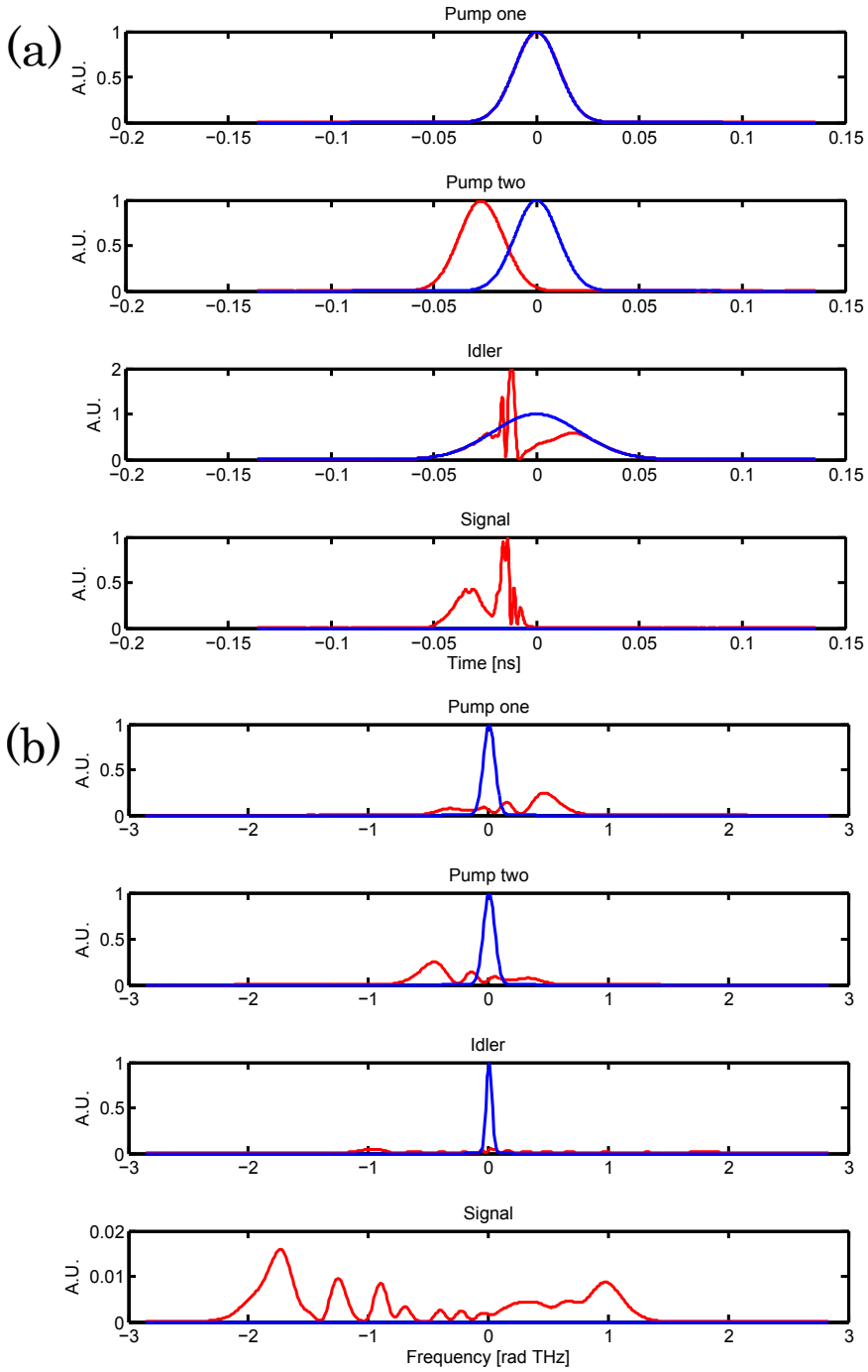

FIGURE 5.5. Input and output amplitudes for pulsed BS; case two. (a) The pump and sideband amplitude squared in the temporal domain. Blue indicates input and red indicates output. In this case, the FWHM of the pumps was 25 ps, while the idler input was 50 ps. The pump peak powers are equal, and the pump pulses are set to have the same energy as they did in Figure 5.4.. The sideband amplitudes are normalized with respect to the peak input power of the idler. (b) The pump and sideband amplitude squared in the frequency domain. The normalization conventions are the same as that in part (a).

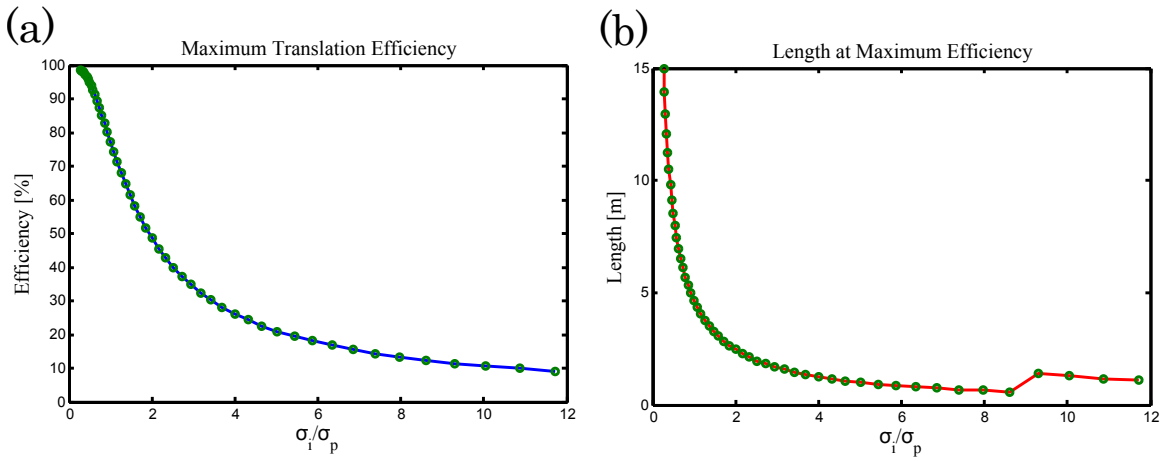

FIGURE 5.6. Translation efficiency for pulsed pumps. The green dots represent cases that were actually calculated, while the connecting lines between them only serve as a visual reference. (a) Maximal translation efficiency achieved versus the ratio of the input sideband pulse width to the pump pulse width. The sideband pulse width was constant at 100 ps, and the total pump pulse energy was held constant (the pumps were equal in power). (b) The length at which the maximal translation efficiency was achieved. The small deviation from the curve for high σ_i/σ_p values is not a numerical artifact and is related to the "ringing" effect discussed below.

accomplish significant translation, whereas for short pump pulses most of the pump pulse doesn't interact with the sideband pulse and only a fraction of the sideband pulse has a chance to be translated. This agrees with the data in part (b), which show that the long pump pulses need a long interaction length to achieve the maximal translation because of their relatively weak power whereas the short pulses that have large peak power achieve maximal translation efficiency very early on in the fiber.

5.2.2. Two-Color Hong-Ou-Mandel Interference

The evolution of the amplitude spectrum in the calculations discussed above could either be interpreted as the evolution of the quantum state, where each frequency/time component is represented by a creation operator, or as the evolution of a classical electromagnetic wave. But not all BS effects are classical; the HOMI

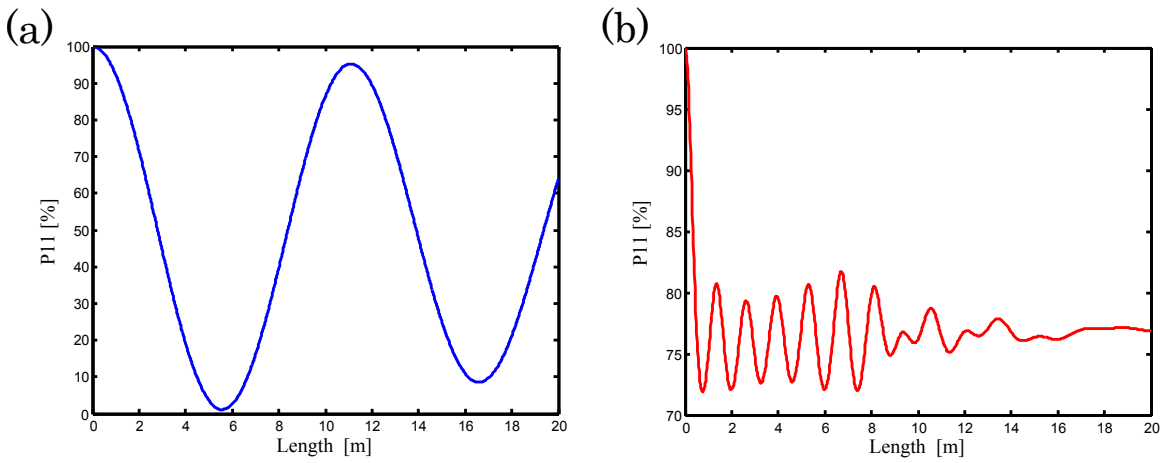

FIGURE 5.7. Two-photon Coincidence probability P11 versus length for two cases. (a) The FWHM of the pump pulses were 270 ps long while the signal and idler were 100 ps. The peak power of the pumps was equal to 3.2 watts. (b) The FWHM of the pump pulses were 16 ps long while the signal and idler were still 100 ps. The pump powers were equal and set to a value that kept the pulse energy the same as that in part (a).

effect discussed in Chapter IV is a decidedly non-classical effect, where the two-photon state can be described as

$$\psi\rangle = C_{11}|1,1\rangle + C_{20}|2,0\rangle + C_{02}|0,2\rangle, \tag{5.16}$$

with $|i,j\rangle$ being the state where i photons are output in the idler mode and j photons are output in the signal mode. It is interesting to note that quantum quantities such as the C coefficients can be discovered through classical simulation, and here we give a few examples of that occurrence. Figure 5.7. shows two cases in which the probability $P11 = |C_{11}|^2$ was calculated, as derived from (4.82), as a function of length down the fiber. In part (a), the pump pulse FWHMs were 270 ps and had equal peak powers of 3.2 watts. The input sidebands had pulsewidths of 100 ps. Since the pump pulses are so much longer than the sidebands, the pumps appear to be quasi-CW to the sidebands. Significant translation occurs, making the value of $P11$ drop near zero

(when around 50 percent translation occurs) and then shoot back up to nearly 100 percent (when nearly 100 percent translation occurs). In the second case shown in part (b), the pump pulsewidth was 16 ps while the sideband pulsewidth was still 100 ps. The energy of each pump pulse was the same as it was in part (a). Since the peak powers were significantly higher, the translation occurred much quicker, hence the rapid drop in $P11$. But since the pump pulses were much shorter in time than the sideband pulses, only a minority of the sideband pulses could be translated, leading to $P11$ staying relatively large. Also, part (b) shows the "ringing" effect, where the probability amplitude oscillates rapidly with small deviation around a central value and finally settles down to that value.

To get a more general understanding of the HOMI phenomenon, we turn to a parameter study, like was done for frequency translation above. Figure 5.8. shows the most important results of a calculation in which $P11$ was calculated for the range of parameters used in the "classical" pulsed-pump calculation shown in Figure 5.6.. Although the $P20$ and $P02$ values are not given here, derived from equation (4.85), it was shown that $P11 + P20 + P02 = 1$ to numerical accuracy, and that the $P20$ and $P02$ values were nearly identical over the range of parameters. As previously discussed, the cases that are most non-classical are those in which the value of $P11$ is the least (and $P20 + P02$ is the highest), which was the reason $P11$ was chosen to be the variable that represents the calculation and was plotted.

As can be seen in part (a), the long pump pulses, where σ_i/σ_p is small, are associated with small minimum values of $P11$. The most extreme of these cases would be essentially equivalent to the case in which the pumps were CW. Conversely, the cases in which the pump pulse width was short see high values for $P11$. These findings make sense in light of the results shown in Figure 5.6. (a), where the long

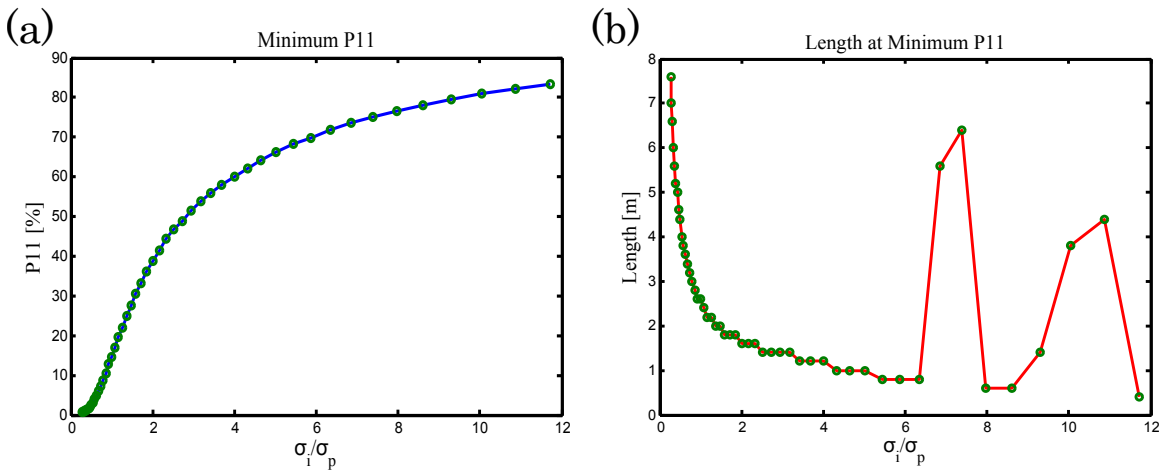

FIGURE 5.8. Two-photon coincidence probability P11 parameter study with pulsed pumps. The green dots represent cases that were actually calculated, while the connecting lines between them only serve as a visual reference. (a) The minimum value of P11 as a function of sideband to pulse FWHM temporal width. (b) The length at which the minimum value of P11 was attained. The "jumps" in the value are not numerical artifacts, and are caused by ringing oscillation in the probability amplitude.

pump pulses corresponded with high translation efficiency and short pump pulses with low translation efficiency. For the cases in which a high degree of translation occurs, at some point the translation efficiency would be around 50 percent, where HOMI is optimal, especially for the CW case. Looking at part (b) it is clear that in general the pulse pump width is proportional to the length at which a minimal value of $P11$ occurs. This makes sense in that the shorter pulses have higher peak power and overlap with the input pulses less, so the part of the input sideband pulse that can be translated are translated sooner in the fiber. The seemingly discontinuous nature of the plot of part (b) is not a numerical artifact; that phenomenon was reproduced for smaller step sizes. For these cases the translation occurs at short fiber lengths but there is ringing oscillation of the probability amplitudes, and for these cases a slightly lower minimum $P11$ value occurs farther on down the fiber. For most intents and purposes, $P11$ takes the smallest value at short distances in the fiber.

It is meaningful to note where exactly the difference between the quantum HOMI effect and its classical correspondence occurs. Imagine a scenario in which two detectors are monitoring the signal and idler output from a fiber that is inducing the BS translation process to occur with 50 percent efficiency. If one classical signal pulse and one classical idler pulse is input into the fiber then the value for $g^{(2)}(0)$, averaged over uniformly random phases for the input sidebands, will be at minimum 0.5. The HOMI effect occurs when this value drops below that 0.5 value, which corresponds to a below 50 percent probability for the state to be in the $|1,1\rangle$ state. As is shown in part (a), this occurs for values of σ_i/σ_p that are at about 3 and below for this particular system. Interestingly, the value of σ_i/σ_p that marks the boundary between being a distinguishingly quantum HOMI effect versus a classical interference effect does not correspond to the case of 50 percent maximum translation. This is because 50 percent translation enables the "strongest" HOMI response, where $P11$ goes to zero. In actuality, all that is needed to demonstrate the HOMI effect is an effective translation efficiency that is meaningfully less than 50 percent (about 35 percent in this case). Also, it is an important to note that the modeling predicts the HOMI effect can be observed when the pumps and sidebands have equal duration, as this case is straightforward to implement experimentally.

CHAPTER VI

THE EXPERIMENTAL APPARATUSES

While this dissertation is concerned mainly with the creation and frequency translation of light on a quantum level, only the frequency translation was experimentally demonstrated [84]. The theoretical work on the production of bi-photon states, as described in Chapter IV, was carried out with collaborators, some of whom performed the experimental work, producing states that had varying degrees entanglement/correlation [15, 16]. The experimental work expounded upon here on quantum frequency translation compliments the work on state creation in that it was necessary to first create a quantum state of light to translate, and the method used was MI in birefringent PCF. The light translated was quantum in the sense that it was mostly composed of single, indivisible photons, a concept not present in classical theory. As noted in an early chapter, the single-photon nature of a field can be experimentally determined by performing a second-order correlation measurement, or $g^{(2)}$ measurement, on the field. In our work, that measurement was performed on the translated and untranslated fields, and they were shown to contain single photons, as will be explained in detail in this chapter. This measurement, along with a determination of the efficiency of the translation process, are the main results of our work, and this chapter details all the experimental equipment necessary to see the quantum frequency translation effect. Also described is a classical frequency translation showing record wavelength/frequency translation and in a new system, birefringent fiber.

6.1. The Quantum Translation Experimental Apparatus

6.1.1. Layout, Lasers and Optical Hardware

The experimental apparatus used to demonstrate quantum frequency translation is shown in Figure 6.1.. In order to produce the frequency translation effect, quantum or classical, in a $\chi^{(3)}$ medium such as fused silica it is necessary to input three fields: two strong pump fields that serve to drive the process and one weak signal field to be translated. The first pump, called Pump one, was a tunable commercial titanium-sapphire laser (Time-Bandwidth, Tiger-ps series) that operating at a central wavelength of 808 nm. It output pulses that were around 100 ps in duration and polarized horizontally (parallel with respect to the optical table). This laser employed a SESAM end mirror [95] with two seemingly (as determined from reflection vs. wavelength measurements) uncoated, solid etalons of thicknesses 1.5 mm and 0.1 mm to achieve passive modelocking. Coarse-grained wavelength tuning was achieved through rotation of a birefringent filter, while fine-tuning was accomplished through small rotations of the etalons with respect to the interior cavity beam. The second pump, called Pump two, was a home-built titanium-sapphire laser operating at central wavelength of 845-nm. It was modeled on the Tiger laser design and also employed a SESAM and etalons for modelocking while relying on a birefringent filter and the etalons for wavelength tuning. Details of the cavity design for the home-built pump can be found in Appendix . Both lasers had repetition rates of 76 MHz and their pulse trains were synchronized by use of a custom-made phase-lock loop (PLL) built by Cliff Dax of the University of Oregon Electronics Shop. The signals used by the PLL were obtained by picking off a small amount of the beam from both pumps and detecting them with photodiodes (DET210 and DET110, Thorlabs) that had rise

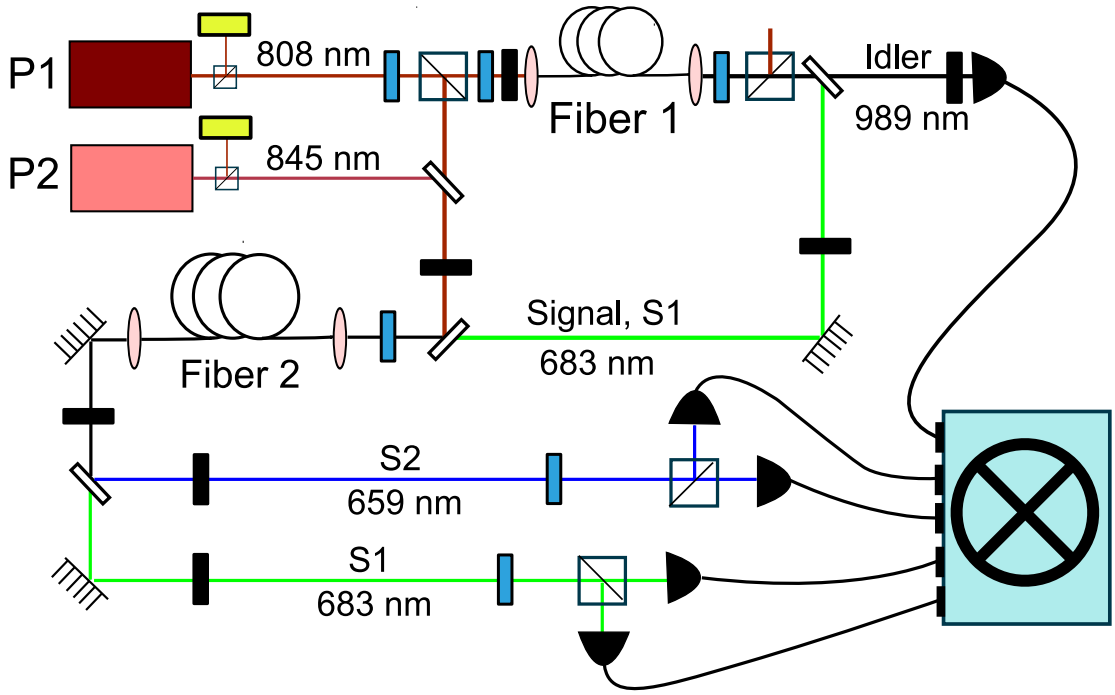

FIGURE 6.1. Diagram of the setup used to create and frequency translate single-photon states. Both pumps (P1 and P2) are 100 ps titanium-sapphire lasers. A single photon is created in Fiber one at 683-nm, heralded, and combined with P1 and P2 to be translated to 659-nm in Fiber two. Four detectors measure $g^{(2)}(0)$ of both 683-nm and 659-nm channels. Small black rectangles represent either longpass or bandpass filters, and transparent rectangles signify dichroic mirrors. The blue rectangles represent have-wave plates and the yellow ones represent photodiodes.

times less than that of the cavity round trip time. Both lasers outputs were filtered with a long-pass filter (FEL0800, Thorlabs) to extinguish any amplified stimulated-emission at the signal and idler wavelengths before being coupled into the fiber used for translation.

The signal to be translated was generated through the birefringent MI effect in fiber having two optical axes.[14, 96] This was accomplished by splitting off a small percentage of Pump one, passing that beam through a longpass filter (FEL0800, Thorlabs) and sending the resulting beam to 32 meters of a custom-made solid-core photonic crystal fiber (PCF), Fiber one, using a half-wave plate (HWP, 10RP42-3,

Newport) to align the beam on the correct optical axis. Fiber one was designed by our collaborators, the Radic group at UCSD, and manufactured by Crystal Fibre. The object lens used for coupling (M-40X, Newport) in had a magnification of 40x and the objective used for coupling the beam (M-20X, Newport) out had a magnification of 20x. The stage used for coupling was a single-mode fiber coupling stage (F-915, Newport). The fiber characteristics are described in more detail below. Through the MI process where two pump photons were annihilated, two sideband photons were created at centered around 683-nm and 989-nm as pictured in Figure 6.2.(a). The frequency difference between the pump and sidebands was $\Delta\omega_{MI} = 4.3 \times 10^{14}$ rad Hz. The pump input power was chosen such that on average each pulse would create significantly less than one photon pair per pump pulse. The output of the fiber was sent through a HWP and polarizing beam splitter (PBS202, Thorlabs) to reject a significant portion of the pump and then split with a dichroic mirror (DM, 669-Di01, Semrock), with the 989-nm idler being sent first through a bandpass filter (FB990-10, Thorlabs) and then to a multimode fiber collection package (F220FC-B coupler with a M31L03 fiber, both from Thorlabs) to be detected by a single-photon detector (avalanche photodiode, PerkinElmer SPCM-AQR-14) for heralding. With successful heralding on the 989-nm channel, the 683-nm signal was very likely to be in the $|1\rangle$ Fock single-photon state. The 683-nm channel was sent through a bandpass filter (FB680-10, Thorlabs) before entering the rest of the setup.

The rest of Pump one, and all of Pump two, were combined on a dichroic mirror (DM, 741-Di01, Semrock), with the resulting beam further combined with the 683-nm signal from Fiber one by use of another DM (741-Di01, Semrock).[1] The fiber

[1]The angle for both of these DMs with respect to the incoming beams was not 45 degrees. These DMs could be tuned in wavelength by varying the incident angles, which was used for optimal combination in these two instances.

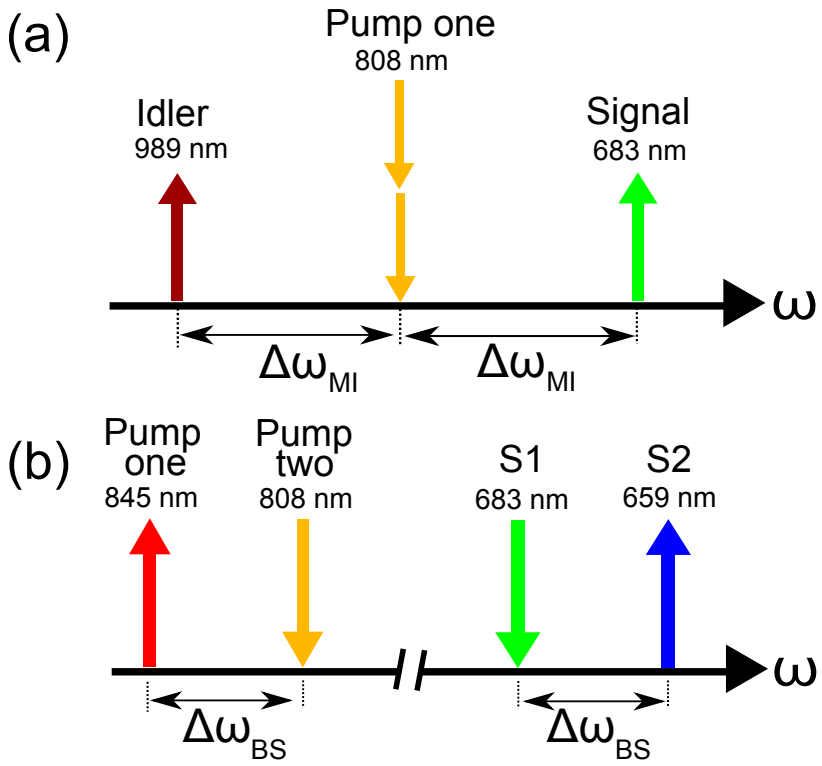

FIGURE 6.2. MI and BS wavelengths. (a) The modulation interaction process. Two Pump one photons are annihilated while two sideband photons (signal and idler), equally spaced in frequency from the pump by $\Delta\omega_{\mathrm{MI}}$, are created. Up(down) arrows indicate creation(destruction). (b) The Bragg-scattering quantum frequency translation process. Photons from Pump one and the $S1$ mode are annihilated while photons in Pump two and the $S2$ mode are created. The frequency separation between the pumps $\Delta\omega_{\mathrm{BS}}$ is equal to the separation of $S1$ and $S2$.

length and positioning of Fiber one was such that the pulses of both pumps and the 683-nm signal pulse maximally overlap. All beams had the same polarization. All three beams were then incident upon 20 meters of Fiber two (Crystal Fibre, model number NL-PM-750, described below), and aligned on one of the principal birefringence axes of the fiber through use of a HWP. Around 20 (30) mW of average power from Pump one (two) was coupled into Fiber two. The object used for coupling (M-60X, Newport) in had a magnification of 60x and the objective used for coupling the beam out had a magnification of 20x (M-20X, Newport). The stage used for coupling was a single-mode fiber coupling stage (F-915, Newport). A percentage of the 683-nm photon state was frequency translated to a new field centered around 659-nm, as pictured in Figure 6.2.(b). The frequency difference between the pumps, and therefore between signal and idler, was $\Delta\omega_{BS} = 1.0 \times 10^{14}$ rad Hz. After exiting Fiber two, the pump components were filtered out of the beam using a shortpass filter (740 alpha shortpass, Omega Optical), which was then separated into the 683-nm and 659-nm channels via a DM (FF669-Di01, Semrock). Both channels were filtered with bandpass filters (FB680-10 and FB660-10 from Thorlabs, respectively).

Second-order correlation measurements ($g^{(2)}(0)$) of the 683-nm and 659-nm channels were carried out in coincidence with the 989-nm channel in order to determine if the initial and translated beams were nonclassical in nature. In each of the 683-nm and 659-nm channels a HWP and a PBS were used to send equal intensities of light to two multimode fibers (similar to the 989-nm detection scheme) and then to two channels of a four channel single photon detector (SPCM-AQ4C, PerkinElmer). Therefore for each channel being detected, three single-photon detectors were involved; two detectors monitoring the 683-nm (or 659-nm channel) equally spaced from the PBS, and one monitoring the 989-nm channel. Note that the

989-nm beam detection must be electronically delayed by 90 ns by use of a custom-made (Cliff Dax, Electronics Shop) coax-cable delay line. As explained in Chapter II, the expression for $g^{(2)}(0)$ of a field in this detection geometry is given by

$$g^{(2)}(0) = \frac{N_{ABC}N_C}{N_{AC}N_{BC}}, \tag{6.1}$$

where A and B label the detectors monitoring the output of the 683-nm or 659-nm channels, and C labels the heralding detector in the 989-nm channel. The quantities N_i, N_{ij}, N_{ijk} are the number of single, double coincidence, triple coincidence events between detectors i, j and k over the time interval of the data collection, respectively.

6.1.2. Fibers

Both fibers used in the experiment, one used to create photon states and the other used to frequency translate those states, were solid core PCFs made out of pure fused silica. Scanning Electron Microscope (SEM) images of both fibers are shown in Figure 6.3.. The most salient geometric traits of such fibers are their core size and air-filling fraction, which can be used to model their dispersion characteristics as discussed in Chapter III. The air-filling fraction for a solid, single-defect core is proportional to the square of the ratio of the hole diameter and the pitch (hole to hole distance). The most important property of PCFs in regards to FWM interactions is their dispersion, so it is desirable to discover their dispersion. However, most PCFs in actuality have small, but important, deviations in these parameters along their lengths. These deviations can have a meaningful impact on their dispersion characteristics. Ideally one would like to measure the dispersion over a given wavelength range [97] and not rely on a few parameters to generate a model of the dispersion. This is particularly true for

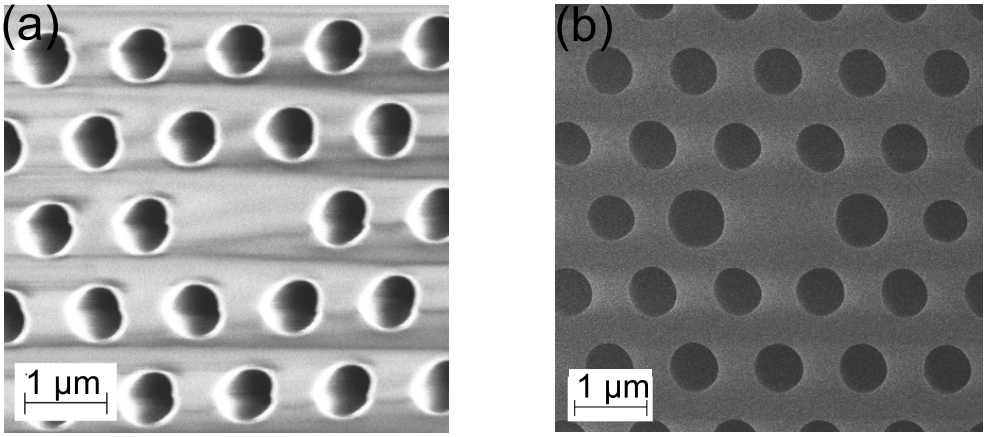

FIGURE 6.3. SEM images of Fibers one and two. (a) Scanning Electron Microscope (SEM) cross-sectional image of Fiber one. (b) Cross-sectional SEM image of Fiber two. The two large cladding holes near the core help to induce birefringence in the fiber.

Fiber one, which was a custom-made PCF that did not meet its original targets for core size and air-filling fraction.

Recently, a technique for indirectly measuring the dispersion of a PCF by measuring the FWM modulation instability (MI) it produces for various pump wavelengths has been proposed, and shown to be valid for a swath of the PCF parameter space [19]. In this method, the core size and air-filling fraction are free parameters of the effective index model for PCFs. Since core size and air-filling fraction uniquely determine the dispersion in the model it is possible to predict what MI products will be produced for a given core size and air-filling fraction. By comparing theoretical MI data for a set of core/filling parameters to the experimentally measured MI data, the core/filling parameter that best fits the data, according to a least-squares metric, of the set can be discovered. This method was carried out for Fiber one, and both theoretical and experimental MI data is shown in Figure 6.4.(a). The error bars for the experimental data were taken to be the uncertainty in measuring the wavelength in both pump and MI product variable

due to the spectrometer (SPM-002-C, Photon-Control), with the error value being ± 0.6 nm. The best-fit core and air-filling fraction were approximately 0.802μm and 0.432, respectively. Fiber two was a commercially available PCF from Crystal Fibre, model NL-PM-750. An estimate of the core radius and air-filling fraction was attained using the same method employed for Fiber one and the resulting MI data and best-fit curve are shown in Figure 6.4.(b), with the results being approximately 0.720μm and 0.494, respectively. The codes used to make these parameter estimations are available upon request. Both fibers are predicted to be single-mode for all the relevant fields that propagate down them in this experiment.

With an estimation of the core and air-filling fraction, the dispersion of Fiber one can be estimated. As noted earlier, the common parameter use to quantify the dispersion characteristics is the D parameter, which is related to the second-order dispersion $\beta^{(2)}$ through the relation $D(\lambda) \cong -2\pi c/\lambda^2 \beta^{(2)}(\lambda)$. Using the effective index model for solid-core PCF and the best-fit values for the core and air-filling fraction, D for Fiber one is shown in Figure 6.5.. As can be seen from Figure 6.5., fiber one has two zero-dispersion wavelengths (ZDW), one around 780 nm and another at 1262 nm. Fiber two has ZDW around 735 nm and 1200 nm. The ZDW parameters are particularly important in FWM processes. For MI, D is the most important parameter in determining the sideband central wavelengths, with the ZDW determining at what wavelengths higher-order dispersion terms become important. For BS, as discussed in Chapter IV, the ZDW is close to the wavelength at which the annihilated and created fields average to energetically (the point, in frequency, in which the interaction is centered around). For this experiment, the annihilated and created fields were centered near 740 nm, which is close in wavelength to the measured ZDW of Fiber two.

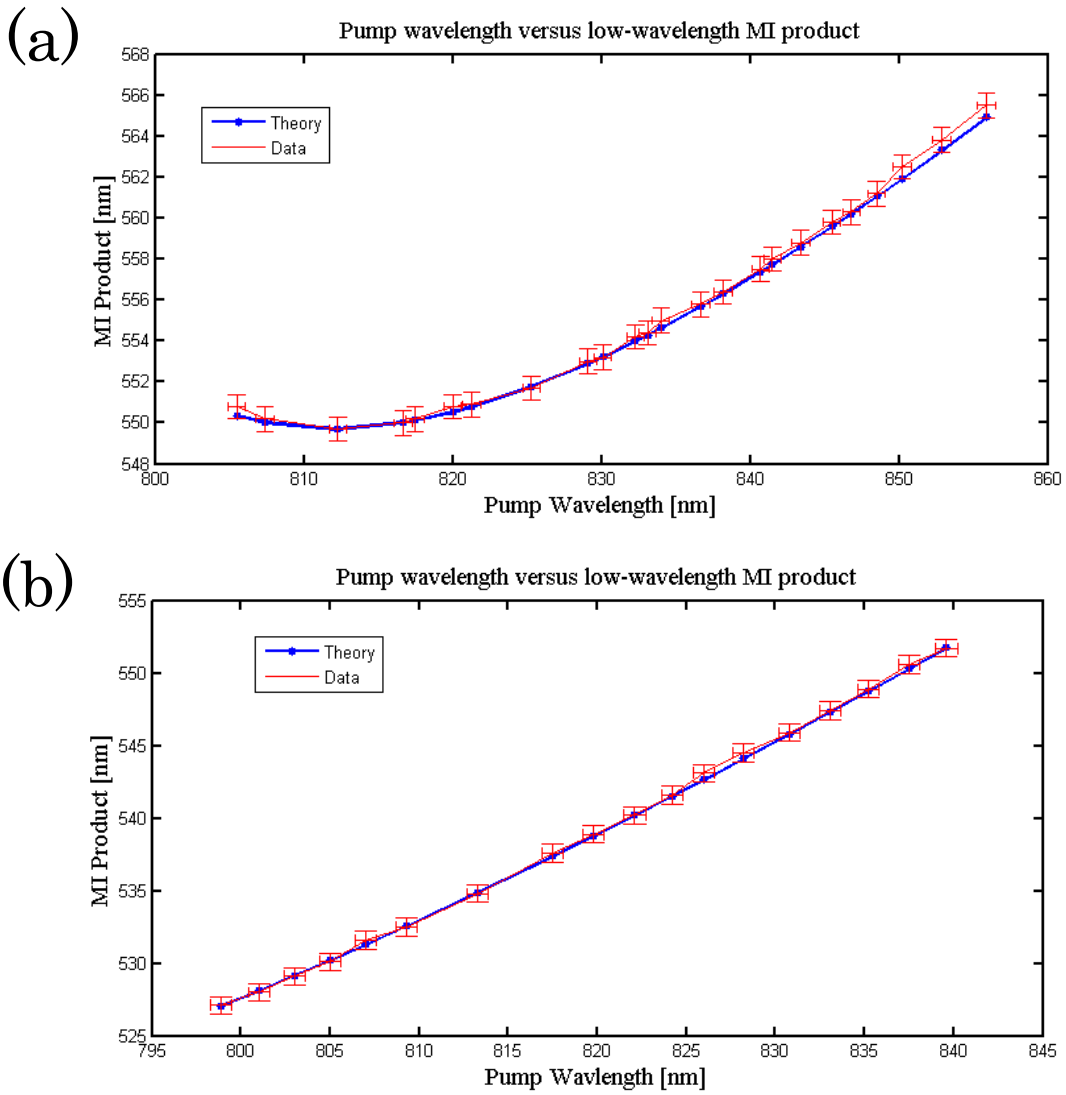

FIGURE 6.4. Dispersion fitting data for Fibers one and two. (a) Experimental data and best-fit theoretical predictions of the low-wavelength MI product as a function of pump wavelength for Fiber one. The error bars are due to uncertainty in the wavelength measurement due to the spectrometer and have a magnitude of ± 0.6 nm. The best fit parameters are 0.802 and 0.436 for the core radius and air-filling fraction respectively. (b) Experimental data and best-fit theoretical predictions of the low-wavelength MI product as a function of pump wavelength for Fiber two. The error bars are also due to the spectrometer, with magnitude ± 0.6 nm. The best fit parameters are 0.720 and 0.494 for the core radius and air-filling fraction respectively.

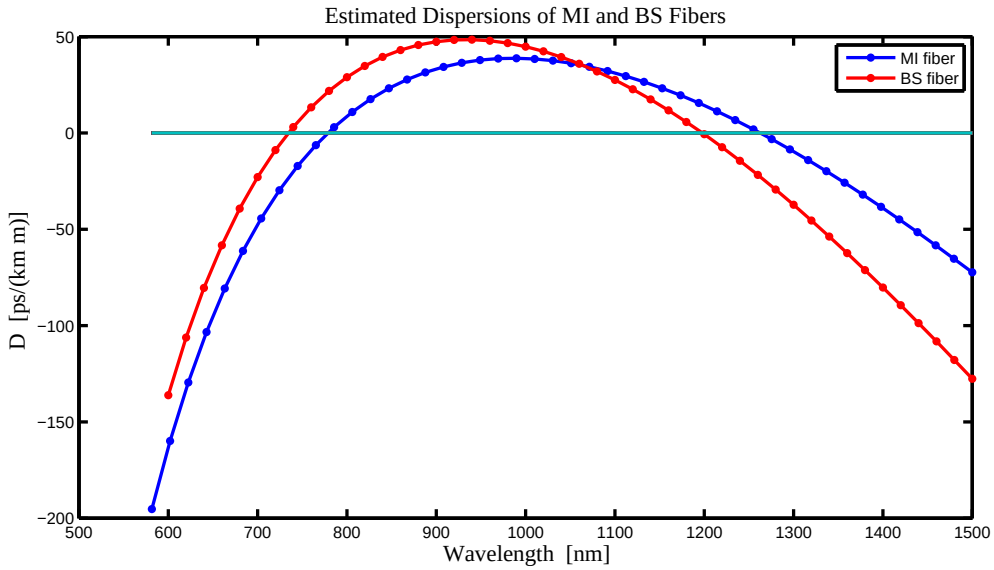

FIGURE 6.5. Dispersion parameter D of Fibers one and two. The data for fiber one was modeled from the effective index model for PCFs with best fit parameters of core radius equal to 0.802 and air-filling fraction equal to 0.436. The data for fiber one was modeled from the effective index model for PCFs with best fit parameters of core radius equal to 0.720 and air-filling fraction equal to 0.494. A line at zero dispersion is included for easy of reading.

There is another critical property that most PCFs have: birefringence. Even when no attempt is made to produce a birefringent fiber usually there is some residual birefringence on the order of $\Delta n \sim 10^{-5}$ [15]. In standard fibers this residual birefringence would be somewhat of a nuisance; not large enough to have good polarization maintaining properties but large enough to make the fiber significantly non-isotropic. However, since PCFs often have ZDWs near the visible spectrum this residual birefringence can be useful in FWM processes. In fact, the photons used for frequency translation in fiber two were created by the birefringent "vector" MI process [96], where the pump beam was polarized along one optical axis of Fiber one while sidebands were created with polarizations on the other optical axis. The birefringence can be estimated in a similar fashion to that of the dispersion. Once a best-fit value for the nonbirefringent dispersion has been attained, by measuring the vector MI product wavelengths for multiple value of the pump wavelength the birefringence can be estimated. This process was carried out for Fiber one and the experimental data and best-fit theoretical predictions are shown in Figure 6.6.. The best-fit value for the birefringence was found to be $\Delta n \cong 4.3 \times 10^{-5}$. This value, while nearly an order of magnitude lower than that of standard birefringent fiber, is relatively large for PCFs that are not designed to exhibit birefringence. The birefringence of Fiber two was not measured as all input fields were co-polarized on one axis.

6.1.3. Detectors, Coincidence Circuitry and Computer Code

The detectors used for heralding the idler photon and monitoring the frequency translation output channels were single-photon APDs run in Geiger mode made by PerkinElmer. The four detectors used for monitoring the output were integrated into a single unit, model SPCM-AQ4C, while the detector used for heralding was a

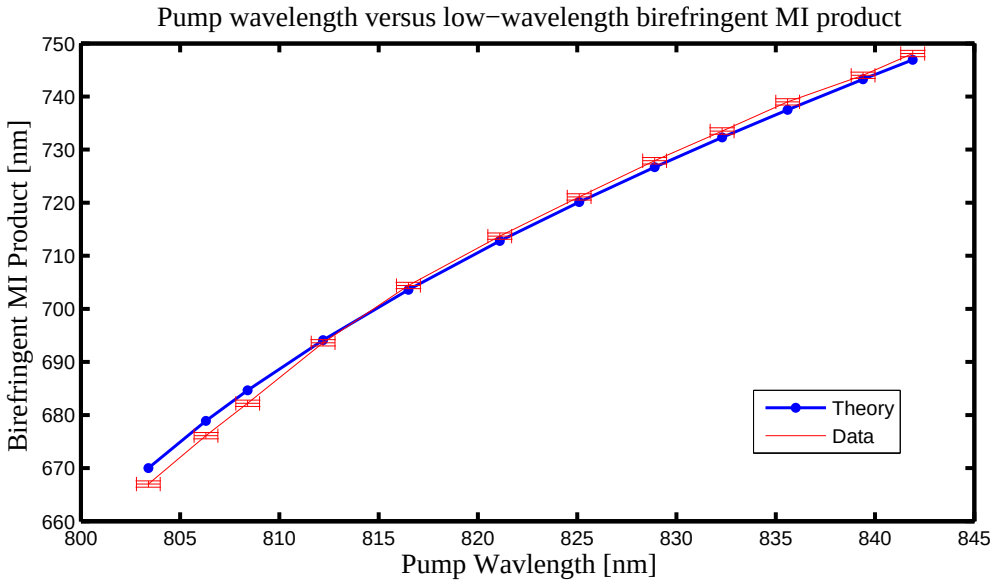

FIGURE 6.6. Birefringence measurement for Fiber one. With known/given dispersion and using the birefringence as a free parameter, the best-fit value for the birefringence of the fiber is found by fitting experimental vector MI data to predicted MI values. Error in measurement is due to the uncertainty in the spectrometer measurement, and has the value of ± 0.6 nm.

single unit, model SPCM-AQR-14. The most important parameters of these detectors to this experiment are their quantum efficiency as a function of wavelength and dark count statistics. In Figure 6.7. the quantum efficiency curve as a function of wavelength is shown, taken from the SPCM-AQ4C datasheet. While the detectors have good efficiency at the signal frequencies $S1$ and $S2$, over 50 percent, the efficiency at the idler wavelength is not good, being around 12 percent. The effect of this low efficiency to increase the required data collections times, as discussed in the next chapter. The dark count rate for all detectors was specified by the manufacturer to be less than 500 counts/sec, which was found to be the case. Such a low rate did not meaningfully impact the outcome of the experiment, since the rate of true counts was several orders of magnitude higher, between 10^5 and 10^6 per second. The detectors were FC conectorized and were connected to multimode, graded-index

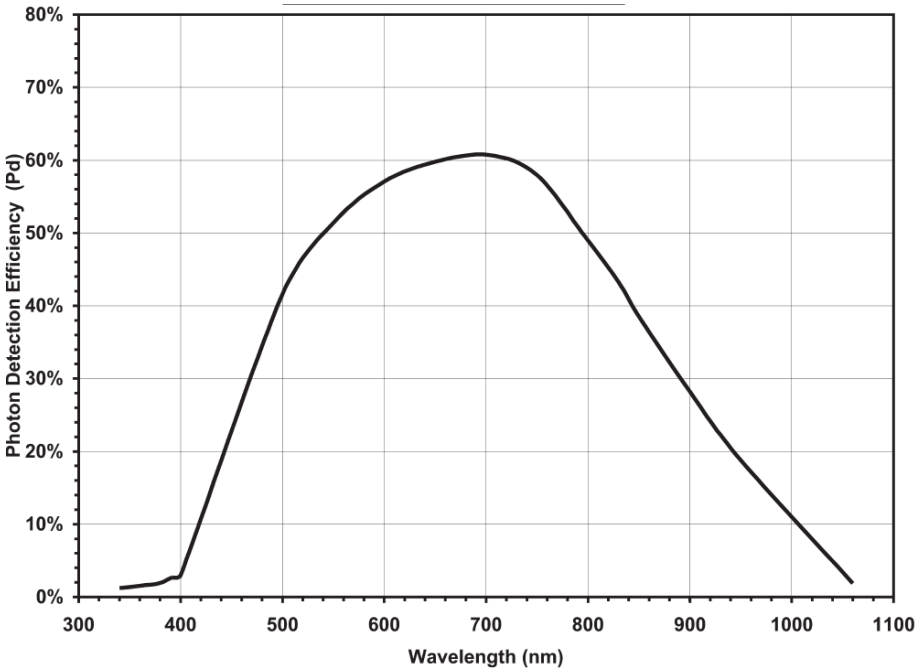

FIGURE 6.7. The quantum efficiency of the APDs used in the experiment.

fibers. The fiber coupling allowed for significantly easier light collection than would have otherwise been possible with free-space detectors and also served to block much of the stray noise light. The maximum count rate specified is 1.5 million count/sec, although in practice the maximum rate seemed to be somewhat higher, around 2 to 2.5 million count/sec.

Upon detection of a pulse, the detectors would output a TTL pulse that was sent to a five-channel coincidence circuitry unit. At the heart of this unit was a 240 pin Field Programmable Gate Array (FPGA) chip (CYCLONE, Altera) that was programmed to tally a set of the possible coincidences from all five channels. An FPGA is essentially an integrated circuit in which the logic gates of the circuit can be physically rewired, or reprogrammed, after the device has been manufactured [98]. In this instance it was programmed to calculate all single, double and triple coincidences between all five input channels, and therefore between all five single-

photon detectors. Single, double and triple coincidences were used to calculate quantities such as $g^{(2)}(0)$, the overall efficiency of the translation process and the noise in each channel. The coincidence circuitry and associated software was designed at the University of Toronto by the Steinberg group for use in quantum optics experiments. All fabrication files, parts list and software including LabView code to interface the coincidence circuitry to a computer, along with instruction on how to build and use the circuitry/software, is available upon request.

6.2. The Classical Translation Experimental Apparatus

In the preceding translation experiment, all the fields were co-polarized and coupled into the same birefringent axis of a fiber. The BS process does not require all fields be co-polarized; in fact, there are four possible configurations as shown in Figure 6.8.. Here we describe a classical BS translation experiment in which the pumps are polarized on one axis of a birefringent fiber and the sideband fields are polarized on the other. As alluded to in the introduction, this configuration may offer advantages over the co-polar configuration in some circumstances. Most importantly, for large frequency shifts the Raman gain coefficient may go down by more than an order of magnitude for this configuration as compared to co-polar configuration, making this configuration optimal for minimizing noise in the sideband fields. Also, having the pumps on an orthogonal polarization axis gives another degree of freedom with which to filter the pumps out after the fields exit the fiber.

6.2.1. Setup, Fibers, and Hardware

The experimental setup used to demonstrate classical frequency translation is shown in Figure 6.9.. Pump one was a titanium sapphire modelocked laser operating

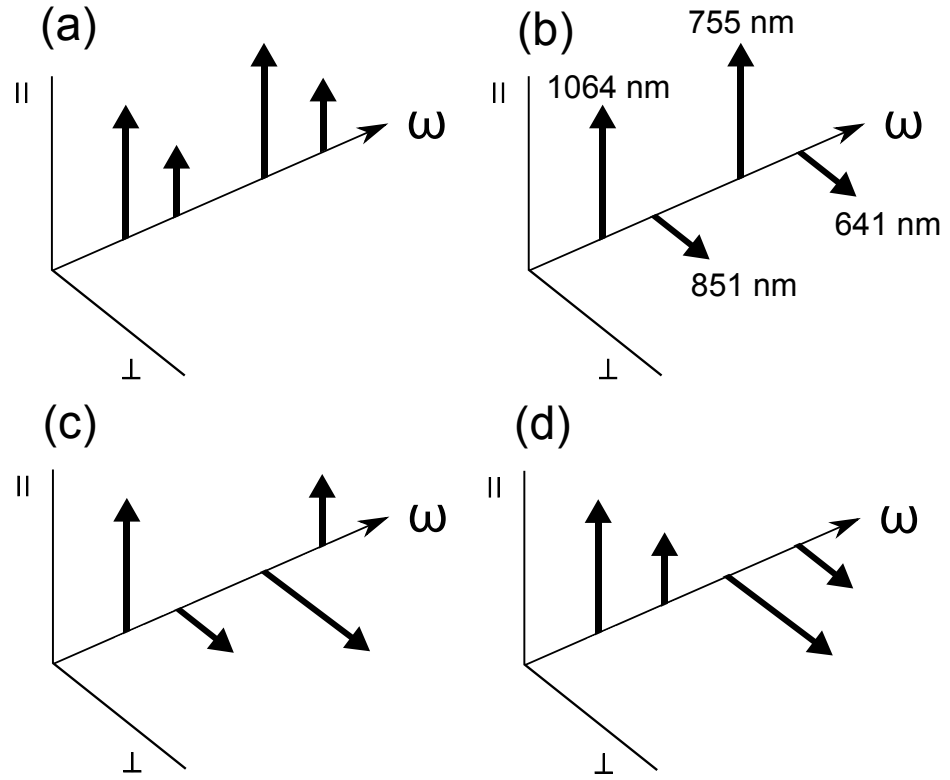

FIGURE 6.8. The four possible pump-sideband configurations possible in a birefringent fiber. Large arrows represent pump fields while small arrows represent sideband fields. The lines labeled perpendicular or parallel could be either the slow or fast axes. (a) The co-polar case. (b) The pumps and sideband fields are orthogonal. It was this configuration, with the associated wavelengths, that was used in the experiment. (c) The pump fields are orthogonal to each other and the sideband fields are orthogonal to each other. (d) Beams that are annihilated/created together are orthogonal.

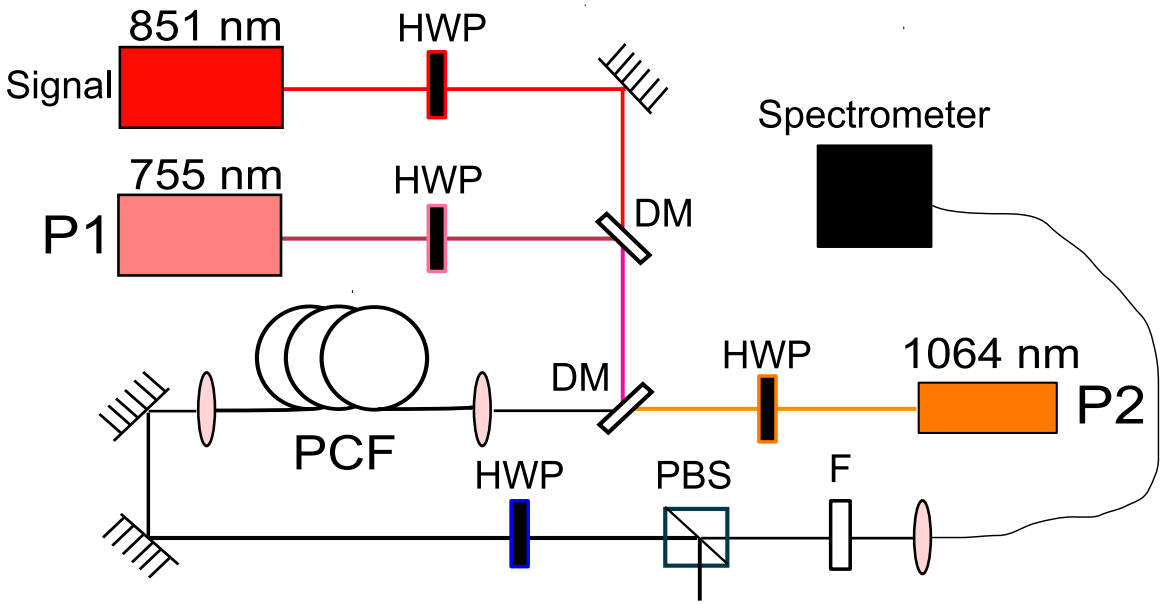

FIGURE 6.9. Diagram of the setup used to show birefringent BS frequency translation of classical fields. The signal field to be translated is combined with Pump one (P1) and Pump two (P2). The polarization of each field is adjusted with the use of HWP. The output from the fiber is sent through a spectral filter (F) and PBS, where it is then measured by a spectrometer.

at 755 nm with a pulse width of about 100 ps. The weak sideband field that was translated originated from a commercial titanium sapphire modelocked laser (Time-Bandwidth, Tiger-ps series) operating at 851 nm with a pulse width of also about 100 ps. Both lasers had a repetition rate of 76 MHz and were synchronized with the use of a commercial PLL (Time-Bandwidth). Pump two was a commercial CW Nd:YAG laser (Skylasers) operating at 1064 nm. The fields were polarized in a manner such that both pumps were co-polarized while the 851 nm signal was polarized orthogonal to the pumps. The two pulsed beams were combined with the use of a dichroic mirror (801-Di01, Semrock) while the 1064 nm field was combined with the other fields with the use of another dichroic mirror (NT52-534, Edmund Optics). The fields' polarizations were manipulated with the use of half-wave plates (10RP42-3, Newport). The microscope objective (M-60X, Newport) used for coupling into the

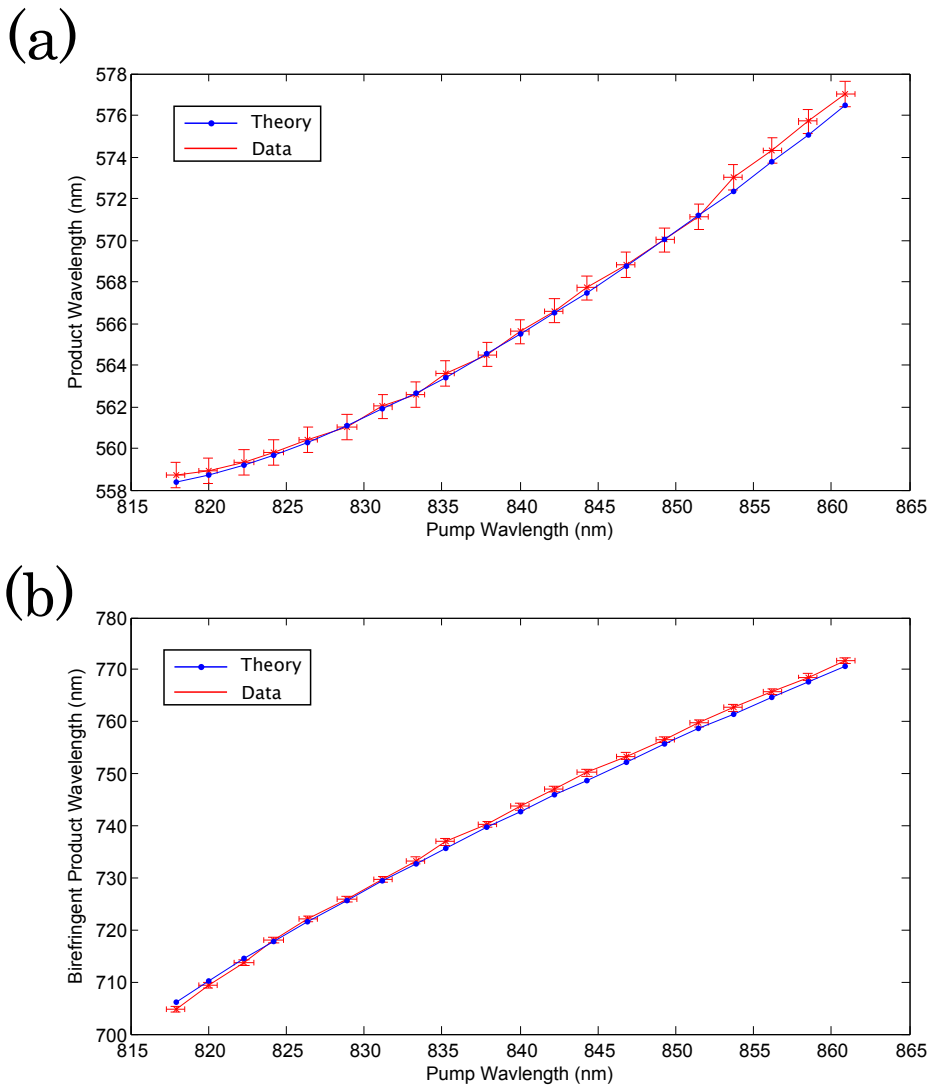

FIGURE 6.10. Dispersion fitting data for classical BS fiber. (a) The best-fit curve for the step-index model for the fiber used in the classical BS experiment. Data points (red) have an error of 1.2 nm in both dimensions, solely derived from the spectrometer uncertainty. The best-fit parameters were a core radius of 0.783 μm and air-filling fraction of 43.7 percent. (b) Best-fit curve for the birefringent MI data fitting. The best-fit value for the birefringence was $\Delta n = 4.5 \times 10^{-5}$.

fiber had a magnification of 60x while the objective used to couple out the fields (M-20X, Newport) had a magnification of 20x. The stage used for coupling in was a single-mode fiber coupling stage (F-915, Newport). Approximately 90 mW of average power of Pump one, 40 mW of Pump two and 10 μW of average power of the signal field were coupled into the fiber. The fiber was a custom-made PCF with a length of approximately 10 m, and is described in more detail below. After passing through the fiber, the output is filtered using either a 860-nm centered, 20 nm bandwidth filter (860DF20, Omega Optical) for monitoring the input signal level, or a 695-nm edge long-pass filter (695ASP, Omega Optical) for monitoring the translated field at 641 nm. The output is monitored with a visible/NIR spectrometer (SPM-002-C, Photon Control).

Using the step-index modeling technique described in Chapter III, dispersion properties of the custom PCF used in the experiment can be accurately estimated. After modeling the appropriate MI data, the best-fit core radius and effective filling fraction were found to be 0.783 μm and 43.7 percent, respectively. Figure 6.10. shows the MI data and the resulting best-fit estimate derived from the best-fit core and air filling fraction values. Figure 6.11. shows the resulting D parameter values as a function of wavelength, with ZDWs of approximately 785 nm and 1225 nm. The birefringence can also be estimated in a similar manner. By measuring the birefringent MI product as a function of pump wavelength, with the knowledge of the best-estimate for the fiber dispersion without birefringence, the birefringence is used as a free parameter to fit the data. The best-fit value for the birefringence was found to be $\Delta n = 4.5 \times 10^{-5}$.

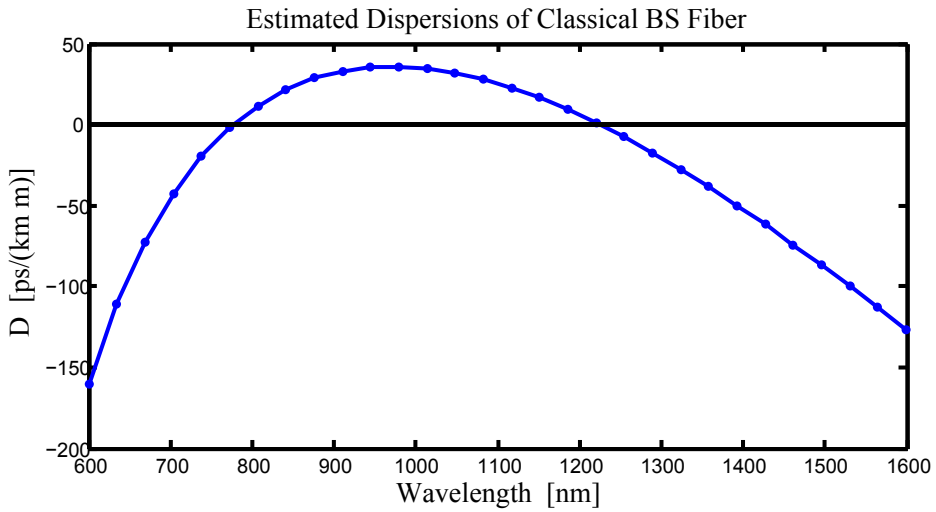

FIGURE 6.11. Estimated value of the D parameter derived from the best-fit value of the core and air-filling fraction for the fiber used in the classical BS experiment. A line at zero D value is included for reference.

CHAPTER VII

EXPERIMENTAL RESULTS AND DISCUSSION

7.1. The Quantum Translation Experiment

For this experiment, the most important result is that of the measured value of the second-order correlation measurements at zero time delay ($g^{(2)}(0)$) of the 683-nm untranslated channel and 659-nm translated channel, given by the expression of (6.1). As described in Chapter II, any Fock state of light will give a value of $g^{(2)}(0)$ less than 1. But fields that are produced experimentally rarely have a perfectly defined number of photons in them; actual fields are a superposition or mixture of Fock states. In this sense the experimentally non-zero value of $g^{(2)}(0)$ can be used to interpret the Fock-state composition of the field. In general, the closer $g^{(2)}(0)$ is to zero, the more the state is dominated by the $|1\rangle$ Fock-state.

It was found that value of $g^{(2)}(0)$ for the untranslated 683-nm channel upon exiting Fiber two in Figure 6.1. was 0.21 ± 0.02. The value of $g^{(2)}(0)$ for the translated 659-nm channel upon exiting Fiber two was 0.19 ± 0.05. These values and associated errors were calculated by running the experiment 30 consecutive times, where each experiment lasted for 20 seconds, and averaging the results. Considering their absolute value and error, both $g^{(2)}(0)$ values were under one by a significant margin, which provides strong evidence that both of these states were highly nonclassical in nature. With these $g^{(2)}(0)$ values and the knowledge that the states of the 683-nm and 659-nm channels are given to good approximation by *heralded* thermal fields (from (2.42)) having no vacuum component, the mean number of photons in the two fields can be accurately approximated. Using the expression of $g^{(2)}(0)$ from (2.57) we find

that the mean photon number for the 683-nm and 659-nm channels are $\langle n \rangle_{683} = 1.12$ and $\langle n \rangle_{659} = 1.11$, respectively. This implies that the single-photon component of the fields made up about 90 percent of the state. Also, both translated and untranslated channel had the same value of $g^{(2)}(0)$ to within error, strongly suggesting that the Fock-state nature of the 683-nm input channel was translated to the 659-nm output channel.

Although the $g^{(2)}(0)$ values were far below one, they were not near zero, as would be desired. There were a number of factors that caused the measured value of $g^{(2)}(0)$ for both channels to be meaningfully above zero. The dominant cause was likely the non-single photon state terms in the state. Unless a number-resolving detector is used for heralding detection (which was not available for this experiment), there is always a trade-off between achieving a high-probability single-photon state field and achieving a high count rate for states generated by the SFWM effect discussed in Chapter IV. As shown in Figure 6.7., the efficiency of the 989-nm idler channel was only around 12 percent. Due to this, and the somewhat lossy filters place in the idler beam path, it was necessary to input more pump power into Fiber one than would be desirable for high single-photon state generation in order to generate significant count rates. This caused the higher order terms of (2.58) to be larger than would otherwise be necessary, leading to a $g^{(2)}(0)$ significantly above zero. Although this was likely the dominant cause of nonzero $g^{(2)}(0)$ measurements, it was not the only one. Other possible causes include accidental coincidence counts from Raman scattering, detector dark counts and other noise. As one test of how much these noise terms affected the $g^{(2)}(0)$ values, the singles and coincidence rates, when Pump two at 845-nm (this pump didn't have a significant noise impact on either sideband channel) was block but Pump one and the 683-nm signal were coupled into Fiber two, were

measured. In this measurement, all coincidences in the 659-nm channel are due to noise from Pump one. No significant noise in the 659-nm channel could come from the 683-nm channel since a bandpass filter was placed in the beam path before it is coupled into Fiber two. The coincidence rates, such as between the 659-nm and 989-nm channels, were far less than 1 percent of the rate when the 845-nm pump is coupled in. Next, the 683-nm channel was blocked and both pumps were coupled in while coincidence rates were measured. Here the coincidence noise was somewhat more noticeable, but still under 1 percent of the rate when all three fields are coupled in. These test demonstrate that coincidence counts due to noise hardly affected the $g^{(2)}(0)$ measurements.[1]

The subject of accidental count rates brings up the matter of testing whether or not the signal and idler channels exiting Fiber one are actually correlated, as they must be for SFWM to be their source, or whether their coincidence rates are due mainly to noise generated by the pumps. Of course, if the input signals to Fiber two were just noise and not created by SFWM then the measured $g^{(2)}(0)$ values would be greater than or equal to one, hence it is clear that they must be correlated. But it is good, and simple, to verify their correlated nature directly. Consider the predicted coincidence counts that two independent, random Poissonian sources would produce. If over an interval of N_p time bins (or in our experimental setup, N_p pulses over a given time) source one produced N_1 counts and source two produced N_2 counts, then the expected number of "accidental" coincidences R_a of these two sources would be

$$R_a = N_1 N_2 / N_P. \tag{7.1}$$

[1]For both tests the coincidence counts between the 659-nm/683-nm and 989-nm channel were on the order of what was excepted according to (7.1).

Therefore, any experiment that relies on using counts/pulses from assumed correlated sources, such as the photon creation process via SFWM, must register more than this number of coincidences to be considered truly correlated. In the experiment, the coincidence level between the 683-nm channel after exiting Fiber two and the 989-nm heralding channel was approximately 8.2 times higher than the expected accidental coincidence rate of (7.1). The coincidence rate for the 659-nm translated channel exiting Fiber two and the 989-nm heralding channel was approximately 6.5 times higher than the expected accidental coincidence rate. This lower rate might have been related to the lower absolute count rate of the 659-nm channel relative to the 683-nm channel. Regardless, both values are significantly larger than one and testify to the highly correlated nature of the signal and idler channels produced through the MI process.

Another important parameter of the experiment, second only to the values of $g^{(2)}(0)$, was the efficiency of frequency translating input 683-nm photons to the 659-nm channel. To quantify this, both the depletion efficiency of the 683-nm channel and the creation efficiency in the 659-nm channel were measured. The depletion rate was obtained by measuring the count rates (minus noise counts, described below) of the output 683-nm channel when the pumps were and were not coupled into Fiber two, and its value equals one minus the ration of these rates, which is independent of the quantum efficiency of the detector. The result was 28.6 ± 2.2 percent. The raw 659-nm creation efficiency was equal to the count rate of the 659-nm channel with the pumps minus the count rate without the pumps, which accounted for any noise due to the pumps. When detector efficiency was taken into account, the raw creation efficiency rate divided by the rate of the 683-nm channel without the pumps equals

29.4 ± 2.4 percent. Hence the two measures of translation efficiency agree with one another to within error.

The noise counts in the experiment in practice were from the pump fields, due most likely to Raman scattering, and mostly from the 808-nm pump. Approximately 11 percent of the counts in the 683-nm channel, and 24 percent in the 659-nm channel, were due to noise. Although noise didn't severely affect the important results of this experiment, such the $g^{(2)}(0)$ value and calculated efficiency (noise was subtracted out), in an application such as the exchange of quantum information between devices this noise level would likely significantly degrade the effectiveness of such an exchange. Therefore it is important to note why noise was so pervasive in this experiment and what could be done about it in similar future experiments. Firstly, and most significantly, the farther separated the pumps are from the sideband channels the less noise due to Raman scattering there should be [60]. Also, due to the dispersion characteristics of the fibers and the wavelength ranges of the available pumps, it was necessary for the wavelength of Pump one to be at 808 nm, only 50 to 70 nm away from Fiber two's ZDW. Many nonlinear effects, such as supercontinuum generation and all its accompanying effects, increase exponentially the closer the pump field is to the ZDW. Hence operating the pump much further from the fiber's ZDW should decrease the noise in both sideband channels. For any particular set of pump and sideband wavelengths the Raman Stokes and anti-stokes noise can be reduced a considerable amount by cooling one or both the fibers, most likely with the use of liquid nitrogen [99].

Finally, there is the topic of why translation of the input field was limited to around 29 percent efficiency. Ideally this would be answered by calculating the output state with the split-step Fourier method described in Chapter V given the pulse

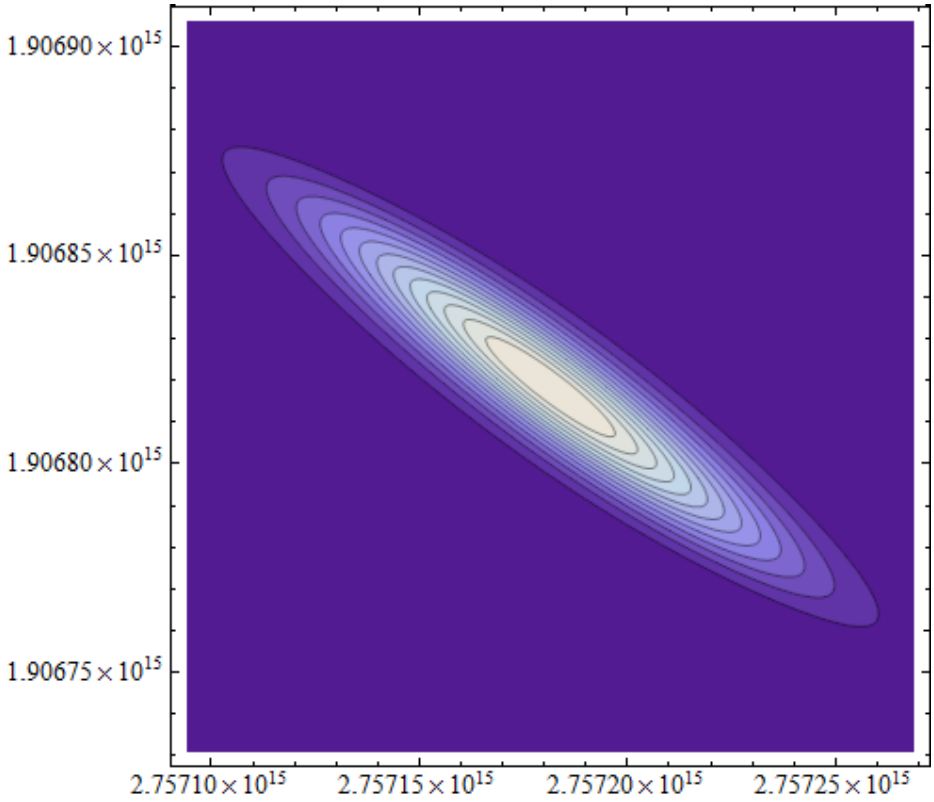

FIGURE 7.1. Theoretical calculation of the modulus square of the JSA that results from the MI process occurring in Fiber one due to an input pulse centered around 808 nm with a FWHM in frequency of about 3.5×10^9 Hz rad. For the projected photon state centered around 683 nm (2.75×10^{15} Hz rad), the amplitude spectrum has a FWHM around 25 times the 808 nm pump pulse FWHM. This calculated FWHM is still a couple orders of magnitude smaller than the experimentally measured FWHM.

parameter inputs and dispersion profiles of both fibers. Unfortunately this is not possible for a couple of reasons. One reason is that the signal spectrum derived from the MI process in Fiber one and input into Fiber two could not be measured due to its small bandwidth and low-power nature. The highest available resolution spectrometer had a resolution of 1.5 nm, and the 683-nm input pulse was found to have a FWHM of approximately 2.0 nm. As the input pulse was barely spectrally wider than the resolution, no fine-coarse spectral intensity details of the pulse could be measured, let alone the phase profile of the pulse. Without a good measurement of the input spectrum it is not possible to accurately calculate the output state.

This hurdle could be overcome by approximating the state of the signal pulse through the calculation of the bi-photon signal and idler JSA that results from the MI process in Fiber one. This has been carried out and a plot of the modulus squared of the JSA, which is proportional to the spectral intensity, is shown in Figure 7.1.. The projection of the state onto the signal frequency axis yields a spectrum that has a FWHM of roughly 0.06 nm. While this is much larger than the original input bandwidth of the pulse it is much smaller than the observed bandwidth. There are at least a couple reasons that might explain this large discrepancy. When the pump is near the ZDW the MI sidebands' spectral width can become quite large, even spanning hundreds of nanometers [15]. Hence a slight miscalculation, or mismeasurement, of the dispersion profile could lead to a significantly different calculated state than the state that actually occurs. Exacerbating this sensitivity to the dispersion profile is the known phenomenon that PCFs often suffer from significant dispersion fluctuations due to random core diameter, hole diameter, and pitch fluctuations along the length of the fiber [100, 101]. While this effect is usually used to explain the lower-than-would-be expected nonlinear gain coefficients of PCFs it is also true that this would

broaden out the output pulse from an MI process due to multiple points of equivalent phase matching. The particular fiber used for the MI process in this dissertation may be even more prone to such an effect since the manufacturer of the fiber declared that the fiber's core and hole size were not acceptably close to the target core and hole size. In other words, there were errors in the manufacturing of this particular fiber, and these errors could quite conceivably contribute to a fluctuating dispersion profile of the fiber. This fluctuating dispersion could also help explain why Fiber two was able to translate an input state that was so spectrally broad. While the BS nonlinear gain would be decreased due to this effect, the bandwidth of the BS process, the frequency range it could efficiency translate, would increase, allowing broader states to be translated. Detailed modeling of these fluctuating processes with PCFs would be necessary in order to accurately calculate the results of the BS process, which is beyond the scope of this dissertation.

7.2. The Classical Translation Experiment

The apparatus and interpretation of the results of the classical translation experiment are significantly simpler than for the quantum translation experiment. In this experiment, all that is of interest is the power that was transferred from the 851 nm channel to the 641 nm channel. The power level of the 851-nm channel was measured when the 755-nm pump field wasn't allowed to couple into the fiber. In contrast, the power of the 641-nm field was measured when both pumps were coupled into the fiber. Unfortunately, the dynamic range of the spectrometer was not large enough to obtain measurements of both the 851-nm and 641-nm channel simultaneously, let alone measure all fields simultaneously. Because of this, to obtain an accurate estimate of the translation efficiency, the spectral response of the filters

and spectrometer much be taken into account. After this was done, we estimate that the conversion efficiency of the vectorial BS process, as pictured in Figure 6.8. (b), was approximately 0.2 percent. Because the 851-nm and 641-nm channels were of classical strength, on the order of microwatts, and because they were on the low-wavelength, anti-stokes side of the pumps, there was no detectable noise from Raman scattering or any other source that the spectrometer could measure.

The translation efficiency for this experiment was significantly lower than that of the quantum translation experiment. This is due to several readily identifiable reasons, all of which could be mitigated in future experiments. While the average powers of the pumps were of the same order of magnitude as in the quantum experiment, one pump was pulsed and the other was CW. The input 851-nm signal was also pulsed and synchronized with the pulsed pump, meaning that the vast majority of the CW pump laser power did not contribute to the translation process. Obviously a far better scenario in terms of efficient translation would if the 1064 nm pump was actually pulsed and overlapping with the other fields. The vector BS process is inherently less efficient than its scalar counter part due to the fact that the value of the nonlinear constant γ goes down by a factor of 1/3 when compared to that the scaler nonlinearity [60]. With the efficiency scaling going roughly as the square of the nonlinearity low efficiency process [24], this implies that the vector BS process is nearly an order of magnitude weaker than the scalar BS process. This weakened nonlinearity is compounded by the phenomenon of fluctuating core, hole size, and hole spacing in PCF which further lessens the nonlinearity as described in the previous section. This effect is particularly severe for the classical experiment as opposed to the quantum experiment since the frequency shift is much larger in

the classical case. Finally, the length of the fiber could be increased by an arbitrary amount, allowing for a longer interaction length.

Although there was no detectable noise due to the pumps, small powers in both the 851-nm and 641-nm channels were detected on the orthogonal polarization axis as compared to the main components of those channels (these small fields were on the same polarization axis as the pumps). The smaller fields for the 851-nm and 641-nm channels were smaller by a factor of approximately 10 and 16, respectively, from their counterparts on the other polarization axis. The cause of this was probably polarization leakage from one polarization axis to another, likely due to the imperfect polarization-maintaining properties of the PCF, which was not designed for the purpose of maintaining polarization. Also, the maximum polarization ratio achieved for either one of the pumps was around 20, suggesting that there was some leakage of the pump fields during propagation. In this light it makes sense that the 641-nm channel was better polarized along one polarization axis; since the 641-nm field grows during propagation it will have less fiber length in which to scatter into the orthogonal polarization axis.

CHAPTER VIII

SUMMARY AND CONCLUDING REMARKS

In this dissertation we have studied theoretically and experimentally the classical and quantum nature of the four-wave mixing modulation instability and optical Bragg scattering phenomena in optical fibers used for photon creation and frequency translation, respectively. To properly understand the subject theoretically and to situate them in the current research efforts in the field of quantum optics, topics in nonlinear optics, the quantum nature of light, general fiber optics theory, and numerical simulation of propagating electromagnetic fields were discussed, albeit far too briefly to give the reader more than a small taste of the depth inherent in each of these fields.

The modulation instability process, in which two photons from an input laser field are annihilated and two photons with differing frequencies from the pump and each other are created, was studied in detail theoretically. Photon pair generation from four-wave mixing in fibers is a relatively new technique compared to pair generation from three-wave mixing such as parametric down conversion in nonlinear $\chi^{(2)}$ crystals. This latter method has been, and still is, the work-horse technique for creating quantum states of light in the field of quantum optics practically since its inception. However, for a number of reasons such as ease of use, ease of achieving phase matching at desired pump/sideband fields, creation in a single spatial mode, and integration with optical devices, techniques such as four-wave mixing in optical fiber are beginning to be used more often in laboratories around the world. In the study of modulation instabilities' spectral creation properties, it was found that nearly any degree of spectral correlation between the two created photons can be achieved, with details

such as the central wavelengths of the created photons and their spectral width highly dependent on the properties of the fiber. The role birefringence plays in this process was also discussed, with the conclusion that the vector modulation instability process is often a very convenient way in which to produce photon pairs. The most interesting cases in general are those where the photon pair exhibit either maximal or minimal spectral correlation, i.e. form either completely entangled or completely pure states, respectively. While much attention has been paid to entangled states in the past couple of decades, we focus on analyzing the cases that lead to pure state creation. Pure states are a necessary resource for any quantum information technology that relies on Hong-Ou-Mandel interference, such as linear-optical quantum computing [102]. It was found that under generally achievable pump laser conditions and fiber properties, pure states can be created that are over 99 percent pure with a minimal amount of spectral filtering. Also discussed theoretically was the Bragg scattering process, used experimentally in this dissertation to translate classical and quantum states of light from one central frequency to another central frequency. Unfortunately, for the general case of arbitrary input fields, the solution for the resulting output is not solvable analytically because it cannot be treated in a perturbation manner, like modulation instability can. Therefore the only recourse is to solve the equations of motion, derived from the nonlinear Schrödinger equation, numerically for particular input fields and particular fibers. A code was written that does exactly that, and solutions to a range of important cases were studied in an attempt to extract some general properties about the Bragg scattering translation process from specific cases. The results generally conformed to what one would intuitively guess; for pulses with the same energy, the longer pump pulses translated the input field more efficiency, while the shorter pulses, particularly when the the pump pulse was shorter than the

input field, did not translate efficiency and significantly distorted the the input field when it was translated to the output mode. For the cases where short pump pulses did not translate efficiently, the efficiency and the length at which maximum translation occurred increased when the pump pulse was increased in energy, essentially due to the larger Bragg scattering bandwidth engendered by a smaller fiber length. The two-color Hong-Ou-Mandel interference effect [33] was also explored computationally for a range of important cases, and conditions in which the effect could be differentiated from a similar classical interference effect were discussed. It was found that the cases in which good translation occurs are also the best for seeing the two-color HOMI effect, although it would still be possible to see the effect in cases in which only 35 percent translation occurred.

Experimentally, a demonstration of Bragg scattering used to frequency translate a verifiably single-photon state of light from a central wavelength of 683 nm to a verifiably single-photon state of light having a central wavelength of 659 nm was demonstrated, with the technique used to verify the single-photon nature of light being the second-order correlation, or $g^{(2)}$, measurement. For a field to be mainly composed of a single Fock state, a nonclassical state of light, the value of $g^{(2)}$ at zero time delay must be less than one, whereas for classical light the value of $g^{(2)}(0)$ is always greater or equal to one. Both channels were measured and the 683-nm channel had a $g^{(2)}(0)$ of 0.21 ± 0.02 while the 659-nm channel had a $g^{(2)}(0)$ of 0.19 ± 0.05. These measurements indicate that both fields were largely dominated by the single-photon term, hence translation of a quantum state of light was demonstrated. The efficiency of the process, i.e. the probability that a photon in the 683-nm channel would be translated to the 659-nm channel, was shown to be around 29 percent. While frequency translation of quantum states of light has a rich history in $\chi^{(2)}$ media such as

nonlinear crystals, the work documented in this dissertation is the first experiment to demonstrate frequency translation in $\chi^{(3)}$ media. The main advantage that frequency translation in $\chi^{(3)}$ instead of $\chi^{(2)}$ media offers is that it allows for translation between closely separated frequency channels, which could allow quantum devices operating at similar, but not identical, frequencies to communicate with one another.

While that possibility could serve as motivation enough carry out such work, there is always the tantalizing possibility that any new phenomenon will be used in a manner not presently envisioned. An example of that occurred during work on this very project; the two-color Hong-Ou-Mandel interference effect, that has possible applications to linear-optical quantum computing, was thought of well after the attempt to demonstrate quantum frequency translation was underway.

Also demonstrated experimentally was a vector Bragg scattering process, where in a birefringent fiber the pump fields were polarized on one axis while the sideband fields were polarized on another. Translation was seen from the 851-nm channel to the 641-nm channel at an efficiency of around 0.2 percent.

Although the effect of quantum frequency translation in $\chi^{(3)}$ media has been demonstrated, there is much work to be done before it can be considered a viable tool for quantum information processing. First and foremost is the need to achieve a significantly higher translation efficiency. This is eminently achievable, since frequency translation in the classical regime has been shown to be nearly 100 percent efficient [28]. As a factor that decreased the efficiency in our experiment, it is quite likely that the 683 nm centered input state's was too spectrally broad to be effectively translated. With a less broad input state, most likely produced by a modulation instability process where the pump is not close to the zero-dispersion wavelength, the translation efficiency will be much higher. Secondly, the fibers used for both the

photon production and translation should be better characterized. Although fiber characterization was carried out to the best of our abilities in this dissertation, subtle effects such as the fluctuating dispersion phenomenon found in PCFs could have had a dramatic effect on the translation process. Thirdly, it would be desirable to fully characterize the quantum state of both the input and output field using the techniques of quantum state tomography [103]. These last two points, better characterized fibers and fully measured input and output states, would allow accurate numerical predictions of the nature of the output states given arbitrary input, facilitating the comparison of experiment to theory and giving one the confidence to claim that the phenomenon is fully understood.

APPENDIX

TITANIUM SAPPHIRE PUMP LASERS

In this appendix we will discuss the details of the two titanium sapphire modelocked lasers used as pump fields in the classical and quantum frequency translation experiments. We will focus on the home-built laser, since that was built and designed by the authors, although many of the design principles were all but copied from the pump laser that was purchased from Time-Bandwidth. This appendix will not be a tutorial on laser design, but will present basic principles that were important for the functioning of these particular lasers and will include the specific parameters used for the home-built laser.

The first thing to consider is the cavity design and geometry. A schematic of the cavity layout is shown in Figure A.1.. The cavity is designed to produce pulses at a rate of 76 MHz. This implies the cavity length is on the order of $L_c \cong c/(2 \cdot 76 \times 10^6) = 1.97$ m. A green pump laser operating at 532-nm, originating from a diode-pumped solid-state CW laser (Verdi V-5, Coherent), is focused by the pump-focusing lens (LA1986-A, Thorlabs) having a focal length of 125 mm and AR coated. The focused beam is passed through the first inner-laser cavity mirror (LGVD-700-825-1025-0.10CC, CVI) and incident onto and into the titanium sapphire (Ti:saph) crystal at Brewster's angle. The pump-focusing lens was placed approximately 150 mm away from the center of the crystal, with the distance being finely tuned for optimal lasing. Other than the dimensions of the crystal, which was measured to be $L_x = 12$ mm long, not much was known about its properties, namely, its doping level of titanium in the sapphire matrix. It was salvaged from a previous experiment, and came with a holding mount that could connect to water-cooling device that allowed

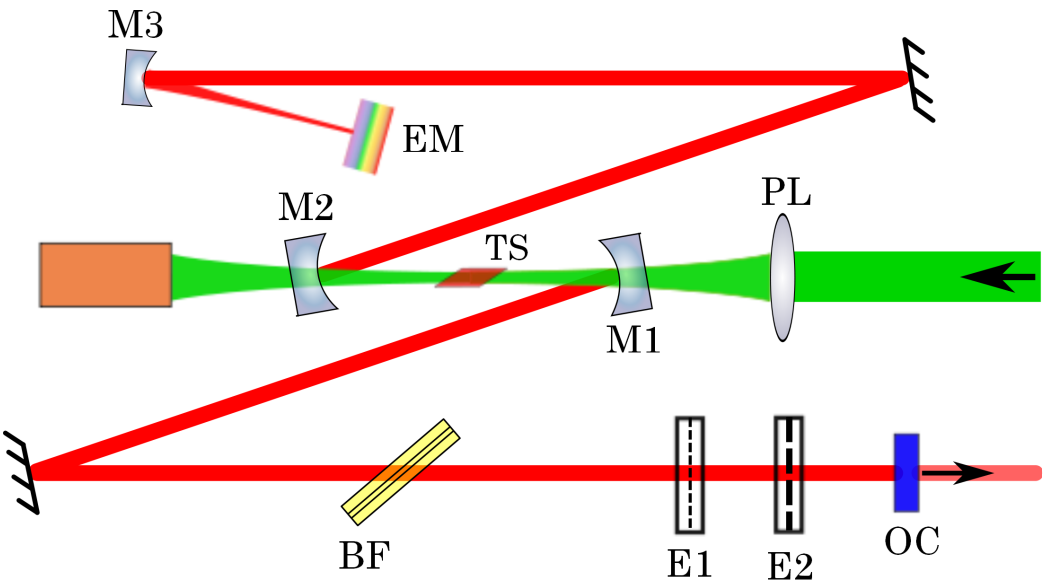

FIGURE A.1. General layout for both titanium sapphire pumps used in the experiment. Includes output coupler (OC), 0.1 mm thick Etalon (E1), 1.5 mm thick Etalon (E2), birefringent filter (BF), inner-cavity laser mirrors (M1 and M2), Ti:saph crystal (TS), pump-focusing lens (PL), focusing mirror (M3), and SESAM end mirror (EM). The green beam denotes the pumping laser field and the red beam denotes the Ti:saph laser field. Arrows indicate the direction of the pump field and output Ti:saph field propagation. The excess pump beam is terminated in a copper beam dump. Unlike femtosecond lasers, this laser does not require dispersion compensation since the spectral bandwidth is so narrow, being on the order of a gigahertz.

the crystal to be temperature controlled. After the pump field passed through the crystal (which absorbed around 84 percent of the beam) the passed through the second inner-laser cavity mirror, identical to the first inner-laser cavity mirror, and was terminated in a cavity beam dump consisting of a thick copper tube closed at the opposite end of where the pump field entered.

Some of the fluorescence from the crystal due to the absorption of the pump field is focused and somewhat collimated by the inner-cavity mirrors, which are very transmissive at the pump wavelength but highly reflective over the 700 to 825 nm range. For proper collimation, the mirrors must be at the correct distance away from the crystal center, in this case, about 53 mm, slightly longer than their focal lengths. It is more accurate to say that this is the optimal configuration, since lasing will occur for a small range of mirror to crystal distances, the exact optimal distance depending on the focusing parameters of the pump, length of the crystal, etc. The method for calculating this distance, as well as all other distances of the geometry, is discussed below. The mirrors are also at angles to the length of the crystal and the propagation of the laser beam. This is to compensate for the astigmatism the Ti:saph laser field suffers when traveling through the crystal, and it can be shown that [104] the proper angle θ is given by

$$\frac{L_x}{R_m}\frac{\sqrt{n_C^4-1}}{n_C^4} = \frac{\sin^2(\theta)}{\cos(\theta)}, \tag{A.1}$$

where n_c is the refractive index of the crystal at the lasing wavelength and R_m is the radius of curvature of the mirrors. For the parameters used in the present experiments, this angle is about 10.9 degrees, although in practice the angle is tuned for optimal lasing.

The Ti:saph fluorescence is collimated by the inner-cavity mirrors in two arms. In reference to Figure A.1., the field bounces off a dielectric mirror, only used so that

the whole apparatus is compact, and travels through a two-plate birefringent filter (BF), which is at Brewster's angle with respect to the propagating field, and two uncoated etalons of thickness 0.1 mm and 1.5 mm. The BF is used to coarsely tune the central wavelength of the laser field, which is accomplished by rotating the BF so that the angle of the field propagation with the plates' optical axes changes [105]. The etalons are used for both fine tuning of the central wavelength, by changing the angle of incidence of the propagating field with respect to the etalon, and for pulse width control [57]. Finally, the field is incident on the output coupler, in which most of the field is reflected but a small amount is transmitted (in this instance around 5 percent). In the upper arm, the field is incident upon a reflecting mirror and sent to a focusing mirror (LGVD-700-825-1025-0.4CC, CVI) that then focuses down the beam onto a semiconductor saturable absorber mirror (SESAM) end mirror placed about 200 mm away. The SESAM is a remarkable device consisting of essentially a saturable absorber material often made from a quantum well grown upon a Bragg mirror [95] and allows the cavity to be passively modelocked. The properties of the quantum well in conjunction with the properties of the other cavity components such as the crystal and etalons determine the temporal and spectral width of the created pulse. The SESAMs used for the home-built laser were the same that were used by the commercial laser and had a temporal FWHM pulsewidth of about 100 ps, with the exact value depending on the wavelength.

The SESAM requires a small range of incident intensity to function properly. A beam that is too intense will destroy absorber material, while a beam that isn't intense enough either will suffer too much loss from the saturable absorber or operate in Q-switching mode and produce irregular pulses. Therefore, it is desirable to know the inner cavity beam characteristics produced by the cavity geometry before commencing

lasing. To discover the beam characteristics, we first note that in order for the cavity to produce a "stable" field, one that allows for a steady-state solution, the field must replicate its phase and spatial dependence upon consecutive round trips through the cavity. This means that for any particular point z in the cavity the beam characteristics must be identical at z and $z + 2L_c$, where a propagation distance of $2L_c$ implies one round trip through the cavity. Second, the inner cavity field of most Ti:saph lasers can be accurately approximated as a Gaussian beam. This means we can treat each cavity operation, whether a cavity element such as a mirror or a distance over which to propagate, as an ABCD matrix acting on the beam's complex q parameter [106]. At a particular point z, if the entire cavity matrix after one round trip is given by the matrix with components A, B, C, and D, then our first condition on the field implies that

$$q(z) = \frac{Aq(z) + B}{Cq(z) + D} \tag{A.2}$$

leading to the equation for q of

$$\frac{1}{q(z)} = -\frac{A - D}{2B} - i\frac{(1 - [(A + D)/2]^2)^{1/2}}{B}. \tag{A.3}$$

The real and imaginary parts correspond to the radius of curvature and beam waist via $R(z) = -\frac{2B}{A-D}$ and $w(z) = \frac{\lambda B}{\pi\left((1-[(A+D)/2]^2)^{1/2}\right)}$. Note that this must be true for all points inside the cavity, including at the SESAM end mirror and output coupler. Using this technique and knowledge of the components inside the cavity, an accurate approximation for the intensity incident on the SESAM can be found. But what should the intensity be? That was estimated by modeling the commercial pump laser's cavity geometry and considering the input pump power to that laser. The geometry of the home-built cavity was designed so that the SESAM would experience that level

of intensity, with the most important element in the design being the curvature of the focusing mirror that focuses the inner cavity beam onto the SESAM. The cavity was also designed so that the inner-cavity field was nearly collimated on the output coupler, although in practice it is simpler to achieve lasing when the field is focused on the output coupler and then tune the parameters of the cavity, namely distances, so that the field is collimated on the output coupler.

The laser used to pump the home-built Ti:saph laser was a Verdi-V5 (Coherent) that output approximately 5 watts of CW laser light operating at 532 nm. The average power output of the home-built laser was around 500 mW, but was wavelength dependent in accordance with the particular SESAM used. The pulse FWHM duration was around 100 ps but was also somewhat wavelength dependent depending on the particular SESAM used. The full central wavelength range of the laser was from approximately 730 nm to 860 nm through the use of five different SESAMs.

As an aside, for future experiments, such as the two-color Hong-Ou-Mandel interference experiment, it will be desirable to have at least one more Ti:saph laser. This laser might not have to be as powerful as the two pump lasers used in the quantum frequency translation experiment. In theory this means the laser field pumping the new Ti:saph laser will not have to be as powerful, which is fortunate since these types of pumping lasers are very expensive. In looking forwards toward future experiments, a low-pump threshold laser was built that could operate on less than one watt of pump power. The key difference between this laser and the "regular" pump lasers is that the inner-cavity mirrors used (LGVD-700-825-1025-0.05CC, CVI) had a radius of curvature of half the value as those of the regular pump lasers. This lowered the threshold of the laser because it created a tighter focus in the crystal so that the intensity inside the crystal was nearly the same as that in the regular pump

lasers [107]. The low-threshold laser had a pump threshold of about 0.57 W and a slope efficiency of about 9.2 percent.

REFERENCES CITED

[1] J. P. Dowling and G. J. Milburn, Phil. Trans. R. Soc. Lond. A **361**, 1655 (2003).

[2] D. Bouwmeester, A. Ekert, and A. Zeilinger, *The Physics of Quantum Information* (Springer, Berlin, 2000).

[3] M. O. Scully and M. S. Zubairy, *Quantum Optics* (Cambridge University Press, Cambridge, UK, 1997).

[4] E. Joos, D. H. Zeh, C. Kiefer, G. D. J. W., J. Kupsch, and I. O. Stamatescu, *Decoherence and the Appearance of a Classical World in Quantum Theory* (Springer, Berlin, 2010).

[5] A. Badolato, K. Hennessy, M. Atature, J. Dreiser, E. Hu, P. M. Petroff, and A. Imamoglu, Science **308**, 1158 (2005).

[6] S. Beveratos, A. Kuhn, R. Brouri, T. Gacoin, J. P. Poizat, and P. Grangier, Euro. Phys. J. D **18**, 191 (2002).

[7] C. Brunel, B. Lounis, P. Tamarat, and M. Orrit, Phys. Rev. Lett. **83**, 2722 (1999).

[8] S. E. Harris, M. K. Oshman, and R. L. Byer, Phys. Rev. Lett. **18**, 732 (1967).

[9] W. H. Louisell, A. Yariv, and A. E. Siegman, Phys. Rev. **124**, 1646 (1961).

[10] D. C. Burnham and D. L. Weinberg, Phys. Rev. Lett. **25**, 84 (1970).

[11] R. Short and L. Mandel, Phys. Rev. Lett. **51**, 201 (1983).

[12] W. P. Grice, A. B. U'Ren, and I. A. Walmsley, Phys. Rev. A **64**, 063815 (2001).

[13] M. Fiorentino, L. Voss, J. E. Sharping, and P. Kumar, Photo. Tech. Lett. **14**, 983 (2002).

[14] B. J. Smith, P. Mahou, O. Cohen, J. S. Lundeen, and I. A. Walmsley, Opt. Express **17**, 23589 (2009).

[15] K. Garay-Palmett, H. J. McGuinness, O. Cohen, J. S. Lundeen, R. Rangel-Rojo, A. B. U'ren, M. G. Raymer, C. J. McKinstrie, S. Radic, and I. A. Walmsley, Opt. Express **15**, 14870 (2007).

[16] O. Cohen, J. S. Lundeen, B. J. Smith, G. Puentes, P. J. Mosley, and I. A. Walmsley, Phys. Rev. Lett. **102**, 123603 (2009).

[17] G.-P. K., A. B. U'ren, R. Rangel-Rojo, R. Evans, and S. Camacho-Lopez, Phys. Rev. A **78**, 043827 (2008).

[18] P. Kok, W. J. Munro, K. Nemoto, T. C. Ralph, J. P. Dowling, and G. J. Milburn, Rev. Mod. Phys. **79**, 135 (2007).

[19] G. K. Wong, A. Y. H. Chen, S. W. Ha, R. J. Kruhlak, S. G. Murdoch, R. Leonhardt, J. D. Harvey, and N. Joly, Opt. Express **13**, 8662 (2005).

[20] J. I. Cirac, P. Zoller, H. J. Kimble, and H. Mabuchi, Phys. Rev. Lett. **78**, 3221 (1997).

[21] J. M. Huang and P. Kumar, Phys. Rev. Lett. **68**, 2153 (1992).

[22] S. Tanzilli, M. Halder, O. Alibart, N. Baldi, P. Gisin, and H. Zbinden, Nature **437**, 116 (2005).

[23] H. Takesue, Phys. Rev. A **82**, 013833 (2010).

[24] C. J. McKinstrie, J. D. Harvey, S. Radic, and M. G. Raymer, Opt. Express **13**, 9131 (2005).

[25] T. A. Birks, J. C. Knight, and P. S. J. Russel, Opt. Lett. **22**, 961 (1997).

[26] K. Inoue, IEEE Photon. Technol. Lett. **6**, 1451 (1994).

[27] K. Uesaka, K. K. Y. Wong, M. E. Marhic, and L. G. Kazovsky, IEEE J. Sel. Top. Quantum Electron. **8**, 560 (2002).

[28] A. H. Gnauck, R. M. Jopson, C. J. McKinstrie, J. C. Centanni, and S. Radic, Opt. Express **14**, 8989 (2006).

[29] D. Mechin, R. Provo, J. D. Harvey, and C. J. McKinstrie, Opt. Express **14**, 8995 (2006).

[30] R. H. Stolen, *Fundamentals of Raman amplification in fibers* (Springer, New York, 2003), vol. 1.

[31] Q. Lin, F. Yaman, and G. P. Agrawal, Phys. Rev. A **75**, 023803 (2007).

[32] R. H. Stolen, IEEE J. Quantum Electron. **QE-15**, 1157 (1979).

[33] M. G. Raymer, S. J. van Enk, C. J. McKinstrie, and H. J. McGuinness, Opt. Commun. **283**, 747 (2010).

[34] B. J. Smith and M. G. Raymer, New J. Phys. **9**, 414 (2007).

[35] I. Popescu, P. Sterian, and M. Dobre, Rom. Rep. Phys. **62**, 360 (2010).

[36] X. Y. Wu, X. J. Liu, Y. H. Wu, Q. C. Wang, Y. Wang, and L. X. Chi, Int. J. Theor. Phys. **49**, 194 (2010).

[37] P. A. Dirac, Proc. Roy. Soc. A **114**, 243 (1927).

[38] R. Loudon, *The Quantum Theory of Light: 3rd edition* (Oxford University, Oxford, 2000).

[39] M. Orszag, *Quantum Optics: 2nd Edition* (Springer, Berlin, 2008).

[40] D. F. Walls and G. J. Milburn, *Quantum Optics: 2nd Edition* (Spring, Berlin, 2008).

[41] L. Mandel and E. Wolf, *Optical Coherence and Quantum Optics* (Cambridge University, Cambridge, 1995).

[42] D. Steck, *Quantum and Atom Optics* (2010), URL `http://steck.us/teaching`.

[43] B. J. Smith, Ph.D. thesis, University of Oregon (2005).

[44] C. Leary, Ph.D. thesis, University of Oregon (2010).

[45] D. J. Griffiths, *Introduction to Quantum Mechanics* (Benjamin Cummings, San Francisco, 2004).

[46] J. Sakurai, *Modern Quantum Mechanics* (Addison Wesley, San Francisco, 1993).

[47] P. Grangier, G. Roger, and A. A., Europhys. Lett. **1**, 173 (1986).

[48] P. W. Milonni, *The Quantum Vacuum: An Introduction to Quantum Electrodynamics* (Academic Press, Maryland Heights, MO, 1993).

[49] E. C. G. Sudarshan, Phys. Rev. Lett. **10**, 277 (1963).

[50] T. Young, Phil. T. R. Soc. Lond. **94**, 1 (1804), URL `http://www.jstor.org/stable/107135`.

[51] A. A. Michelson, Am. J. Sci. **22**, 120 (1881).

[52] C. Roddier and F. Roddier, JOSA **66**, 580 (1976).

[53] R. Hanbury-Brown and R. Q. Twiss, Nature **177**, 27 (1956-1958).

[54] H. Bachor, *A Guide to Experiments in Quantum Optics* (Wiley-Vch, Weinheim, 1998).

[55] M. Beck, J. Opt. Soc. Am. B **24**, 2972 (2007).

[56] H. Yokota, H. Kanomori, Y. Ishiguro, G. Tanaka, S. Tanaka, H. Takada, M. Watanabe, S. Suzuki, K. Yano, M. Hoshikawa, et al., in *Tech. Digest of Opt. Fiber Commun.* (1986), p. PD3.

[57] B. Saleh and M. Teich, *Fundamentals of Photonics* (Wiley, New York, 1991).

[58] K. Okamoto, *Fundamentals of Optical Waveguides* (Academic Press, Amsterdam, 1990).

[59] L. B. Jeunhomme, *Single-Mode Fiber Optics: Principles and Applications* (Marcel Dekker, New York, 1990).

[60] G. P. Agrawal, *Nonlinear Fiber Optics: 4th edition* (Academic, San Diego, 2006).

[61] I. P. Kaminow, IEEE J. Quantum Electron. **17**, 15 (1981).

[62] A. Mendez and T. F. Morse, *Specialty optical fibers handbook* (Academic Press, Amsterdam, 2007).

[63] G. R. Fowles, *Introduction to Modern Optics* (Dover, New York, 1989).

[64] J. C. Knight, T. A. Birks, P. S. Russel, and D. M. Atkins, Opt. Lett. **21**, 1547 (1996).

[65] P. S. Russel, Science **299**, 358 (2003).

[66] T. A. Birks, J. C. Knight, B. J. Mangan, and P. S. J. Russell, IEICE Trans. Electron. **E84-C**, 585 (2001).

[67] A. Yariv, *Optical Electronics in Modern Communications* (Oxford University Press, Oxford, 1997).

[68] J. Gordon, H. Zeiger, and C. Townes, Phys. Rev. **95**, 282 (1954).

[69] T. H. Maiman, Nature **187**, 2493 (1960).

[70] L. E. Garwin and T. E. Lincoln, *A Century of Nature: Twenty-One Discoveries that Changed Science and the World* (University Of Chicago Press, Chicago, 2003).

[71] P. Franken, A. Hill, C. Peters, and G. Weinreich, Phys. Rev. Lett. **7**, 118 (1961).

[72] R. W. Boyd, *Nonlinear Optics* (Academic, New York, 2008).

[73] C. V. Raman, Nature **121**, 501 (1928).

[74] R. W. Eckhardt, F. Hellwarth, S. McClung, D. Schwarz, F. Weiner, and E. J. Woodbury, Phys. Rev. Lett. **9**, 455 (1962).

[75] C. J. McKinstrie, S. Radic, and A. R. Chraplyby, IEEE J. Sel. Top. Qu. Elect. **8**, 538 (2002).

[76] J. Chen, X. Li, and P. Kumar, Phys. Rev. A. **72**, 033801 (2005).

[77] W. P. Grice and I. A. Walmsley, Phys. Rev. A **56**, 1627 (1997).

[78] A. L. Berkhoer and V. E. Zakharov, JETP **31**, 486 (1970).

[79] R. H. Stolen, M. A. Bosch, and C. Lin, Opt. Lett. **6**, 213 (1981).

[80] R. J. Kruhlak, G. K. L. Wong, J. S. Y. Chen, S. G. Murdoch, R. Leonhardt, J. D. Harvey, N. Y. Joly, and J. C. Knight, Opt. Lett. **31**, 1379 (2006).

[81] C. McKinstrie, Opt. Express **12**, 2033 (2004).

[82] M. T. Rakher, L. J. Ma, O. Slattery, X. A. Tang, and K. Srinivasan, Nature Photonics **4**, 786 (2010).

[83] R. Jiang, R. Saperstein, A. N., M. Nezhad, C. McKinstrie, J. Ford, Y. Fainman, and S. Radic, Photo. Tech. Lett. **18**, 2445 (2006).

[84] H. J. McGuinness, M. G. Raymer, C. J. McKinstrie, and S. Radic, Phys. Rev. Lett. **105**, 093604 (2010).

[85] H. J. McGuinness, M. G. Raymer, C. J. McKinstrie, and S. Radic, Photo. Tech. Lett. **23**, 109 (2011).

[86] C. J. McKinstrie, S. Radic, and M. G. Raymer, Opt. Express **12**, 5037 (2004).

[87] C. McKinstrie, Opt. Commun. **282**, 583 (2009).

[88] M. Boas, *Mathematical Methods in the Physical Sciences* (John Wiley and Sons, New York, 1983).

[89] C. K. Hong, Z. Y. Ou, and L. Mandel, Phys. Rev. Lett. **59**, 2044 (1987).

[90] P. D. Drummond and C. W. Gardiner, J. Phys. A **13**, 2353 (1980).

[91] C. W. Gardiner, *Quantum Noise* (Springer, Berlin, 1992).

[92] J. A. Fleck, J. R. Morris, and M. D. Feit, Appl. Phys. **10**, 129 (1976).

[93] W. H. Press, S. A. Teukoslky, W. T. Vetterling, and B. P. Flannery, *Numerical Recipes in Fortran: Second Edition* (Cambridge Universit Press, Cambridge, 1992).

[94] J. C. Butcher, *Numerical methods for ordinary differential equations* (John Wiley and Sons., New York, 2003).

[95] K. Ursula, K. J. Weingarten, F. X. Kartner, D. Kopf, B. Braun, I. D. Jung, R. Fluck, C. Honninger, N. Matuschek, and J. Aus der Au, IEEE J. Sel. Top. Quant. **2**, 435 (1996).

[96] J. Fan and A. Migdall, Opt. Express **13**, 5777 (2005).

[97] D. Derickson, *Fiber-optic test and measurement* (Prentice Hall, 1997).

[98] C. Maxfield, *The design warrior's guide to FPGAs : devices, tools and flows* (Elsevier, Boston, 2004).

[99] H. Takesue and K. Inoue, Opt. Express **13**, 7832 (2005).

[100] K. L. Reichenbach and C. Xu, Opt. Express **13**, 2799 (2005).

[101] J. S. Y. Chen, S. G. Murdoch, R. Leonhardt, and H. J. D., Opt. Express **14**, 9491 (2006).

[102] E. Knill, R. Laflamme, and G. J. Milburn, Nature **409**, 46 (2001).

[103] D. T. Smithey, M. Beck, J. Cooper, and M. G. Raymer, Phys. Rev. A **48**, 3159 (1993).

[104] J. C. Diels and W. Rudolph, *Ultrashort Laser Pulse Phenomena* (Academic Press, Ampsterdam, 2006).

[105] S. Zhu, Appl. Opt. **29**, 410 (1990).

[106] W. T. Silfvast, *Laser Fundamentals: Second Edition* (Cambridge University Press, Cambridge, 2004).

[107] W. Ling, Y. Jia, J. Sun, Z. Wang, and Z. Wei, Appl. Opt. **45**, 2495 (2006).